Chapter 4

Results and Discussion

4.1 Determination of Hole Concentrations with Various Critical Temperatures

The effects of planar hole concentration, p, on the microwave properties of high-quality c-axis oriented epitaxial thin films for $YBa_2Cu_3O_{7-\delta}$ (YBCO) and $Y_{0.7}Ca_{0.3}Ba_2Cu_3O_{7-\delta}$ (Ca-YBCO) samples have been investigated. The hole concentration was varied by changing the oxygen deficiency for the YBCO and Ca-YBCO thin films. The critical temperature, T_c, was obtained from both resistivity and microwave resonance frequency measurements. The value of T_c was taken at zero resistance and accuracy within 1 K for these samples from the above two methods. In particular, the determination of p and T_c is shown as accurately as possible because of the extreme sensitivity of various ground-state superconducting and normal state properties to p. In fact, Tallon et al. [53, 134] have reported that near the optimum doping level the pseudogap energy scale, superfluid density and other physical quantities change quite abruptly and substantially for a small change in p. With reference to the measurements of the relationship between T_c and hole concentration p, it appears that the HTSC have exhibited a similar phase relation which can be expressed as a single universal curve $T_c(p)/T_{c,max}$ for all HTSC, where $T_{c,max}$ is maximum value of T_c for various HTSC. And so, later, in order to get the hole concentration p, we use the empirical relation

$$\frac{T_c}{T_{c,max}} = 1 - 82.6(p - 0.16)^2, \qquad (4.1)$$

here we take $T_{c,max}$ = 84 K for $Y_{0.7}Ca_{0.3}Ba_2Cu_3O_{7-\delta}$ film and $T_{c,max}$ = 91 K for $YBa_2Cu_3O_{7-\delta}$ film which has been reported previously [110, 111]. In our samples, however, the $T_c/T_{c,max}$ versus p phase diagram obeys the empirical relation very well, as shown in Fig. 4.1.

4.2 Resonance Frequency and Penetration Depth

Microwave microstrip resonators have attracted a lot of attention due to their ability to integrate into conventional microwave circuitry and one of the most sensitivity techniques for probing the surface properties of the superconducting sample. In particular, ring resonator with or without a gap have been performed by Gou et al. [35, 116] to depict the frequency dependence of the forward transmission coefficient S_{21} on the same microstrip ring resonator, including numerical simulations using "ANSOFT" program and inductance equivalent circuit model. Moreover, on the one hand, the measurements of the resonance frequencies f(T) of the resonator structure also serve as a viable tool for measuring the temperature dependence of the effective dielectric constant of the ring resonator, from which the dielectric constant of the substrate can be obtained. For example, the dielectric constant ε_r=25.7 for LAO substrate has been obtained by this method. On the other hand, the resonating mode of the ring resonator has a field distribution similar to the quasi-TEM mode of the strip line [135]. If we assume that the existence of E_z modes is a pure longitudinal electric field and the magnetic field is perpendicular to the z-axis, the solution to the Maxwell's equations gives the resonate condition as $2\pi r_o \cong n\lambda_p = n\, v_p/f$, where r_o is the outer radius of the ring, λ_p is the wavelength in the ring resonator and n is an arbitrary integer. From $2\pi r_o \cong v_p/f$ with n=1, we obtained the phase velocity almost consistent with the one estimated from the microstrip line resonator by the condition, $\lambda_p/2$ =L=

$v_p/2f$, where L is the microstrip line length.

Fig. 4.2 shows the temperature dependence of resonance frequency f(T) of the same ring resonator with the YBCO thin film (YBCO ring resonator) for p = 0.16, 0.148, 0.134, 0.098, 0.09 and 0.074, respectively. The resonance frequencies are measured around 3.62 GHz. For each hole concentration p, the resonance frequency decreases as increasing temperature T. The rapid shift in the resonance frequency near T_c indicates the effect of Cooper pair breaking. As the hole concentration of the YBCO ring resonator decreases, the resonance frequency f(T) decreases with decreasing p. The inset in Fig. 4.2 shows the normalized temperature dependence of the f(T)/f(5K), which indicates a unique manner and independence of the hole concentrations at $T < 0.6\ T_c$. Since the results were obtained from the same sample, the results have to be understood within the scenario in which their only difference of T_c stems from the oxygen content of the YBCO films only. In other words, the origin of the superconducting me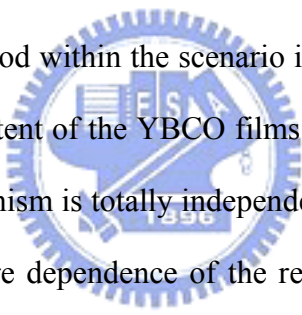chanism is totally independent of the oxygen concentration. Fig. 4.3 shows the temperature dependence of the resonance frequency, f(T), of the same ring resonator with the Ca-YBCO thin film (Ca-YBCO ring resonator) for various hole concentrations. The results are also measured at f = 3.62 GHz. In the overdoped regime (p>0.16), it shows that the resonance frequency for p = 0.218 at any temperature is smaller than the one for p = 0.188 and p =0.207. This result indicates that the resonance frequency f(T) increases with decreasing p. However, in the underdoped regime (p<0.16), the resonance frequency f(T) decreases with decreasing p. In Fig. 4.3, the inset shows that the normalized temperature dependence of resonance frequency f(T)/f(5K) of the Ca-YBCO ring resonator, and it shows the same behavior at $T<0.6T_c$. Figs. 4.4 and 4.5 show the temperature dependence of resonance frequency f(T) measured around 5.2 GHz for the microstrip line resonators with the YBCO thin film (YBCO microstrip line resonator), and the Ca-YBCO thin

film (Ca-YBCO microstrip line resonator), respectively. The temperature and doping dependences of the resonance frequency show the same results with the one which was measured by ring resonators for the YBCO and Ca-YBCO thin films. The rapid decrease in frequency as T approaches to T_c from the lower temperature is because of the rapid increase in $\lambda(T)$ and the effect of Cooper pair breaking. Fig. 4.6 shows the normalized temperature dependence of the change of resonance frequency $-\Delta f(T)/f(5K)=1-f(T)/f(5K)$ for the YBCO ring resonator with various hole concentrations p. As $T/T_c <0.1$, the change of resonance frequency $-\Delta f(T)/f(5K)$ is very small and almost equals to zero. In fact, this indicates a flattening of the resonance frequency f(T) at $T/T_c <0.1$ and later, we will make sure whether this phenomenon was an effect of quasiparticle localization or not. The same results were observed by Ca-YBCO ring resonator, YBCO microstrip line resonator and Ca-YBCO microstrip line resonator with various hole concentrations p, as shown in Figs. 4.7, 4.8 and 4.9, respectively.
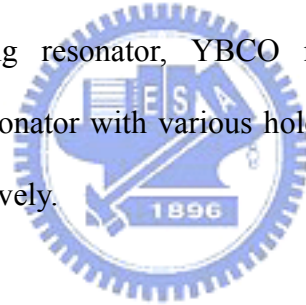
For the microstrip ring and line resonators with double-sided YBCO and Ca-YBCO thin films, the resonance frequency is directly related to the inductance L and capacitance C, by the expression $f \propto 1/\sqrt{LC}$. Since the change of the capacitance C(T) with temperature is much smaller than the inductance L(T), therefore, we can take the L(T) as the only changing variable of f(T). By incorporating the resonance frequency with the magnetic penetration depth $\lambda(T)$ of the thin films at different temperatures, T and T_0, an inductive formula for a superconductor strip transmission line was derived by Chang [125-127],

$$\frac{f(T)}{f(T_0)} = \sqrt{\frac{1 + \frac{\lambda(T_0)}{d}[2\coth(t/\lambda(T_0)) + g\,csch(t/\lambda(T_0))]}{1 + \frac{\lambda(T)}{d}[2\coth(t/\lambda(T)) + g\,csch(t/\lambda(T))]}}.$$ (4.2)

Here T_0 is the lowest temperature in the experiments (taken as 5 K here), d (~0.125mm) is the effective thickness of the dielectric, t (~500nm) is the thickness of the YBCO or Ca-YBCO film, and g is the conductor asymmetry factor, respectively. To obtain the absolute values of $\lambda(T)$, the modified two-fluid model has to be assumed. Following a number of previous studies, for example THz experiments [136], we will take a functional form:

$$\lambda(T) = \lambda(5K)[1 - (\frac{T}{T_c})^2]^{-\frac{1}{2}} ,$$ (4.3)

at $0.3 \leq T/T_c \leq 0.6$. Using (4.2) and (4.3), then the best fit to the experimental curves $f(T)$ gets the $\lambda(5K)$. For example, the best least-square fit yields $\lambda(5K) = 145.7$ nm and $\lambda(5K) = 195.7$ nm for the YBCO ring resonator with $p = 0.16$ and $p = 0.09$, as shown in Figs. 4.10(a) and 4.10(b), respectively. Figs. 4.11(a) and 4.11(b) show the fitting results of the Ca-YBCO ring resonator, where $\lambda(5K) = 212$ nm and $\lambda(5K) = 202.7$ nm with $p = 0.218$ and $p = 0.111$, respectively. The YBCO and Ca-YBCO ring resonators are noted as samples' names: YC010105A and Ca-Y040305A. The obtained values of penetration depth $\lambda(5K)$ for YBCO and Ca-YBCO films with various hole concentrations are listed in Table 4.1. Then, the obtained value of $\lambda(5K)$ was then inserted into Eq. (4.2) to obtain $\lambda(T)$ for all temperatures. It is noted that, for $p = 0.16$ and $p = 0.218$ (i.e. the optimally doped YBCO and Ca-YBCO films), the values of $\lambda(5K) = 145.7$ nm and $\lambda(5K) = 212$ nm are very close to that reported for the YBCO and Ca-YBCO single crystals [55, 137]. On the other hand, we also fit the experimental data measured by the YBCO and Ca-YBCO microstrip line resonators.

And the fitting results are shown in Fig. 4.12(a) (Sample:YC020309A) and 4.12 (b) (Sample:Ca-Y050406A), where $\lambda(5K) = 195.4$ nm for $p = 0.148$ and $\lambda(5K) = 211.7$ nm for $p = 0.217$, respectively.

Table 4.1. The penetration depth $\lambda(5K)$ and the energy gap $2\Delta_0/k_B T_c$ for the YBCO and Ca-YBCO films are obtained from microstrip ring resonator measurements.

	T_c (K)	Hole concentrations p	λ(5K) nm	d($\Delta\lambda$)/dT (Å/K)	$2\Delta_0/k_B Tc$
	91	0.160	145.7±0.8	4.5±0.1	4.8±0.1
	90	0.148	150.7±0.3	3.3±0.1	6.8±0.2
YC010105A YBCO	86	0.134	162.2±0.2	4.1±0.1	6.2±0.2
	63	0.098	171.6±0.4	6.6±0.1	5.7±0.1
	54.5	0.090	195.7±0.2	8.2±0.2	6.0±0.1
	36.4	0.074	272.0±0.3	19.4±0.5	5.3±0.1
	60	0.218	212.0±2.3	7.6±0.3	6.4±0.3
	68.5	0.207	155.3±0.4	5.5±0.2	5.6±0.2
Ca-Y040305A Ca-YBCO	78.5	0.188	151.3±0.2	5.0±0.2	5.2±0.2
	73.5	0.121	188.4±0.2	5.7±0.2	6.1±0.2
	68	0.111	202.7±0.2	6.8±0.3	6.0±0.3
	48.5	0.088	270.4±1.4	13.7±0.5	5.6±0.2

It should be noted that there are four YBCO samples as sample's names: YC020309A, YC050109A, YC050514A and YC050705A, and two Ca-YBCO samples as sample's names: Ca-Y050406A and Ca-Y050527A. For the YBCO microstrip line resonator, the obtained value of $\lambda(5K)$ (see in Table 4.2) near optimum doping are very close to that reported for the YBCO thin films by use of two-coil mutual inductance method [138]. Fig. 4.13 shows the doping dependence of $\lambda(5K)$ for the YBCO and Ca-YBCO

thin films in comparison with the published thin film and single crystal data. $\lambda(5K)$ was decreased as p decrease in the overdoped regime ($p>0.16$) and increased as p decrease in the underdoped regime ($p<0.16$). Indeed, the doping dependence of measured $\lambda(5K)$ approaches to that for single crystal data, and it proved that the above method to find the penetration depth $\lambda(5K)$ is reasonable and reliable in the microstrip ring and line resonators deeply.

Table 4.2. The penetration depth $\lambda(5K)$ and the energy gap $2\Delta_0/k_BT_c$ for the YBCO and Ca-YBCO thin films are obtained from microstrip line resonator measurements.

	T_c (K)	Hole concentrations p	$\lambda(5K)$ nm	$d(\Delta\lambda)/dT$ (Å/K)	$2\Delta_0/k_BTc$
YC020309A YBCO	90	0.148	195.4±0.8	5.1±0.2	5.8±0.2
	69.5	0.106	242.0±0.7	11.2±0.4	4.3±0.1
	54.5	0.090	234.1±0.8	11.6±0.5	5.1±0.2
YC050109A YBCO	90	0.148	202.5±0.4	6.6±0.2	4.6±0.1
	49	0.085	255.7±2.2	13.4±1.1	5.3±0.4
	22	0.064	348.3±5.5	61.0	3.6±0.1
YC050514A YBCO	90	0.148	194.3±0.8	6.1±0.1	4.8±0.1
	80.5	0.122	219.6±2.9	8.4±0.7	4.4±0.3
YC050705A YBCO	90	0.148	193.1±1.4	5.0±0.3	5.9±0.3
	43	0.080	217.9±1.4	14.4±0.7	4.8±0.2
Ca-Y050406A Ca-YBCO	61	0.217	211.7±6.2	7.1±0.2	6.7±0.3
	74.5	0.197	166.4±1.1	4.8±0.4	6.4±0.5
	62	0.103	224.9±1.0	9.9±0.2	5.5±0.1
	52.5	0.092	227.9±0.9	11.9±0.4	5.0±0.2
	42.5	0.082	240.0±1.8	16.1±0.7	4.8±0.2
	37.5	0.078	256.0±2.6	19.6±0.8	4.8±0.2
Ca-Y050527A Ca-YBCO	74.5	0.197	161.5±2.0	6.3±0.1	4.7±0.1
	53	0.093	250.6±5.5	11.2±0.5	5.8±0.3

The change in the penetration depth $\Delta\lambda(T)$, defined as $\Delta\lambda(T) \equiv \lambda(T) - \lambda(T_0)$, and $T_0 = 5$ K for simplicity, has been depicted in Figs. 4.14(a) and 4.14(b), which show $\Delta\lambda(T)$ as a function of reduced temperature for the same YBCO and Ca-YBCO ring resonators with various hole concentrations. Figs. 4.15(a) and 4.15(b) show the normalized temperature dependence of $\Delta\lambda(T)$ at $0 \leq T \leq 0.4T_c$ for the YBCO ring resonator with p=0.148 and 0.098, respectively. Figs. 4.16(a) and 4.16(b) show the normalized temperature dependence of $\Delta\lambda(T)$ at $0 \leq T \leq 0.4T_c$ for the Ca-YBCO ring resonator with p=0.218 and 0.088, respectively. It is noted that $\Delta\lambda(T)$ is linear in the low temperature regime (0.1Tc < T < 0.3Tc), and indeed, $\Delta\lambda(T)$ is further flattening at $T<0.1T_c$ for both YBCO and Ca-YBCO thin films. Within the scenario of d-wave pairing, the linear-T dependence of $\Delta\lambda(T)$ would imply that the nodal line feature of the order parameter could persist to temperatures near $0.3T_c$. Following the model of d-wave superconductor with the line nodes in the order parameter, the linear $\Delta\lambda(T)$ is understood from the following expression:

$$\Delta\lambda(T) \cong [\frac{\lambda_0 \ln 2}{\Delta_0}]T, \tag{4.4}$$

where Δ_0 is the d-wave gap value at zero temperature [139] and λ_0 is taken as $\lambda(5K)$. Thus the slope of $\Delta\lambda(T)$ with respect to temperature would give a gap value. Tables 4.1 and 4.2 list the values of the slope of the $\Delta\lambda(T)$ measured by microstrip ring and line resonators for the YBCO and Ca-YBCO thin films with various hole concentrations. Then the values of the d-wave energy gap, $2\Delta_0 / k_B T_c$, were obtained. For example, in Table 4.1, when p=0.16, the $\Delta\lambda(T)$ has a slope of 4.5 Å/K, which is very close to that found in pure YBCO single crystal (a slope of 4.3 Å/K) [55]. And the energy gap $2\Delta_0 / k_B T_c$ =4.8 can be extracted within the framework of d-wave

pairing. In Tables 4.1 and 4.2, one can also find that the increase in the slope of $\Delta\lambda(T)$ with decreasing hole concentration in the underdoped regime. The reason may result from an increase in $\lambda(5K)$ and/or a decrease in $\Delta(0)$. Fig. 4.17 shows the doping dependence of the d-wave energy gap, $2\Delta_0/k_BT_c$ obtained from the BCS d-wave model for the YBCO and Ca-YBCO films. The average value (solid line) and the error bar of the all experimental data of the $2\Delta_0/k_BT_c$ are 5.4 and 0.7, respectively. In addition, the values of $2\Delta_0/k_BT_c$ extracted from the measurement of the penetration depth $\lambda(T)$ reported by Bonn et al.'s group (full triangles) [55, 67] and Panapogoulos et al.'s group (full diamonds) [140] were also plotted in Fig. 4.17 and consistent with our experimental data. So, if we stay with the d-wave interpretation, then from Fig. 4.17 one would reach the following conclusions. The characteristic of the d-wave pairing does not change significantly with moderate changes in the hole concentration with reducing oxygen content from the over- to the underdoped regime. Since the oxygen controlling process is completely reversible, indicating no microstructural changes other than oxygen content was occurring during the process [30], it seems that a pure d-wave pairing scheme may be adequate to reconcile the evolving changes in $\Delta\lambda(T)$ (including the slope and the penetration depth changes) with the reducing oxygen content obtained in the same YBCO and Ca-YBCO thin films. Therefore, all physical properties obtained in this work are thoroughly dependent on the same structure of the superconducting thin films and the ratio of energy gap to the critical temperature, $2\Delta_0/k_BT_c$, is around 5.4±0.7, and independent of the doping concentrations. The detailed experimental data are listed in Tables 4.1 and 4.2.

4.2.1 Ferrel-Glover-Tinkham (FGT) Sum Rule

We have measured the temperature dependence of in-plane magnetic penetration depth $\lambda(T)$ of the YBCO and Ca-YBCO thin films using microstrip ring and line resonators [110, 111]. Then, the superfluid density $n_s(T)$, which is inversely proportional to the square of the magnetic penetration depth $\lambda(T)$, was obtained. Fig. 4.18 shows the doping dependence of the superfluid density, $1/\lambda^2$, at 5 K for the YBCO and Ca-YBCO thin films. Obviously, in the underdoped regime, the $1/\lambda^2(5K)$ increases as increasing p. However, in the overdoped regime, it decreases as increasing p. Fig. 4.19 shows the $T_c/T_{c,max}$ vs $1/\lambda^2(5K)$ for the YBCO and Ca-YBCO thin films. In the underdoped regime, the $T_c/T_{c,max}$ is roughly proportional to the superfluid density $1/\lambda^2(5K)$, which was revealed as the Uemura relation [141], as shown in Fig. 4.19 (dotted line: Uemura line). When near the optimum or in the overdoped regime, the plateau in $T_c/T_{c,max}$ versus $1/\lambda^2(5K)$ was observed for the YBCO and Ca-YBCO thin films. However, for fully oxygenated Ca-YBCO thin film (p=0.218), $1/\lambda^2(5K)$ comes to stay on the Uemura line.

In experiments, Homes et al. [142] have reported a universal relation with the nature of superconductivity using optical measurements, which is shown as superfluid density n_s at 0K proportional to the product of critical temperature (T_c) and the d.c. conductivity σ_{dc} at T_c. This relation has also shown to be connected with the well-known Uemura relation [141], and it works reasonably well in either the under- to the overdoped regime for the high-T_c cuprate superconductors or conventional superconductors. From our experimental data, we can test this relation again by using the high quality YBCO and Ca-YBCO thin films. The superfluid density $n_s(T) \propto 1/\lambda^2(5K)$ has been measured by using the same high quality factor (Q $>10^4$) microstrip ring resonators made of double-sided YBCO and Ca-YBCO thin films.

And the d.c. conductivity σ_{dc} at T_c can be measured by standard four probe technique. For example, the in-plane resistivity as a function of temperature $\rho_{ab}(T)$ for the YBCO and Ca-YBCO thin films with various hole concentrations has been studied previously in details in chapter 2. In order to define the d.c. conductivity σ_{dc} at T_c, we introduce some characteristic temperature from the measurements of d.c. resistivity $\rho_{ab}(T)$ for the YBCO and Ca-YBCO films. The resistivity decreases gradually down to an onset temperature T_{c0}, after which it begins to decrease sharply and reaches zero (ρ_{ab}=0). The linear temperature dependence of $\rho_{ab}(T)$ was observed near the optimum doping in the normal state. The departure from linearity in underdoped samples that occurs at the characteristic temperature, T^*, somewhat above the T_c and T_{c0}. So, we have three regions, starting from higher temperatures, a linear region ($T^*<T$) (I), a nonlinear region ($T_{c0}<T<T^*$) (II), and a transition region ($T_c<T<T_{c0}$) (III). The d.c. conductivity $\sigma_{dc} = \dfrac{1}{\rho_{ab}(T)}$ at $T=T_c$ is determined by the intersection from two straight lines; one straight line is drawn from T_c($\rho_{ab}=0$) to the midpoint of sharply drop in region III. Another one is drawn from linearly extrapolated in-plane resistivities $\rho_{ab}(T)$ at T_{c0}. By using this method, the values of σ_{dc} at T_c at various hole concentrations were obtained and also listed in Table 4.3. It should be noted that for Ca-YBCO thin film at p = 0.088, the value of σ_{dc} at T_c was estimated by the interpolation between two values of σ_{dc} at T_c at p = 0.111 and 0.082, respectively.

Table 4.3. Some parameters for YBCO and Ca-YBCO thin films are obtained from microwave measurements and the resistivity measurements.

	Hole concentrations p	λ(5K) nm	σ_{dc} $(\Omega^{-1}cm^{-1})$	Constant a	$2\hbar\omega_g\ (meV)$
YC010105A YBCO	0.160	145.7±0.8	9100±500	5.4±0.3	42.3±2.3
	0.148	150.7±0.3	8600±500	5.4±0.3	41.9±2.4
	0.134	162.2±0.2	7800±600	5.5±0.4	40.7±3.1
	0.098	171.6±0.4	7400±800	7.0±0.8	38.0±4.1
	0.090	195.7±0.2	6800±900	7.1±0.9	33.3±4.4
	0.074	272.0±0.3	4400±900	8.4±1.7	26.3±5.4
Ca-Y040305A Ca-YBCO	0.218	212.0±2.3	****	****	****
	0.207	155.3±0.4	16700±500	3.1±0.1	18.3±0.5
	0.188	151.3±0.2	10600±600	4.7±0.3	31.8±1.8
	0.121	188.4±0.2	7200±700	6.2±0.6	39.3±3.8
	0.111	202.7±0.2	6300±900	5.5±0.8	32.2±4.6
	0.088	270.4±1.4	4000±1000	7.8±2.0	32.6±8.1

Based on our experimental data, we test the relation $\lambda^{-2}(5K) \propto \sigma_{dc}T_c$ for the a-b plane (that is, parallel to the copper-oxygen planes) properties of double-layer cooper oxide materials by using microwave measurement to probe the superfluid density $1/\lambda^2(5K)$ [111] and the standard four probe technique to extract the values of σ_{dc} at T_c [117]. The results for the scaling relation are shown in Fig. 4.20. The scaling relation $\lambda^{-2}(5K) \propto \sigma_{dc}T_c$ was holds for the cuprate high-Tc thin films from the under- to the overdoped regime. The single crystal data reported by Homes et al. [142] are described by the dotted line, $\lambda^{-2}(5K) = 4700\sigma_{dc}T_c$ (where $\lambda^{-2}(5K)$ is in

cm^{-2}, σ_{dc} is in $\Omega^{-1}cm^{-1}$, and T_c is in K). For the YBCO thin film (full circles) near

optimum doping, it can be described by the solid line with a slope ~5700 (as a guide

to the eye). But for the YBCO thin film in the underdoped regime, it only can be

described by the dashed line with a slope ~7500 (as a guide to the eye). The results

contained in this plot are that within error all of these points set into the range with a

slope of 3700 ~ 5700 near optimally or overdoped regime, as same as Homes et al.'s

data, but in the underdoped regime, the slope becomes larger (~7500) than the error

range. The combined data span nearly three times of magnitude of $\lambda^{-2}(5K)$, from the

insulating behavior in the underdoped copper oxides to the metallic behavior in the

a-b planes of the overdoped copper oxides.

In fact, the scaling relation, $\lambda^{-2}(5K) \propto \sigma_{dc} T_c$ for the a-b planes have been

interpreted in a number of different ways [142, 143]. Here we will interpret the

scaling relation, $\lambda_L^{-2} \propto \sigma_{dc} T_c$ based on the Ferrell-Glover-Tinkham (FGT) sum rule

[144, 145]. Since its discovery in the conventional superconductors, FGT sum rule

has been applicable in the understanding of electrodynamic properties about various

kinds of superconductors. It is well known that the FGT sum rule is particularly useful

as equal to the oscillator-strength sum rule in quantum physics and is an expression of

the conservation of charge. Their argument starts from the well-known

Kramers-Kronig relation based on causality and linearity, which can be written as:

$$\sigma_1(\omega) = \frac{2}{\pi} \int_0^\infty \frac{\omega' \sigma_2(\omega') d\omega'}{\omega'^2 - \omega^2} + const, \tag{4.5}$$

$$\sigma_2(\omega) = -\frac{2\omega}{\pi} \int_0^\infty \frac{\sigma_1(\omega') d\omega'}{\omega'^2 - \omega^2}, \tag{4.6}$$

which either σ_1 or σ_2 to be calculated, provided the other is known for all

frequencies. If we take the Eq. (4.6) and let $\omega \to \infty$, one finds

$$\lim_{\omega \to \infty} \sigma_2(\omega) = \lim_{\omega \to \infty} -\frac{2\omega}{\pi} \int_0^\omega \frac{\sigma_1(\omega')d\omega'}{\omega'^2 - \omega^2} = \frac{2}{\pi\omega} \int_0^\infty \sigma(\omega')d\omega'. \qquad (4.7)$$

If we assume that at very high frequencies (such as X-ray frequencies), well above the gap frequencies, there should be no change in properties on the transition to superconductivity, it then follows that

$$\int_0^\infty \sigma_{1n}(\omega)d\omega = \int_0^\infty \sigma_{1s}(\omega)d\omega, \qquad (4.8)$$

where σ_{1n} and σ_{1s} are the normal and superconducting state conductivities. That is, the area under the σ_1 curve must be conserved. But from the inspection of the measured conductivity curves shown in Refs. [143] and [146], we see that σ_{1s} falls below σ_{1n}, and goes to zero for $\omega < \omega_g$, where ω_g is the cut-off energy scale. Since there is no enough compensating rise in σ_{1s} for $\omega < \omega_g$, therefore we are led to assume that the missing area A annihilated from the $\sigma_{1s}(\omega)$ curve must appear in the delta function at $\omega = 0$. That is, we have $A\delta(\omega)$ where $A = \int_{0^+}^\infty (\sigma_{1n} - \sigma_{1s})d\omega$.

This area can be approximately equal to the product of the cut-off energy scale ω_g and the d.c. conductivity σ_{dc} at T_c, i.e, $A = 2\sigma_{dc}\omega_g$. The physical constraint of the missing area $A = 2\sigma_{dc}\omega_g$ is that σ_{dc} is essentially constant out to ω_g. It should be noted that the BCS model requires that the spectral weight of the condensate be fully formed at energies comparable to the energy gap $(2\hbar\omega_g \approx 2\Delta_0 = ak_B T_c)$. If a is equal to 3.5, then the energy gap is the BCS weak coupling.

Now, if we apply Kramers-Kronig relation, to compute the contribution of $A\delta(\omega)$ to $\sigma_2(\omega)$ under the constraint of causality and linear response, we find

$$\sigma_2(\omega) = \frac{2A}{\pi\omega} = \frac{4}{\pi}\sigma_{dc}\frac{\omega_g}{\omega} \ . \tag{4.9}$$

This shows that

$$\frac{\sigma_2}{\sigma_{dc}} = \frac{4}{\pi}\frac{\omega_g}{\omega} = \frac{2ak_BT_c}{\pi\hbar\omega} , \tag{4.10}$$

which had been observed empirically by Glover and Tinkham before this sum rule argument was developed. Relating these expressions to the London theory, in which

$$\sigma_2 = \frac{1}{\mu_0\omega\lambda^2} , \tag{4.11}$$

then Eqs. (4.9) and (4.10) can be rewritten as

$$\frac{1}{\lambda^2} = \frac{2\mu_0 A}{\pi} , \tag{4.12}$$

and

$$\frac{\lambda^{-2}}{\sigma_{dc}T_c} = \frac{2a\mu_0 k_B}{\pi\hbar} . \tag{4.13}$$

Thus, we see that the penetration depth is related to the missing area by $\lambda^{-2} = 2\mu_0 A/\pi$ from Eq. (4.12), so that in principle the d.c. superconducting properties can be computed from the superfluid density λ^{-2} measurement. Roughly speaking, the gap implies the superconductivity, but more carefully, it is the missing area that is important [23]. From Eq. (4.13), the universal relation $\lambda^{-2}(5K) \propto \sigma_{dc}T_c$ is directly obtained. Therefore from the experimental data, the energy scale $\hbar\omega$ related to k_BT_c gives us the value of constant a, where $a = 5.4$ is near optimum doping but $a \geq 7.0$ is in the underdoped regime ($p<0.1$) (see in Table 4.3). Fig. 4.21 shows the doping dependence of the normalized energy gap $2\Delta_0/k_BT_c$ extracted from the FGT sum rule for the YBCO and Ca-YBCO thin films. The ratio $2\Delta_0/k_BT_c$ seems to be monotonic with the doping level p and increases with decreasing doping at $p<0.1$. The inset shows the doping dependence of the magnitude of energy gap Δ_0 for the YBCO and Ca-YBCO thin films. We emphasize that if the cut-off energy scale

$2\hbar\omega_g$ is a characteristic property of the gap $2\Delta_0$, then the energy scale required to recover the full strength of the condensate in the optimally doped YBCO thin film is $2\hbar\omega_g = 5.4k_B T_c = 2\Delta_0$, in good agreement with the twice of the maximum value of d-wave gap Δ_d measured by scanning tunneling spectroscopy (STS) studies at 4.2K [147, 148]. In fact, this value is quantitatively agreement with the one measured by Andreev reflection [149] or microwave technique [55, 67]. But as considered to the doping dependence of the $2\Delta_0 / k_B T_c$, it is consistency with the one obtained from STS measurements based on the d-wave gap model, as reported by Yeh *et al.* [147] (see in Fig. 4.21). This result gives an evidence indirectly that not only the superconducting energy gap from the under- to the overdoped regime in YBCO and Ca-YBCO thin films is d-wave pairing symmetry but also the conservation of charge in the CuO_2 plane is obeyed.

4.2.2 Fermi-Liquid Correction Factor

Figs. 4.22(a) and 4.22(b) show the normalized temperature dependence of $1/\lambda^2(T)$ for the YBCO and Ca-YBCO ring resonators at $T<0.35T_c$. In the low temperature regime ($T< 0.3T_c$), the linear temperature dependence of $1/\lambda^2(T)$ was observed. As mentioned previously, the flattening of $\lambda(T)$ will come into play in $1/\lambda^2(T)$ at $T<0.1 T_c$. So, we take the linear-T fit on $1/\lambda^2(T)$ at $0.1T_c \leq T \leq 0.3T_c$, as shown in Fig. 4.22(a) and 4.22(b) (solid lines). The fitting results of $1/\lambda^2(T)$ were listed in Table 4.4 for the YBCO and Ca-YBCO ring resonators with various hole concentrations. Moreover, the same temperature dependent features of $1/\lambda^2(T)$ for the YBCO and Ca-YBCO microstrip line resonators with various hole concentrations were also observed. And the fitting results with a linear-T fit on $1/\lambda^2(T)$ were listed in Table 4.5. The values

of the slope, $-d\lambda^{-2}(T)/dT$ will provide valuable data to test some theoretical models. In particular, Wen and Lee's model based on the Fermi-liquid-described superconductivity along the lines of phenomenology will be testified. Their point of view is that the well defined quasiparticles (low-lying excitations) can be described in terms of Fermi-liquid theory [82]. And as the temperature is raised from T = 0 K, the thermal excitation of quasiparticles along the nodal line of the d-wave gap grows linearly with increasing temperature. They argued that the normal fluid density n_n(T) at low temperature could be expresses as [82, 83]:

$$\frac{n_n(T)}{m} = \frac{2\ell n 2}{\pi} \frac{k_B}{\hbar^2} \frac{n}{d} \alpha^2 (\frac{v_F}{v_2})T, \tag{4.14}$$

where m is the mass of the carriers, d/n is the average separation between CuO_2 planes stacked along the c axis, v_F/v_2 is the ratio of quasiparticle velocities (v_F and v_2 are the quasiparticles velocities along normal and tangential to the Fermi surface at each node), and α^2 is the Fermi-liquid correction accounted for charge currents renormalization. Wen and Lee's model predicts that $\alpha \leq 1$ and independent of doping. A linear temperature dependence of n_n(T) is a global property of most cuprate superconductors. It can be extracted from the measurements of the penetration depth λ(T) via the relation n_s(T)/m = n_s(0)/m − n_n(T)/m = $1/\mu_0 e^2 \lambda^2$(T). Furthermore, Durst and Lee [81] calculate for the transport of heat by d-wave quasiparticles in two dimensions, and they give that the residual term of thermal conductivity, κ_0/T, can be repressed as

$$\frac{\kappa_0}{T} = \frac{k_B^2}{3\hbar}(\frac{n}{d})(\frac{v_F}{v_2} + \frac{v_2}{v_F}) \approx \frac{k_B^2}{3\hbar}(\frac{n}{d})(\frac{v_F}{v_2}). \tag{4.15}$$

So, the measurements of κ_0/T provide a simple and direct measurements of $\frac{v_F}{v_2}$ in the cuprates.

105

The slop of the superfluid density with respect to temperature T, $d\lambda^{-2}(T)/dT$, is related with the Fermi-liquid correction factor α^2 and the linear quasiparticle term κ_0/T in thermal conductivity as

$$\frac{d\lambda^{-2}(T)}{dT} = -2.93 \times 10^{13} \frac{\kappa_0}{T} \alpha^2 . \qquad (4.16)$$

For the optimally doped YBCO sample, the κ_0/T value of 0.14 mW/K^2-cm can be taken from the thermal conductivity measurements of YBCO single crystal [150]. Hence the Fermi-liquid correction α^2 can be calculated as:

$$\alpha^2 = -\frac{2.44 \times 10^{-12}}{\lambda^2(5K)} \frac{d[\lambda^2(5K)/\lambda^2(T)]}{dT}, \qquad (4.17)$$

For the underdoped or overdoped samples, more elaborate consideration about the doping dependence of the residual thermal conductivity κ_0/T or v_F/v_2 is necessary to elucidate the accurate value of α^2. The thermal conductivity (κ) measurements by Sutherland et al. [151] have reported the values of κ_0/T and v_F/v_2 with various doping levels. Assuming the tendency of κ_0/T and v_F/v_2 with respect to p of single crystal data reported by Sutherland et al. is qualitatively and quantitatively applicable to our thin film samples, the values of α^2 for various hole concentrations are now accessible, as listed in Tables 4.4 and 4.5 for the microstrip ring and line resonators, respectively. It is found that the Fermi-liquid correction factor α predicted by Wen and Lee's model can be obtained with $\alpha < 1$ and nearly independent of doping (see in Fig. 4.23), which is consistent with that predicted by Wen and Lee's model ($\alpha \leq 1.0$). In particular, $\alpha^2 \approx 0.4 \sim 0.5$ as $0.12 < p \leq 0.16$ is consistent with Sutherland et al.'s results. The experimental result reflects that the nature of the quasiparticles behaves as the Fermi liquid in the superconducting state for the YBCO and Ca-YBCO thin films.

Table 4.4. The Fermi-liquid correction factor α^2 for the YBCO and Ca-YBCO thin films are obtained from the microwave ring resonators.

	Hole concentrations p	$\lambda(5K)$ nm	$-\mathrm{d}(1/\lambda^2(T))/\mathrm{d}(T/T_c)$ (μm^{-2})	v_F/v_2	α^2
YC010105A YBCO	0.160	145.7±0.8	20±0.4	11.5	0.65
	0.148	150.7±0.3	14±0.4	11.1	0.47
	0.134	162.2±0.2	14.6±0.3	10.6	0.54
	0.098	171.6±0.4	14.6±0.3	9.4	0.83
	0.090	195.7±0.2	10.8±0.2	9.1	0.74
	0.074	272.0±0.3	6.4±0.1	8.5	0.70
Ca-Y040305A Ca-YBCO	0.218	212.0±2.3	7.7±0.3	23.1	0.18
	0.207	155.3±0.4	15.9±0.5	20.9	0.37
	0.188	151.3±0.2	20.4±0.6	17.1	0.51
	0.121	188.4±0.2	11.6±0.3	10.1	0.53
	0.111	202.7±0.2	9.7±0.3	9.8	0.49
	0.088	270.4±1.4	5.3±0.1	9.0	0.41

Table 4.5. The Fermi-liquid correction factor α^2 for the YBCO and Ca-YBCO thin films are obtained from the microstrip line resonators.

	Hole concentrations p	$\lambda(5K)$ nm	$-d(1/\lambda^2(T))/d(T/T_c)$ (μm^{-2})	v_F/v_2	α^2
YC020309A YBCO	0.148	195.4±0.8	11.6±0.5	11.1	0.39
	0.106	242.0±0.7	8.7±0.4	9.6	0.44
	0.090	234.1±0.8	8.4±0.4	9.1	0.57
YC050109A YBCO	0.148	202.5±0.4	12.6±0.4	11.1	0.43
	0.085	255.7±2.2	6.9±0.5	8.8	0.54
	0.064	348.3±5.5	*	*	*
YC050514A YBCO	0.148	194.3±0.8	13±0.4	11.1	0.44
	0.122	219.6±2.9	10.2±1.3	10.1	0.42
YC050705A YBCO	0.148	193.1±1.4	11.2±1.3	11.1	0.38
	0.080	217.9±1.4	9.3±0.5	8.7	0.84
Ca-Y050406A Ca-YBCO	0.217	211.7±6.2	6.3±0.4	22.9	0.15
	0.197	166.4±1.1	11.5±1.0	18.9	0.27
	0.103	224.9±1.0	8.8±0.7	9.5	0.51
	0.092	227.9±0.9	9.1±0.4	9.2	0.64
	0.082	240.0±1.8	8.4±0.4	8.7	0.77
	0.078	256.0±2.6	7.3±0.4	8.6	0.77
Ca-Y050527A Ca-YBCO	0.197	161.5±2.0	15.9±0.9	18.9	0.38
	0.093	250.6±5.5	5.4±0.3	9.2	0.37

4.3 Quality Factor and Surface Impedance

Because the loss tangent of the LaAlO$_3$ substrate is less than 5×10^{-6} at T < 77K, we can neglect the influence of the dielectric loss on the resonator. Another observation concerning with radiation loss is relatively difficult to evaluate, but the

loss is small because of the microwave microstrip resonator was placed on a sample housing with $\lambda_p / 2$ screening. In this study, we have illuminated that the resonators with very low microwave insertion loss and high quality factor (Q) are, indeed, attainable by using double-sided HTSC films. In fact the Q comes mainly from the surface resistance R_s of the superconducting films on the transmission plane and the ground plate. Figs. 4.24 and 4.25 show the temperature dependence of the quality factor, Q, of the YBCO and Ca-YBCO ring resonators with various hole concentrations. It is evident that Q(T) shows a linear temperature dependence in the low temperature regime and a precipitous drop at T near T_c. Furthermore, the quality factor reaches a value over 10^4 at the lower temperature near optimum doping, which is compatible with the best microstrip line resonators.

Fig. 4.26 shows the temperature dependence of the quality factor, Q, of the same YBCO microstrip line resonator measured at f = 5.2 GHz for p = 0.148, 0.106 and 0.09, respectively. From Fig. 4.26, it is evident that for p = 0.148, the quality factor reaches a value about 8×10^4 at the lower temperatures. As decreasing p, the low-temperature Q-value drops to a value about 2×10^4 at the lower temperatures. In particular, the abrupt increase of the Q-factor at p=0.16 was observed around T=30K. Another observation concerning this feature is shown in Fig. 4.27 for the Ca-YBCO microstrip line resonator at optimum doping (p=0.217). As is evident from Fig. 4.27, the temperature dependence of Q(T) for the fully oxygenated Ca-YBCO microstrip line resonator displays essentially the same behavior of the YBCO microstrip line resonator regardless of the existence of the calcium impurity atom. In fact, the Q-factor reaches the value over 10^4 at the lower temperature for both the YBCO and Ca-YBCO microstrip line resonators with various hole concentrations.

The surface impedance, in general, can be expressed as $Z_s = R_s + jX_s$. Here R_s is the surface resistance, which may be originated from the scattering between quasiparticles and various types of defects. And X_s is the reactance reflecting the nondissipative energy stored in the superconductor. R_s can be yielded from the relation $R_s = \Gamma/Q$, which has been obtained from Eq. (3.148) in chapter 3. On the other hand, the surface reactance can be calculated via the relation, $X_s(T) = \mu_0 \omega \lambda(T)$. Figs. 4.28(a) and 4.28(b) show the temperature dependences of $R_s(T)$ and $X_s(T)$ for a YBCO ring resonator with p = 0.16, 0.148, 0.134, 0.098, 0.09 and 0.074, respectively. The main qualitative feature of the surface resistance is the rapid drop at T_c, which is believed to result from the fluctuation effects [72]. Figs. 4.29(a) and 4.29(b) show the temperature dependences of $R_s(T)$ and $X_s(T)$ for a Ca-YBCO ring resonator with p = 0.218, 0.207, 0.188, 0.121, 0.111 and 0.088, respectively. The rapid drop of the $R_s(T)$ was also observed near T_c. For the YBCO and Ca-YBCO ring resonators in the low temperature regime, the value of the R_s is about 0.15 mΩ in the low temperature regime for all doping levels. And the value of the X_s is at least one order of magnitude larger than the value of the R_s for these samples. For the YBCO ring resonator, the temperature dependence of $R_s(T)$ shows an unusual monotonic temperature dependence below T_c. But for the Ca-YBCO ring resonator, the temperature dependence of $R_s(T)$ shows an monotonic temperature dependence below T_c. For the YBCO and Ca-YBCO microstrip line resonators, the temperature dependences of the $R_s(T)$ and the $X_s(T)$ show the monotonic temperature dependence below T_c for all doping levels, as shown in Figs. 4.30(a), 4.30(b), 4.31(a) and 4.31(b). In particular, the value of $R_s(T)$ reaches 0.02 mΩ for the YBCO microstrip line resonator at p=0.148 in the low temperature because of its very high quality factor (Q=8×10^4). Moreover, for these samples of microstrip ring and line

resonators, there does not display a broad peak, which was interpreted to arise from the competitions between the reduced quasiparticles density and the increasing in quasiparticle lifetime with descending temperature in the measurement of YBCO singe crystal [76, 152]. The common feature of the YBCO and Ca-YBCO thin films for all doping levels, except p=0.074, is the linearity of the surface resistance with temperature in the range of $T < T_c/2$, which has been considered as a characteristic of d-wave superconductivity in the pure d-wave order parameter [153]. This result is similar to the property of $R_s(T)$ observed in YBCO, BSCCO, and TBCCO single crystals which exhibits linear in the range of $T \leq T_c/2$ at frequencies below 20 GHz [55, 66, 154].

4.3.1 Real Part Conductivity

Figs. 4.32(a) and 4.32(b) show the temperature dependence of the microwave ab-plane real-part conductivity, σ_1, of the YBCO and Ca-YBCO ring resonators extracted from the $R_s(T)$ and $X_s(T)$ measurements for various hole concentrations. The real-part conductivity $\sigma_1(T)$ reaches a plateau in the low temperature limit (T<0.1Tc), which is clearly contradicted to that found by a high-purity single crystal in the clean limit [76]. The feature of σ_1 displays no peak from T_c down to the lowest measuring temperature, suggesting that the sample is not in the clean limit and the physical properties of the $\sigma_1(T)$ could not be explained by classical Drude model. For the YBCO ring resonator, the value of σ_1 decreases as decreasing p, as shown in Fig. 4.32(a). But for the Ca-YBCO ring resonator, the value of σ_1 increases as decreasing p in the overdoped regime, and the value of σ_1 decreases as decreasing p in the underdoped regime, as shown in Fig. 4.32(b).

In Fig. 4.33, we show the normalized conductivity $\sigma_1/\sigma_1(5K)$ vs T_c/T for the YBCO and Ca-YBCO ring resonators. A universal relation is emergent, indicating that the physical properties of the dissipation σ_1 have the same thermal properties in our ring resonator samples. It shows a unique property that $\sigma_1/\sigma_1(5K)\approx 1$ is independent of microscopic disorder and frequencies at $T/T_c<0.1$ ($T<10K$). Moreover, the onset of the rapid increase in σ_1 due to thermal fluctuations dominates the behavior in σ_1 at $0.5T_c<T<T_c$. Then, we take up the formula, $\sigma_1 = \sigma_1(5K)(1-Ae^{-c_1\cdot T_c/T})$, which gives a close form to achieve the percolation effect, to fit the experimental data by least square fitting of the "OriginR 7.0 SR0" program, where A and c_1 are two fitting parameters. Here $\sigma_1(5K)$ is the measured microwave conductivity at 5K. The fitting result is shown in Table 4.6. And in Fig. 4.34(a) (solid line), we show the fitting curve with the fitting parameters $A = 2.61\pm 0.03$ and $c_1 = 0.95\pm 0.01$ for the YBCO ring resonator with p=0.16. In Fig. 4.34(b) (solid line), the fitting curve with the fitting parameters $A = 2.01\pm 0.08$ and $c_1 = 0.87\pm 0.03$ for the YBCO ring resonator with p=0.098 is shown. Figs. 4.35(a) and 4.35(b) show the fitting curves for the Ca-YBCO ring resonator with p=0.218 and p=0.121, respectively. We can define $c_1\cdot T_c = E_{g1}(0)$ (or $c_1\cdot k_B T_c = E_{g1}(0)$ in meV unit : k_B is Boltzmann's constant), which is a thermal activation gap at 0K. And when $\sigma_1(T)$ is equal to zero, we found another characteristic temperature $T_{\sigma 1}^*$ from the criterion, $1=Ae^{-c_1\cdot T_c/T_{\sigma 1}^*}$. The doping dependences of $T_{\sigma 1}^*$, $E_{g1}(0)$ and T_c are shown in Fig. 4.36, and it is worthy mentioning that the p-dependent properties of $T_{\sigma 1}^*$ and T_c reveal roughly similar to the phase diagram reported by the model of the classical thermal fluctuations

suggested by Emery and Kivelson [88]. The most significance of the Emery and Kivelson's model is their prediction that phase fluctuations (thermal or quantum) are necessary to play a significantly larger role in high-Tc superconductors due to the existence of low superconducting carrier density and high T_c. Although to the present time, even a number of such experiments have been performed in order to confirm their prediction [91-94], the conclusive evidence has not given yet. We note that the implication of the formula $\sigma_1(5K)(1 - Ae^{-c_1 \cdot T_c /T})$ can be seen with another form, $\sigma_1(5K)(1 - e^{-E_{g1}(T)/k_B T})$, where the thermal activation gap or the coupling energy through the tunneling barrier $E_{g1}(T) = E_{g1}(0) - E_{g1}(0) \times \dfrac{T}{T_{\sigma 1}^*}$ is a function of temperature. We note that if the term $e^{-E_{g1}(T)/k_B T}$ is to be interpreted as a weight due to lose phase coherence memory, then $1 - e^{-E_{g1}(T)/k_B T}$ would play as a role of establishing phase coherence of the long-range order parameters. In fact, the result give a strong evidence that the thermal phase fluctuations plays an important role in high Tc superconductivity at $T \geq 0.5T_c$. From our experimental viewpoint, the thermal phase fluctuations can be enhanced not only originating from the low superfluid density but also from the surface inhomogeneity or weak disorder. However, it is very hard to give a clear evidence due to the inhomogeneity from microscopic origin. Since σ_1 comes from the contribution of quasiparticle flow, in our inhomogeneous (disordered) structures of thin films (grain size 150~400nm), the average grain is much larger than the mean free path ($\ell \approx 75nm$), which will be discussed later from Lee's model, and so the inhomogeneity caused by the disorder (grain boundary or non-superconducting region) can give the weak-link effect. In our opinion, the structures of the weak-link produce a network of tunneling junctions on these quasiparticles with different coupling strength.

Table 4.6. Some parameters for the YBCO and Ca-YBCO films are obtained from the numerical fitting of the real-part conductivity σ_1.

	Hole concentrations p	λ(5K) nm	c_1	A	$E_{g1}(0)$ (K)	$T_{\sigma1}^{*}$ (K)
YC010105A YBCO	0.160	145.7±0.8	0.95±0.01	2.61±0.03	86.4±0.9	90.1±1.4
	0.148	150.7±0.3	1.15±0.01	3.18±0.03	103.5±0.9	89.4±1.0
	0.134	162.2±0.2	0.93±0.01	2.46±0.04	79.9±0.8	88.8±1.8
	0.098	171.6±0.4	0.87±0.03	2.01±0.08	54.8±1.8	78.5±5.2
	0.090	195.7±0.2	1.00±0.01	2.50±0.04	54.5±0.5	59.4±1.1
	0.074	272.0±0.3	0.79±0.01	1.80±0.03	28.7±0.3	48.9±1.5
Ca-Y040305A Ca-YBCO	0.218	212.0±2.3	0.90±0.03	2.10±0.11	54.0±1.8	72.7±5.6
	0.207	155.3±0.4	1.06±0.02	2.85±0.06	72.6±1.3	69.3±1.9
	0.188	151.3±0.2	0.92±0.01	2.52±0.03	72.2±0.7	78.1±1.3
	0.121	188.4±0.2	0.99±0.01	2.32±0.03	72.7±0.7	86.4±1.5
	0.111	202.7±0.2	0.90±0.01	1.93±0.03	61.2±0.6	93.0±2.4
	0.088	270.4±1.4	1.29±0.05	2.56±0.17	62.5±2.4	66.5±5.3

In the light of Lee's model [80, 81], the microwave conductivity $\sigma_1(5K)$ must be composed of the universal conductance $\dfrac{e^2}{2\pi\hbar}$ due to the localization effects of the quasiparticles scattering with the impurities. According to Lee's model and Durst and Lee's model, we can write down $\sigma_1(5K) = \dfrac{e^2}{2\pi\hbar}\dfrac{v_F}{v_2}\alpha^2\beta/\zeta$, where v_F and v_2 are the velocities of the quasiparticles along normal and tangential to the Fermi surface at the nodes. And α^2, β and ζ are Fermi-liquid correction factor, vertex correction

factor and geometric length, respectively. As is well known, α^2 and β account for the charge current renormalization and the anisotropic impurity potential, respectively. ζ can be easily determined by the current flowing loop in the ring or line resonator. For example, ζ is equal to $\lambda t / 2\pi r \approx 3.2 \times 10^{-3}$ nm at p=0.16 for the YBCO ring resonator, where λ is the London penetration depth, t is the thickness of the film (500nm), r is the radius of the ring resonator (3.625mm). Based on the measurements of linear temperature dependence of $1/\lambda^2(T)$ and the ratio of v_F/v_2 (see Table. 4.4) [111], α^2 has been obtained with various hole concentrations p. Then, from the microwave measurements of the real-part conductivity $\sigma_1(5K)$, the doping dependence of the vertex correction factor β was obtained, as shown in Fig. 4.37, and its value is around 1.0±0.5. This value is apparently consistent with the theoretical prediction by Durst and Lee [81]. Based on Lee's model, in particular, the scattering rate $1/\tau$ would approaches to a constant value in the low-temperature regime. But in experiment, the direct measurement of $1/\tau$ is very difficult and sometimes needs the help of some theoretical models, such as Drude model, to extract the scattering rate. For example, Hardy et al. [76] have reported that the scattering rate reaches 5.2×10^{10} (s^{-1}) for high-purity single crystal in the clean limit by use of Drude model. But for the samples of thin films, the scattering rate usually has the order of magnitude about $10^{11} \sim 10^{12}$ (s^{-1}) at low temperature. In fact, Luo et al. [12] have used femtosecond spectroscopy to measure the quasiparticle relaxation time near the Fermi surface. And the quasiparticle relaxation time in the ab plane is about 3×10^{-12} (s) which corresponds to the scattering rate of 3.3×10^{11} (s^{-1}) at low temperature. As the scattering rate is taken as 3.3×10^{11} (s^{-1}) at 5 K, we have $\omega\tau \cong 0.068$ at resonance frequency f=3.62 GHz. By using the Drude form for f($\omega\tau$) in Eq. (3.115), the normalized temperature dependence of quasiparticle scattering rate $1/\tau$ was extracted, as shown in Figs. 4.38(a) and 4.38(b) for the YBCO and Ca-YBCO ring resonators

with various hole concentrations. The scattering rate below T_c falls rapidly and then approaches to a constant value in the low temperature ($T<0.4T_c$), which was predicted by Lee'd model. It is well known that the scattering rate of the quasiparticles by scattering with impurities (disorder) does not depend on temperature in general [74, 80], as confirmed in Figs. 4.38(a) and 4.38(b).

We conclude with confidence that part of the low-lying excitation states should be localized. Of course, the localized state have observable consequences if $g = \sigma_1(5K)/2\pi\hbar$ is not too large (order of unity). In Lee's model Ⅱ, there is another concern while $\sigma_1(\omega \to 0)$ is independent of disorder, the amount of disorder controls the energy scale over which this estimates applies. Then the impurity band for a dilute strong scatters is $\gamma_0 \approx \Delta_0(\Delta_0\tau)^{-1/2}$, where τ is quasiparticle relaxation time. In our case, the universal constant can be approached by $\Delta W <T<\gamma_0(\approx 0.1T_c)$. We therefore reach the calculation that for short coherent length d-wave superconductors, the low energy excitations with $E < \gamma_0$ are strongly localized. Fig. 4.39 shows the doping dependence of the energy scale $\Delta(0)$, $T_{\sigma 1}^*$, T_c, $E_{g1}(0)$, γ_0, ΔW and $\hbar/\tau$ for the YBCO and Ca-YBCO ring resonators. ΔW is the typical energy level spacing between two localized states within a localization length of each other. The magnitude of the thermal activation gap, $E_{g1}(0)$, is about $\frac{1}{3}\Delta_0$, as shown in Fig. 4.39. From Fig. 4.39, the energy scale can be placed by $\hbar/\tau \approx \Delta W <\gamma_0 < E_{g1}(0) \approx T_c <T_{\sigma 1}^*<\Delta_0$. And the experimental consequences are as follows: For $\Delta W <T<\gamma_0$, we expect the d.c.- or microwave conductance to be $\sigma_1 \approx (\frac{e^2}{2\pi\hbar})\frac{\xi_0}{a}$ due to macroscopic quantum tunneling of the quasiparticles. For $T>\gamma_0$, the more importance of the thermal fluctuations will behave in σ_1. In fact,

these localized quasiparticles can be attributed to the tunneling effect of quasiparticles in the weak links of our thin films. And σ_1 can be realized as that of quasiparticles in thermal insulator phase in the superconducting state, as suggested by Vishveshwara and Fisher's model.

Furthermore, we also report the temperature dependence of the real-part conductivity, σ_1, of the YBCO microstrip line resonator with $p = 0.148$, 0.106 and 0.09, as shown in Fig. 4.40. In Fig, 4.40, the real part conductivity, $\sigma_1(T)$ contains an extra linear-T contribution at T<35K for $p= 0.148$, which has been observed for high-purity single crystals, as reported by Hardy et al. [76]. It is evident that the broad peak was observed at T≈35K. When considering the linear-T contribution in σ_1, we use the formula, $\sigma_1 = \sigma_1(5K)[(1-Ae^{-c_1 \cdot T_c/T}) + a'\dfrac{T}{T_c}]$ to fit the $\sigma_1(T)$ of YBCO microstrip line resonator for $p=0.148$ at T<60K. The fitting result of σ_1 with $c_1 = 2.16 \pm 0.08$, $A = 28.27 \pm 3.38$ and $a'=1.46 \pm 0.02$ is shown in Fig. 4.41 (solid line). As the hole concentration p becomes 0.106 or 0.09, the extra linear-T contribution in $\sigma_1(T)$ has disappeared in the low temperature, as shown in Fig. 4.40. Apparently, $\sigma_1(T)$ reaches a plateau versus temperature in the low temperature limit for $p = 0.106$ and 0.09. Figs. 4.42(a) and 4.42(b) (solid lines) show the fitting result of σ_1 with the formula, $\sigma_1 = \sigma_1(5K)(1-Ae^{-c_1 \cdot T_c/T})$ for the YBCO microstrip line resonator with $p = 0.106$ and $p = 0.09$, respectively. The detailed fitting parameters are listed in Table 4.7.

Table 4.7. Some parameters for the YBCO and Ca-YBCO microstrip line resonators are obtained from the numerical fitting of the real-part conductivity σ_1.

	p	$\lambda(5K)$ nm	c_1	A	a'	$E_{g1}(0)$ (K)
YC020309A YBCO	0.148	195.4±0.8	2.16±0.08	28.27±3.38	1.46±0.02	194.4±7.2
	0.106	242.0±0.7	1.22±0.02	2.98±0.08	*	84.7±1.4
	0.090	234.1±0.8	1.41±0.02	3.35±0.1	*	76.8±1.1
YC050109A YBCO	0.148	202.5±0.4	1.84±0.04	9.14±0.55	0.35±0.01	165.6±3.6
	0.085	255.7±2.2	1.10±0.03	7.90±0.20	1.50±0.07	53.9±1.4
	0.064	348.3±5.5	0.78±0.15	0.80±0.17	*	17.1±3.3
YC050514A YBCO	0.148	194.3±0.8	1.12±0.01	3.08±0.06	*	100.8±0.9
	0.122	219.6±2.9	0.86±0.01	2.27±0.03	*	69.2±0.8
YC050705A YBCO	0.148	193.1±1.4	1.30±0.01	3.69±0.08	*	117±0.9
	0.080	217.9±1.4	0.74±0.01	1.23±0.03	*	31.8±0.4
Ca-Y050406A Ca-YBCO	0.217	211.7±6.2	1.91±0.05	12.01±0.67	0.96±0.02	116.5±3.0
	0.197	166.4±1.1	1.20±0.01	5.50±0.04	0.79±0.01	89.4±0.7
	0.103	224.9±1.0	1.18±0.02	10.06±0.24	2.65±0.07	73.1±1.2
	0.092	227.9±0.9	1.07±0.02	1.39±0.05	*	56.1±1.1
	0.082	240.0±1.8	1.32±0.04	1.66±0.11	*	56.1±1.7
	0.078	256.0±2.6	0.94±0.02	1.99±0.06	*	35.2±0.7
Ca-Y050527A Ca-YBCO	0.197	161.5±2.0	2.45±0.07	12.78±0.83	0.33±0.01	182.5±5.2
	0.093	250.6±5.5	0.81±0.01	1.55±0.02	*	42.9±0.5

For the Ca-YBCO microstrip line resonator, the temperature dependence of the real-part conductivity, σ_1, is shown in Fig. 4.43 at p = 0.217, 0.197, 0.103, 0.092, 0.082 and 0.078, respectively. It is apparently that the linear-T contribution in σ_1 was observed in the low temperature regime for p = 0.217, 0.197, 0.103. In Figs. 4.44(a), 4.44(b) and 4.44(c) (solid lines) show the fitting results of σ_1 with the formula, $\sigma_1 = \sigma_1(5K)[(1 - Ae^{-c_1 \cdot T_c / T}) + a' \dfrac{T}{T_c}]$. However, $\sigma_1(T)$ reaches a plateau versus temperature in the low temperature limit for p = 0.092, 0.082 and 0.078, as shown in Fig. 4.43. Figs. 4.44(d), 4.44(e) and 4.44(f) (solid lines) show the fitting result of σ_1 with the formula, $\sigma_1 = \sigma_1(5K)(1 - Ae^{-c_1 \cdot T_c / T})$ for p = 0.092, 0.082 and 0.078, respectively. The detailed fitting parameters are also listed in Table 4.7. By analyzing the microwave conductivity σ_1 of the YBCO and Ca-YBCO microstrip ring and line resonators with various hole concentrations, the doping dependence of the thermal activation gap, $E_{g1}(0)$ was revealed as in Fig. 4.45. Roughly speaking, the doping dependence of the $E_{g1}(0)$ is very similar to the "superconducting dome" of the T_c versus p in the doping-temperature phase diagram of the cuprates. On the other hand, comparing with the pure single crystal data in the clean limit reported by Hardy et al. [76], σ_1 has a linear-T dependence in the low temperature regime at microwave frequencies, as shown in Fig. 4.46. Fig. 4.46 (solid line) shows the fitting result of σ_1 of YBCO single crystal measured at f=1.14GHz with the formula, $\sigma_1 = \sigma_1(5K)[(1 - Ae^{-c_1 \cdot T_c / T}) + a' \dfrac{T}{T_c}]$ at T<50 K. And the fitting parameters are $c_1 = 1.13 \pm 0.02$, $A = 174.11 \pm 6.56$ and $a' = 42.44 \pm 0.44$ We conclude that $\sigma_1 = \sigma_1(5K)[(1 - Ae^{-c_1 \cdot T_c / T}) + a' \dfrac{T}{T_c}]$ is a reasonable formula to fit the conductivity $\sigma_1(T)$ which has a linear-T dependence in the low temperature for the thin films or

single crystals in the clean limit. And we speculate that the linear-T dependence in $\sigma_1(T)$ is originated from the delocalized quasiparticles. So, in this case, there are two distinct phases of the samples in the clean limit: the thermal-metal and the thermal-insulator, as well as the samples of Hardy's group for high-purity single crystals.

4.3.2 Imaginary Part Conductivity

In order to compare with the real part of microwave conductivity σ_1, we also report the temperature dependence of the imaginary part of microwave conductivity $\sigma_2(T)$ of the YBCO and Ca-YBCO films, as shown in Figs. 4.47(a) and 4.47(b). Fig. 4.47(a) shows the temperature dependence of the imaginary part of microwave conductivity $\sigma_2(T)$ with various hole concentrations by controlling oxygen contents for the same YBCO ring resonator and the value of $\sigma_2(T)$ increases as T decreasing at T<Tc. The value of $\sigma_2(T)$ also decreases with decreasing hole concentrations p. In Fig. 4.47(b), we show the temperature dependence of the imaginary part of microwave conductivity $\sigma_2(T)$ for the same Ca-YBCO ring resonator with various hole concentrations and the value of $\sigma_2(T)$ increases as T decreasing at T<T$_c$. Also, the value of $\sigma_2(T)$ increases with decreasing p in the overdoped regime and it decreases with decreasing p in the underdoped regime. The order of magnitude for σ_2 of these samples is at least one order of magnitude larger than the one of σ_1. In Fig. 4.48, we plot the normalized conductivity $\sigma_2/\sigma_2(5K)$ vs T_c/T, which indicates the universal behavior of the conductivity σ_2 having the same intrinsic properties in our ring resonators. It shows a unique property that the onset of the rapid decrease in σ_2 due to thermal fluctuations dominates the behavior in σ_2 at 0.5Tc<T. Then, we take the formula, $\sigma_2 = \sigma_2(5K)(1 - Be^{-c_2 \cdot T_c/T})$ to fit the

experimental data by least square fitting of the "OriginR 7.0 SR0" program, where B

and c_2 are two fitting parameters. Here $\sigma_2(5K)$ is the measured microwave

conductivity at 5K. The fitting result is shown in Table 4.8. In Figs. 4.49(a)-(d) (solid

lines), we show the fitting curves with the formula, $\sigma_2 / \sigma_2(5K) = 1 - Be^{-c_2 \cdot T_c / T}$ for

the YBCO and Ca-YBCO ring resonators, respectively. In Fig. 4.49(a) (solid line), the

fitting curve with the fitting parameters $B = 3.04 \pm 0.08$ and $c_2 = 1.18 \pm 0.02$ for

the YBCO ring resonator with p=0.16 is shown. Fig. 4.49(b) shows the fitting curve

for the YBCO ring resonator with p=0.098. Figs. 4.49(c) and 4.49(d) show the fitting

curves for the Ca-YBCO ring resonator with p=0.218 and p=0.121, respectively. We

can define $c_2 \cdot T_c = E_{g2}(0)$ (or $c_2 \cdot k_B T_c = E_{g2}(0)$ in unit of meV) which is a

thermal activation gap at 0K. And when $\sigma_2(T)$ is equal to zero, we can have another

characteristic temperature $T_{\sigma2}^*$ from the equivalent $1 = Be^{-c_2 \cdot T_c / T_{\sigma2}^*}$. The doping

dependence of $T_{\sigma2}^*$, $E_{g2}(0)$ and T_c is shown in Fig. 4.50, where the p-dependent

properties of $T_{\sigma2}^*$, $E_{g2}(0)$ and T_c are also very similar to the phase diagram reported

by Emery and Kivelson [88]. In fact, in the underdoped regime, the p-dependence of

$E_{g2}(0)$ and $T_{\sigma2}^*$ are similar to the upper bound on the phase ordering temperature

(T_θ^{max}). And in the overdoped regime, the p-dependence of $E_{g2}(0)$ and $T_{\sigma2}^*$ are

resembled to the mean-field transition temperature. These results give an compelling

evidence that the thermal fluctuations plays an important role in high Tc

superconductivity. The thermal activation gap $E_{g2}(T)$ at 0K is also observed in our

thin film structure. Furthermore, the formula $\sigma_2(5K)(1 - Be^{-c_2 \cdot T_c / T})$ can also be

rewritten as a simple form, $\sigma_2(5K)(1 - e^{-E_{g2}(T)/k_B T})$. The formula clearly takes up

the thermal activation gap as $E_{g2}(T) = E_{g2}(0) - E_{g2}(0) \times \dfrac{T}{T^*_{\sigma2}}$, which is a linear

dependence of temperature. From the physical point of view, the term $e^{-E_{g2}(T)/k_B T}$

can be attributed to as a probability weight due to lose of phase memory. As compared

to the classical thermal fluctuation model of the Emery and Kivelson 's theory, the

values of $T^*_{\sigma2}$ could be viewed as T^{max}_θ, which are larger than T_c but smaller than

$E_{g2}(0)$, and we also have $\dfrac{T^{max}_\theta}{T_c}$ is close to unity in all our samples. The result

indicates that the classical phase fluctuations is seemly very important in the

destruction of phase coherence of the long-range order parameter.

The temperature dependence of the imaginary part of the microwave

conductivity, σ_2, for the YBCO and Ca-YBCO microstrip line resonators with various

hole concentrations are shown in Figs. 4.51(a) and 4.51(b). The value of σ_2 increases

as decreasing T at $T<T_c$ for all doping levels. Fig. 4.52 shows the plot of $\sigma_2/\sigma_2(5K)$

versus T_c/T for the YBCO and Ca-YBCO microstrip line resonators with various hole

concentrations. In Figs. 4.53(a)-(d) (solid lines), we show the fitting curves with the

formula, $\sigma_2/\sigma_2(5K) = 1 - Be^{-c_2 \cdot T_c/T}$ for the YBCO and Ca-YBCO microstrip line

resonators, respectively. In Fig. 4.53(a) (solid line), the fitting curve with the fitting

parameters $c_2 = 1.16 \pm 0.01$ and $B = 3.07 \pm 0.05$ for the YBCO microstrip line

resonator with p=0.148 is shown. Fig. 4.53(b) shows the fitting curve for the YBCO

microstrip line resonator with p=0.09. Figs. 4.53(c) and 4.53(d) show the fitting

curves for the Ca-YBCO microstrip line resonator with p=0.217 and p=0.078,

respectively. The detailed fitting parameters are listed in Table 4.9. In Fig. 4.54, the

doping dependence of the characteristic energy scale $E_{g2}(0)$ and T_c of the YBCO

and Ca-YBCO thin films was obtained from the fitting of σ_2 for the microstrip ring

(full square) and line (full diamond) resonators. It is evident that $E_{g2}(0)$ is larger

than T_c for all doping levels and similar to the "superconducting dome" of T_c versus p.

Fig. 4.55(a) shows the doping dependence of the characteristic energy scale $T_{\sigma 2}^*$ of

the YBCO and Ca-YBCO thin films for the microstrip ring (full square) and line (full

diamond) resonators. It is clearly that $T_{\sigma 2}^*$ is a little larger but close to T_c, i.e.

$\dfrac{T_{\sigma 2}^*}{T_c} \approx 1$. Comparing with the phase diagram sketched by Emery and Kivelson [88], as

shown in Fig. 4.55(b), the same systematically tendency for $T_{\sigma 2}^*$, $T_\theta^{\max}$ and T^{MF}

was shown. Hence, we propose that $T_{\sigma 2}^*$ would be the upper bound on the phase

ordering temperature $T_\theta^{\max}$ in the underdoped regime, and in the overdoped regime,

$T_{\sigma 2}^*$ corresponding to the mean field transition temperature T^{MF}.

As revealed by Lee's model, we have put the universal conductance $\dfrac{e^2}{2\pi\hbar}$ in

our microwave conductivity $\sigma_1(5K)$ in such disordered system, and sketched

various energy scales which describe the physical properties of the quasiparticles

when the quasiparticles are in the localized states. According to this, it gives us

another inspiration on explaining $\sigma_2(5K)$ related to the universal conductance $\dfrac{e^2}{2\pi\hbar}$.

Because $\sigma_2(5K)$ is the meaning of Josephson tunneling, we propose

$\sigma_2(5K) = \dfrac{(e^*)^2}{2\pi\hbar} \dfrac{v_F}{v_2} \gamma/\zeta$, where $e^* = 2e$. The experimental result gives that the

average value of γ is around 2 (see in Fig. 4.56), which is almost twice of the β

value extracted from the $\sigma_1(5K)$ measurements. No matter what, all of the results

reveal that σ_1 and σ_2 approach the universal value $\dfrac{e^2}{2\pi\hbar}$ via macroscopic

quantum tunneling in the low temperature limit in our thin film samples.

Table 4.8. Some parameters for YBCO and Ca-YBCO ring resonators are obtained from the numerical fitting of the imaginary-part conductivity σ_2.

	Hole concentrations p	$\lambda(5K)$ nm	c_2	B	$E_{g2}(0)\,(K)$	$T_{\sigma 2}^{*}\,(K)$
YC010105A YBCO	0.160	145.7±0.8	1.18±0.02	3.04±0.08	107.3±1.8	96.5±2.8
	0.148	150.7±0.3	1.32±0.02	3.30±0.09	118.8±1.8	99.5±2.7
	0.134	162.2±0.2	1.28±0.02	3.19±0.09	110.0±1.7	94.8±2.7
	0.098	171.6±0.4	1.25±0.02	2.96±0.11	78.7±1.2	72.5±2.7
	0.090	195.7±0.2	1.40±0.03	3.56±0.14	76.3±1.6	60.0±2.2
	0.074	272.0±0.3	1.36±0.03	3.29±0.13	49.5±1.0	41.5±1.6
Ca-Y040305A Ca-YBCO	0.218	212.0±2.3	1.43±0.02	4.52±0.17	85.8±1.2	56.8±1.6
	0.207	155.3±0.4	1.43±0.03	4.02±0.15	97.9±2.0	70.4±2.3
	0.188	151.3±0.2	1.14±0.01	2.93±0.07	89.4±0.7	83.2±1.9
	0.121	188.4±0.2	1.28±0.03	3.17±0.11	94.0±2.2	81.5±3.1
	0.111	202.7±0.2	1.32±0.03	3.37±0.14	89.7±2.0	73.8±3.0
	0.088	270.4±1.4	1.36±0.02	3.80±0.12	65.9±0.9	49.4±1.3

Table 4.9. Some parameters for the YBCO and Ca-YBCO microstrip line resonators are obtained from the numerical fitting of the imaginary-part conductivity σ_2.

	Hole concentrations p	$\lambda(5K)$ nm	c_2	B	$E_{g2}(0)$ (K)	$T_{\sigma2}^*$(K)
YC020309A YBCO	0.148	195.4±0.8	1.16±0.01	3.07±0.05	104.4±0.9	93.0±1.5
	0.106	242.0±0.7	1.05±0.01	2.60±0.04	72.9±0.6	76.3±1.4
	0.090	234.1±0.8	1.24±0.03	3.00±0.12	67.5±1.6	61.5±2.6
YC050109A YBCO	0.148	202.5±0.4	1.11±0.01	2.82±0.06	99.9±0.9	96.3±2.1
	0.085	255.7±2.2	1.26±0.02	3.50±0.13	61.7±0.9	49.2±1.6
	0.064	348.3±5.5	1.02±0.01	2.26±0.05	22.4±0.2	27.5±0.7
YC050514A YBCO	0.148	194.3±0.8	1.21±0.02	2.97±0.08	108.9±1.8	100.0±2.9
	0.122	219.6±2.9	*	*	*	*
YC050705A YBCO	0.148	193.1±1.4	1.38±0.01	3.58±0.08	124.2±0.9	97.3±1.8
	0.080	217.9±1.4	1.19±0.03	2.54±0.10	51.1±1.2	54.8±2.7
Ca-Y050406A Ca-YBCO	0.217	211.7±6.2	1.74±0.03	5.14±0.24	106.1±1.8	64.8±2.1
	0.197	166.4±1.1	1.32±0.01	3.52±0.08	98.3±0.7	78.1±1.5
	0.103	224.9±1.0	1.29±0.03	3.26±0.14	79.9±1.8	67.6±2.9
	0.092	227.9±0.9	1.28±0.03	3.21±0.14	67.2±1.5	57.6±2.5
	0.082	240.0±1.8	1.15±0.01	2.90±0.06	48.8±0.4	45.9±0.9
	0.078	256.0±2.6	1.16±0.01	2.91±0.06	43.5±0.3	40.7±0.8
Ca-Y050527A Ca-YBCO	0.197	161.5±2.0	1.27±0.01	3.12±0.07	94.6±0.7	83.1±1.7
	0.093	250.6±5.5	1.51±0.04	3.86±0.20	80.0±2.1	59.2±2.7
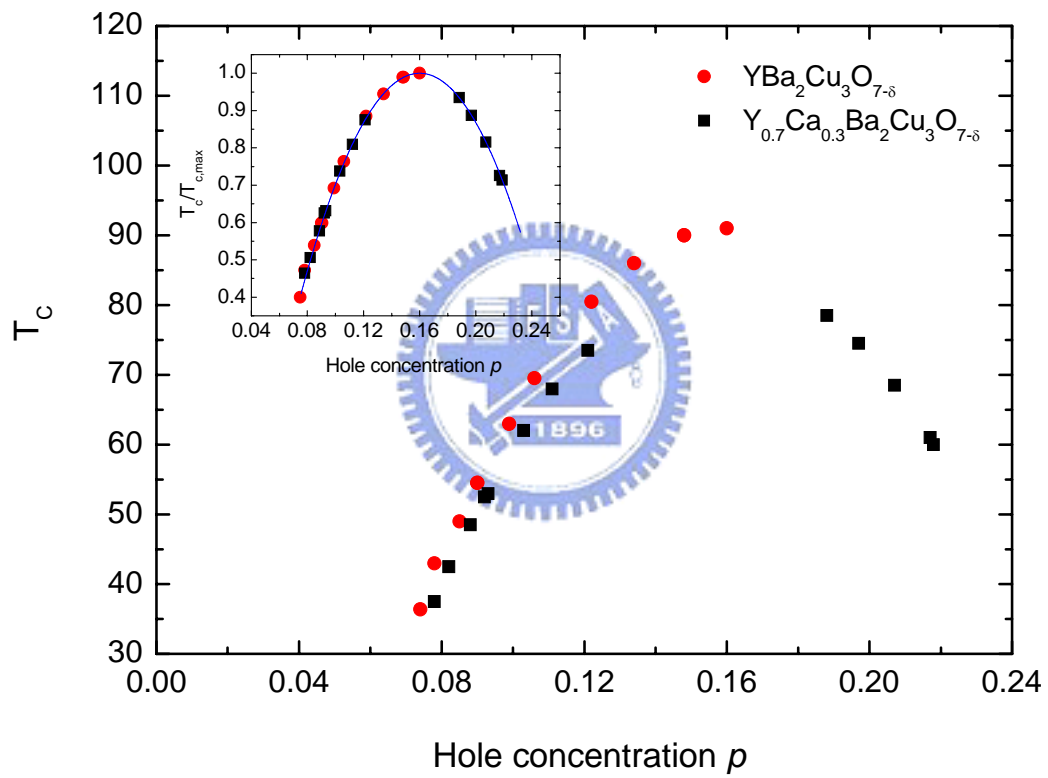
Fig. 4.1. The hole concentrations of the YBa$_2$Cu$_3$O$_{7-\delta}$ and the Y$_{0.7}$Ca$_{0.3}$Ba$_2$Cu$_3$O$_{7-\delta}$ thin films are obtained by using the empirical relation T$_c$/T$_{c,max}$=1-82.6(p-0.16)^2. Here T$_{c,max}$ for YBa$_2$Cu$_3$O$_{7-\delta}$ thin film is taken as 91K and the one for Y$_{0.7}$Ca$_{0.3}$Ba$_2$Cu$_3$O$_{7-\delta}$ thin film is taken as 84K.
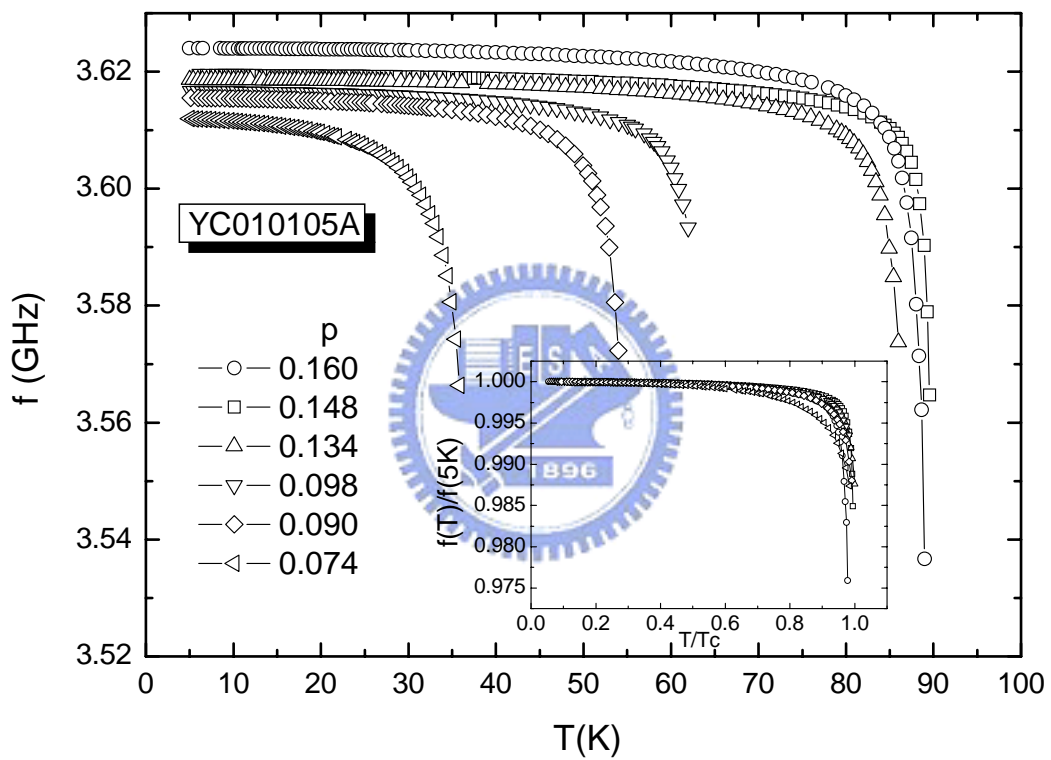
Fig. 4.2. The temperature dependence of resonance frequency f(T) of the ring resonator for the YBCO thin film with various hole concentrations *p*.
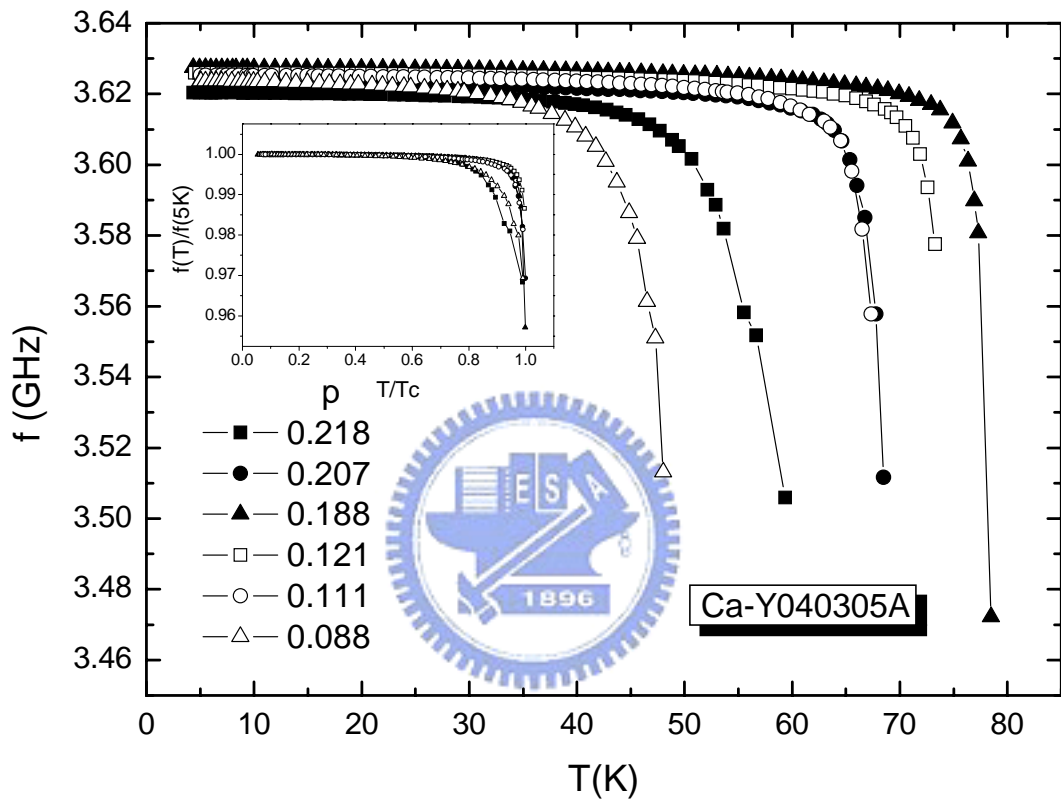
Fig. 4.3. The temperature dependence of resonance frequency f(T) of the ring resonator for the Ca-YBCO thin film with various hole concentrations *p*.
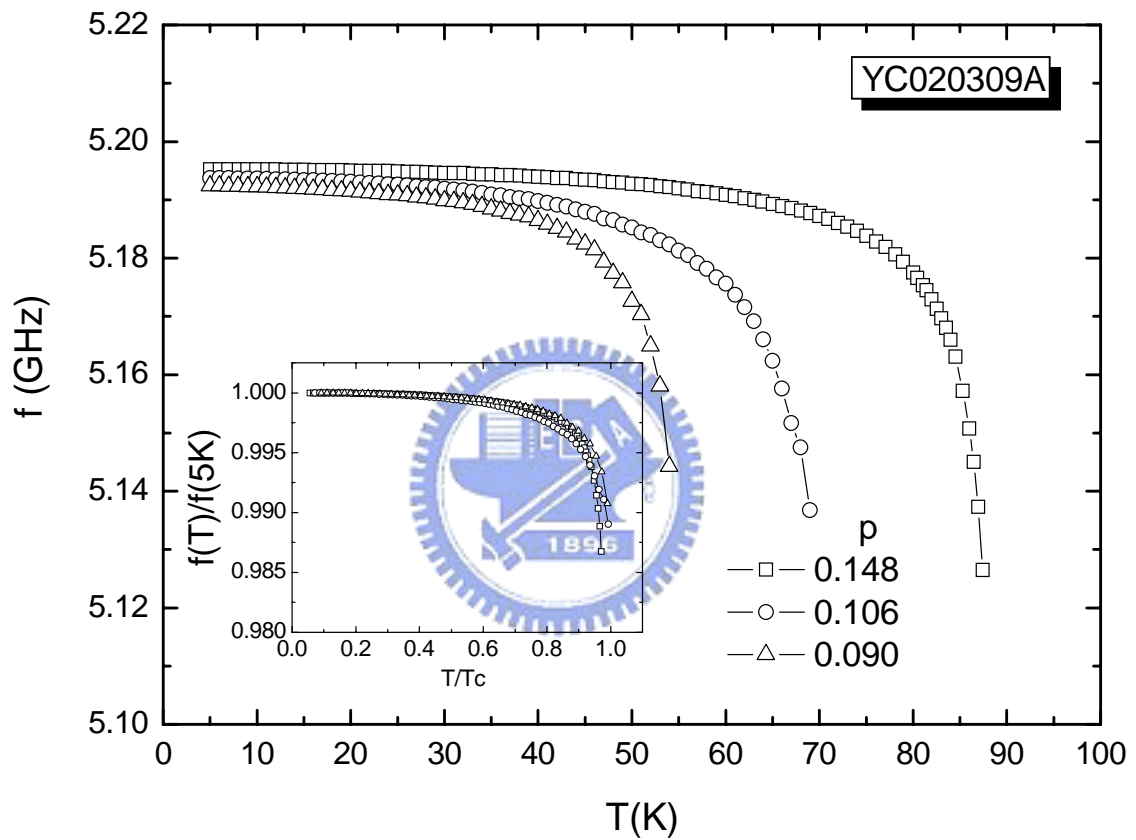
Fig. 4.4. The temperature dependence of resonance frequency f(T) of the microstrip line resonator for the YBCO thin film with various hole concentrations p.
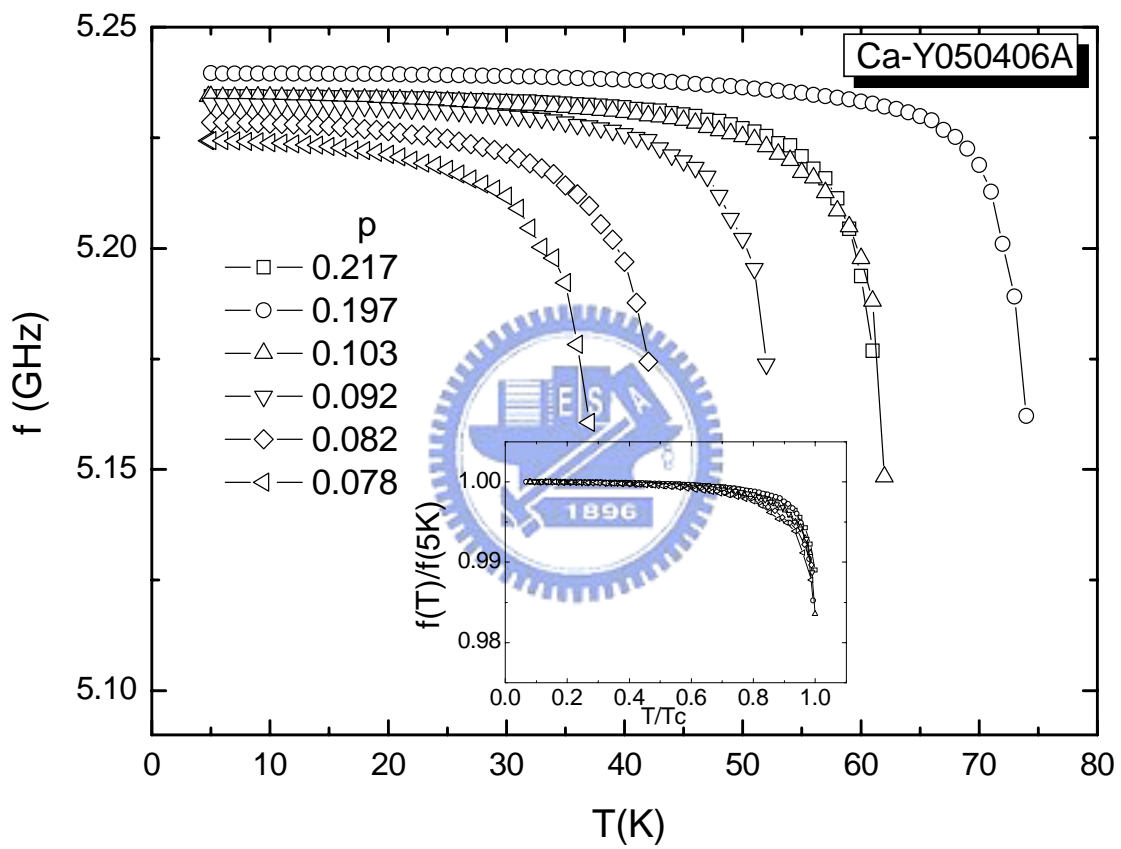
Fig. 4.5. The temperature dependence of resonance frequency f(T) of the microstrip line resonator for the Ca-YBCO thin film with various hole concentrations *p*.
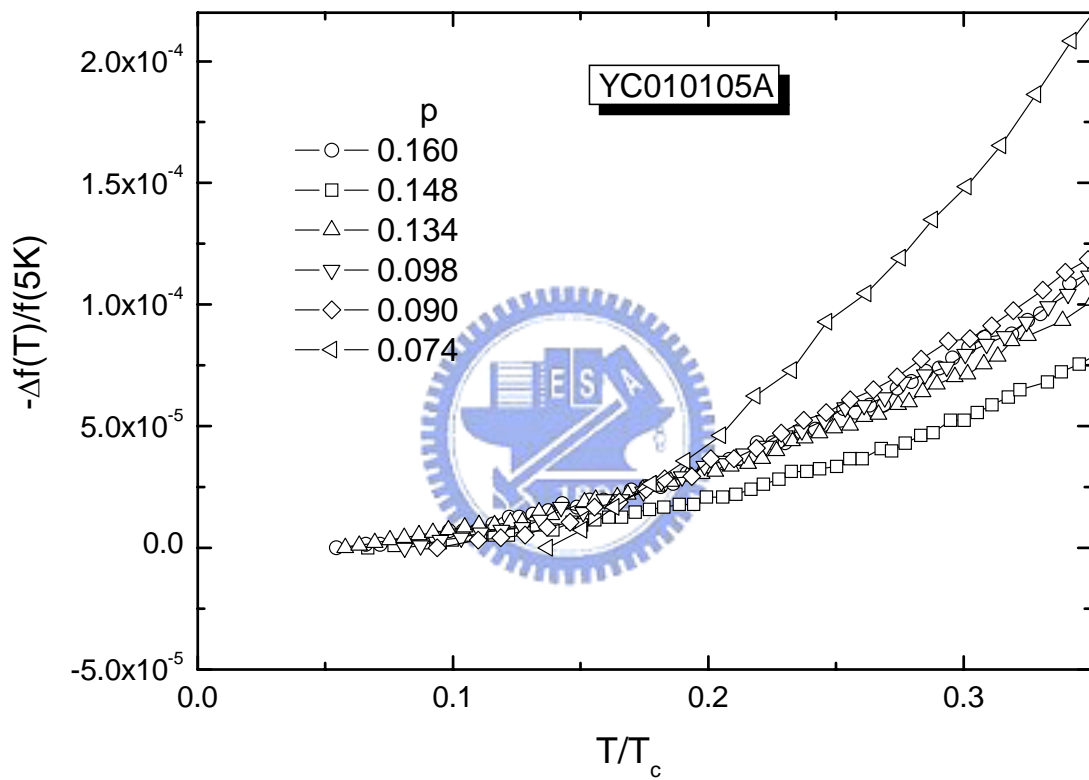
Fig. 4.6. The normalized temperature dependence of the change of resonance frequency $-\Delta f(T)/f(5K)=1-f(T)/f(5K)$ for the YBCO ring resonator with various hole concentrations p.
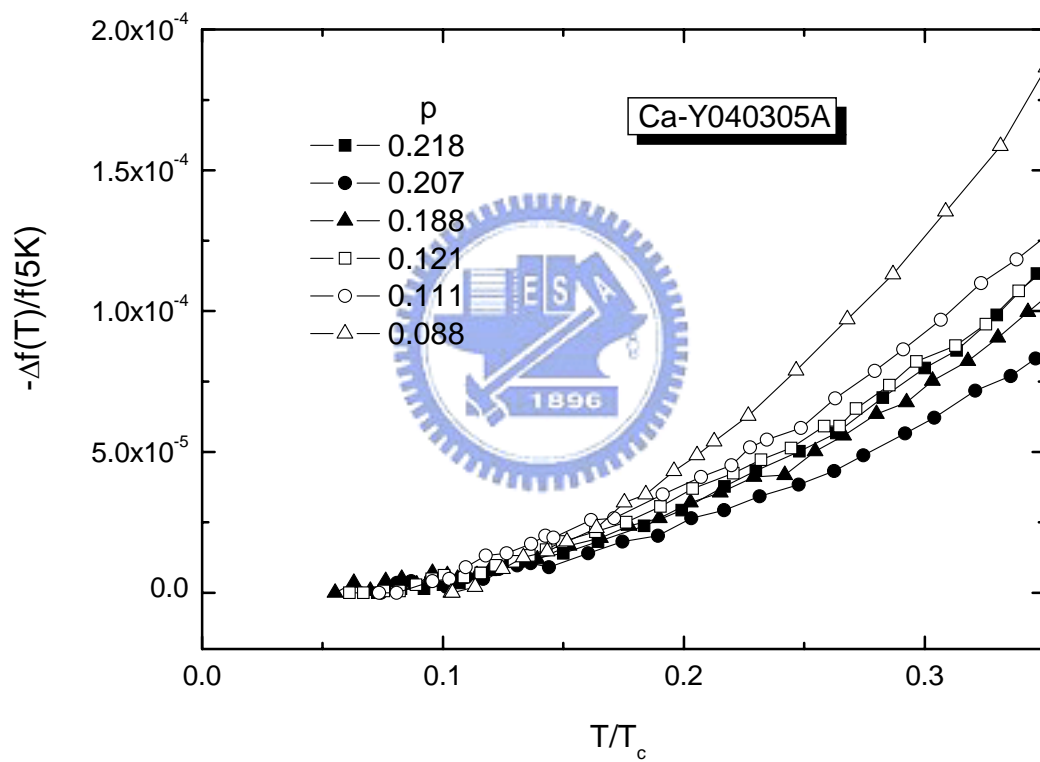
Fig. 4.7. The normalized temperature dependence of the change of resonance frequency $-\Delta f(T)/f(5K)=1-f(T)/f(5K)$ for the Ca-YBCO ring resonator with various hole concentrations p.

132
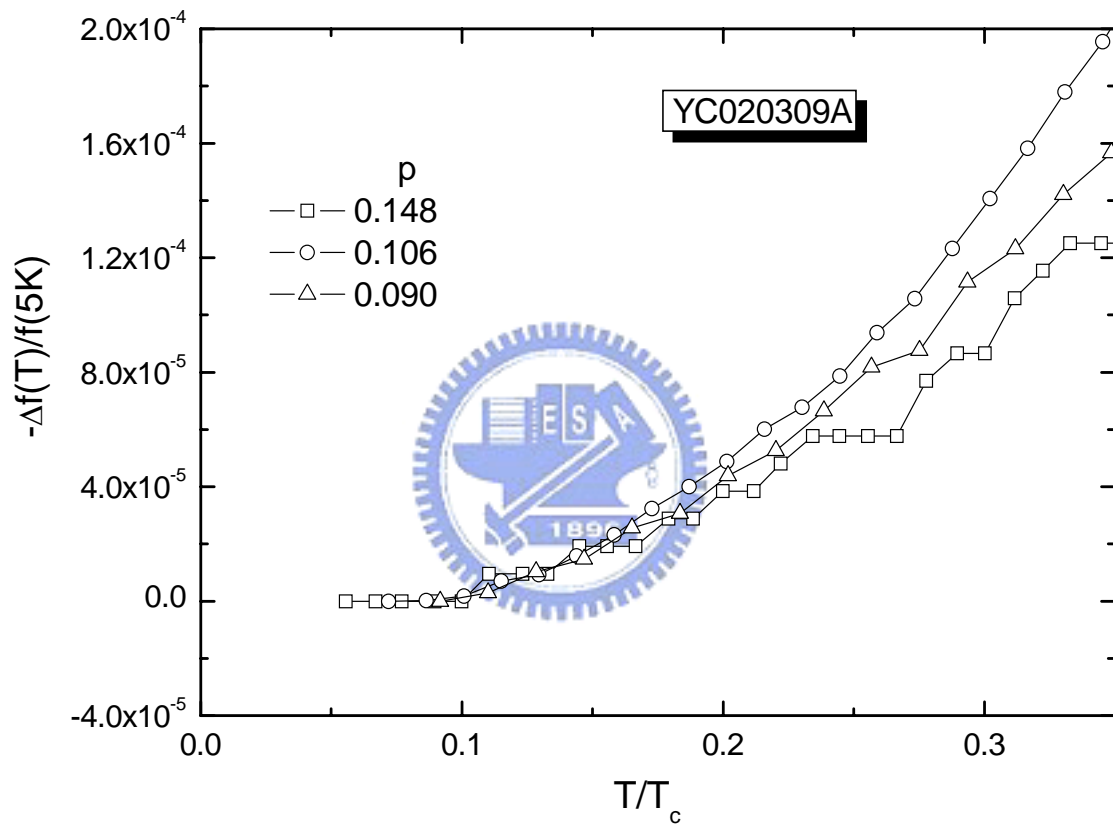
Fig. 4.8. The normalized temperature dependence of the change of resonance frequency $-\Delta f(T)/f(5K)=1-f(T)/f(5K)$ of the microstrip line resonator for the YBCO film with various hole concentrations p.
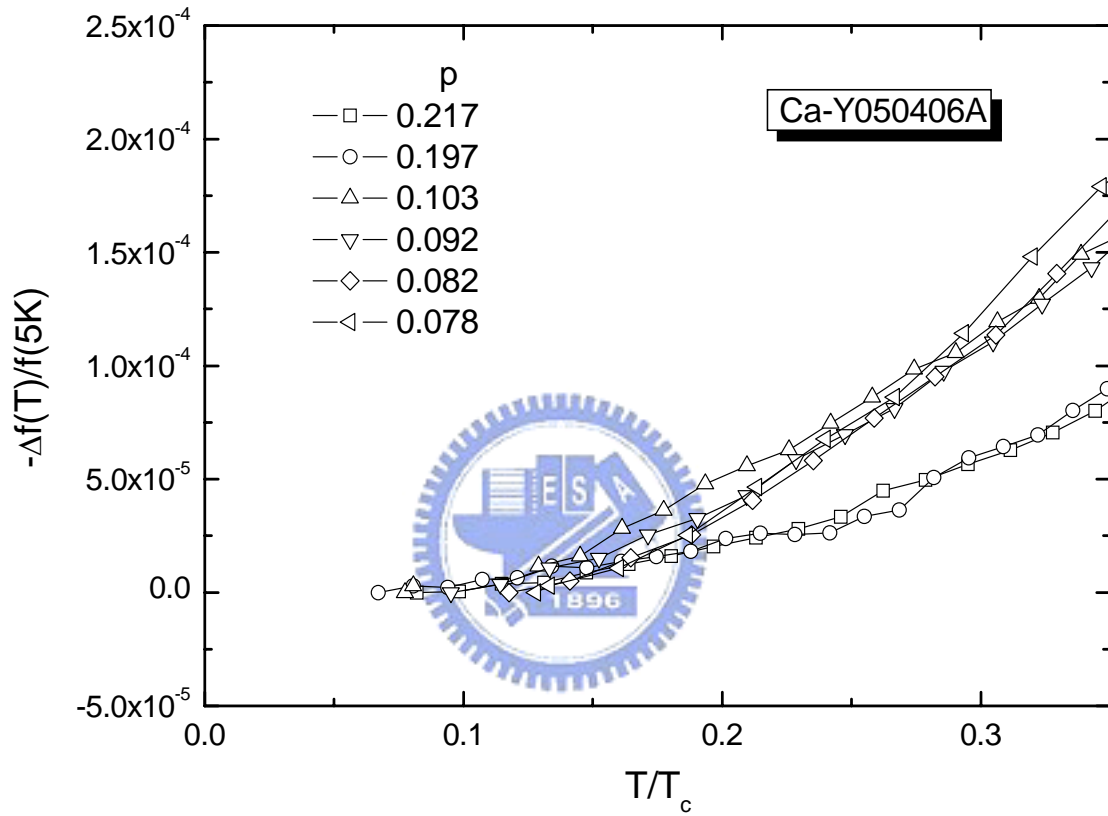
Fig. 4.9. The normalized temperature dependence of the change of resonance frequency $-\Delta f(T)/f(5K)=1-f(T)/f(5K)$ of the microstrip line resonator for the Ca-YBCO film with various hole concentrations p.
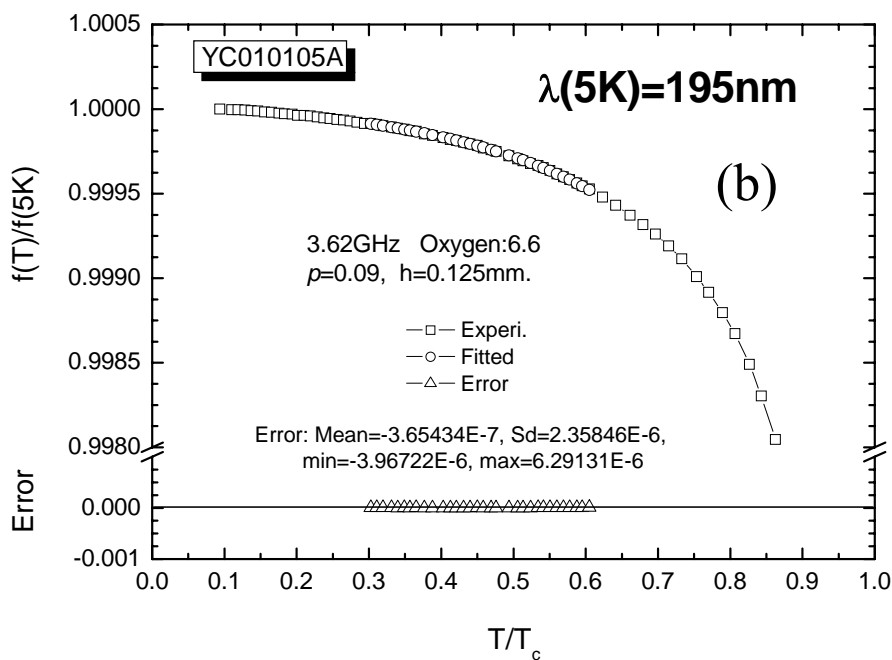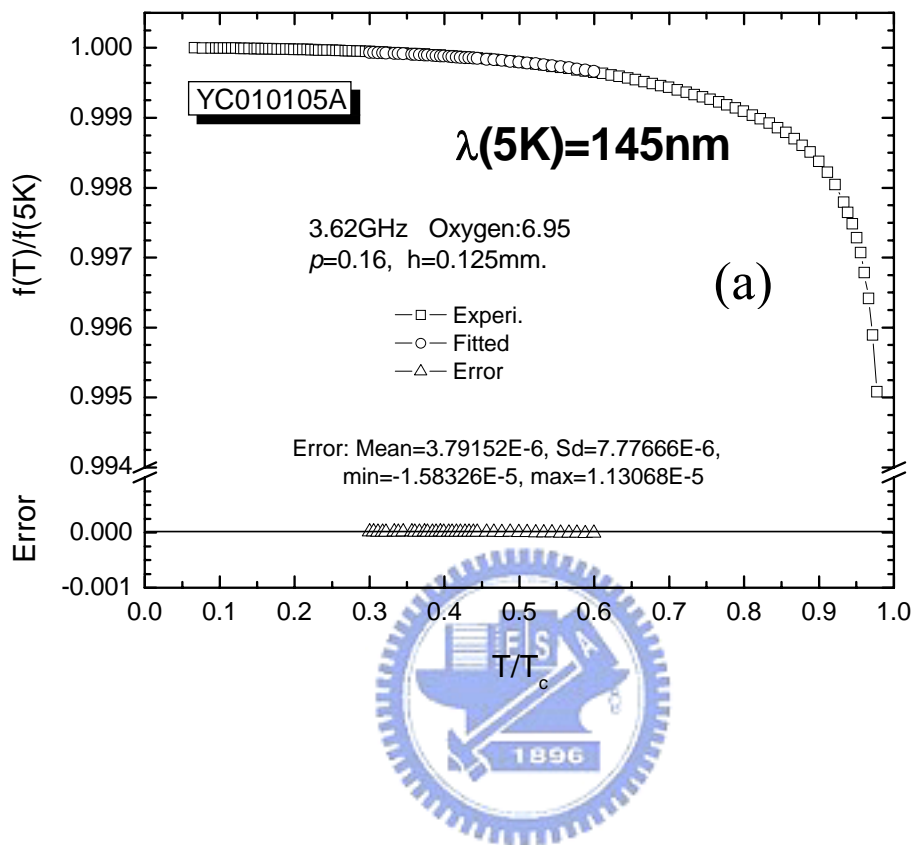
Fig. 4.10. The normalized temperature dependence of the resonance frequency f(T)/f(5K) for the YBCO ring resonators with (a) p=0.16 and (b) p=0.09, respectively.

135
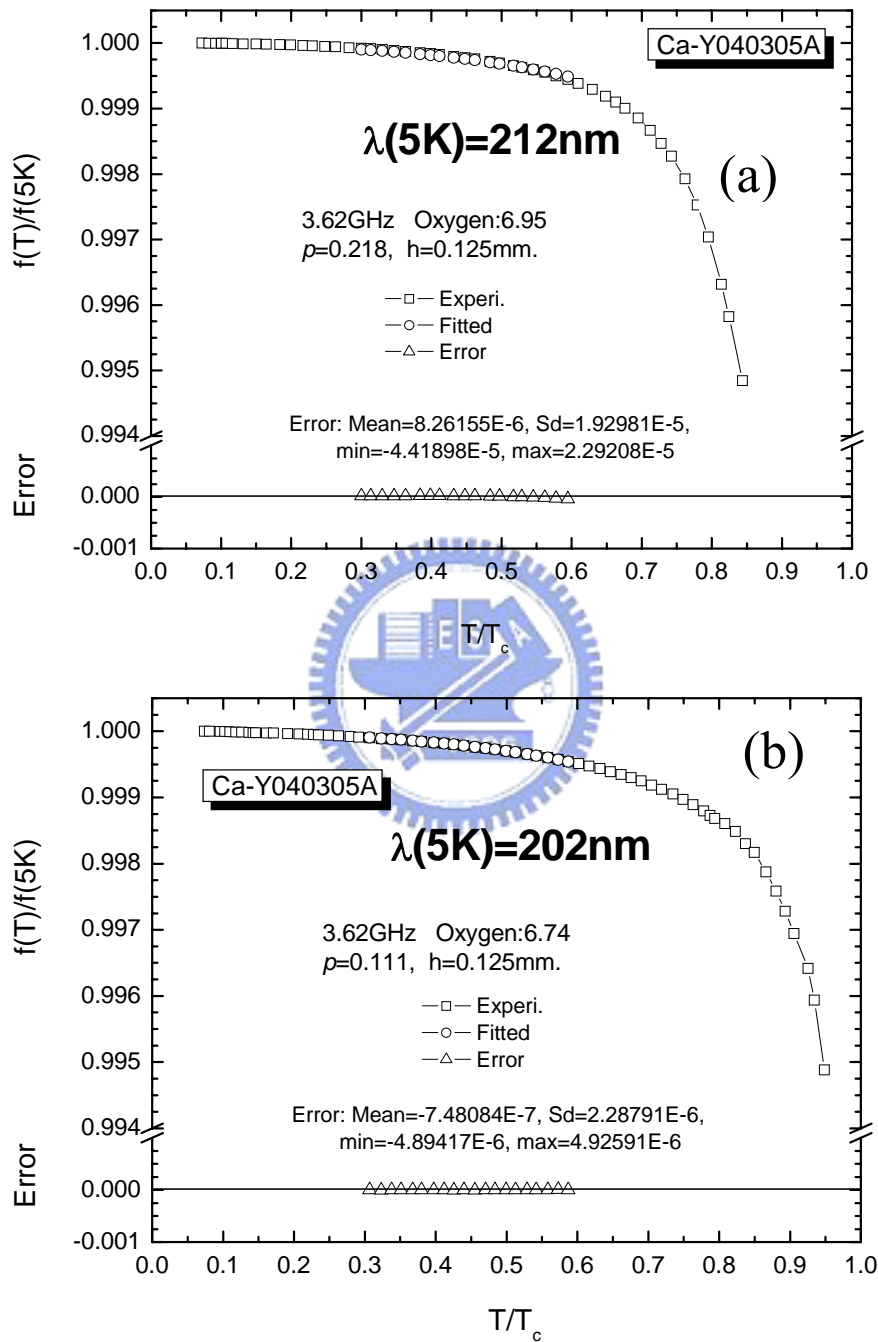
Fig. 4.11. The normalized temperature dependence of the resonance frequency f(T)/f(5K) for the Ca-YBCO ring resonator with (a) p= 0.218 and (b) p= 0.111, respectively.
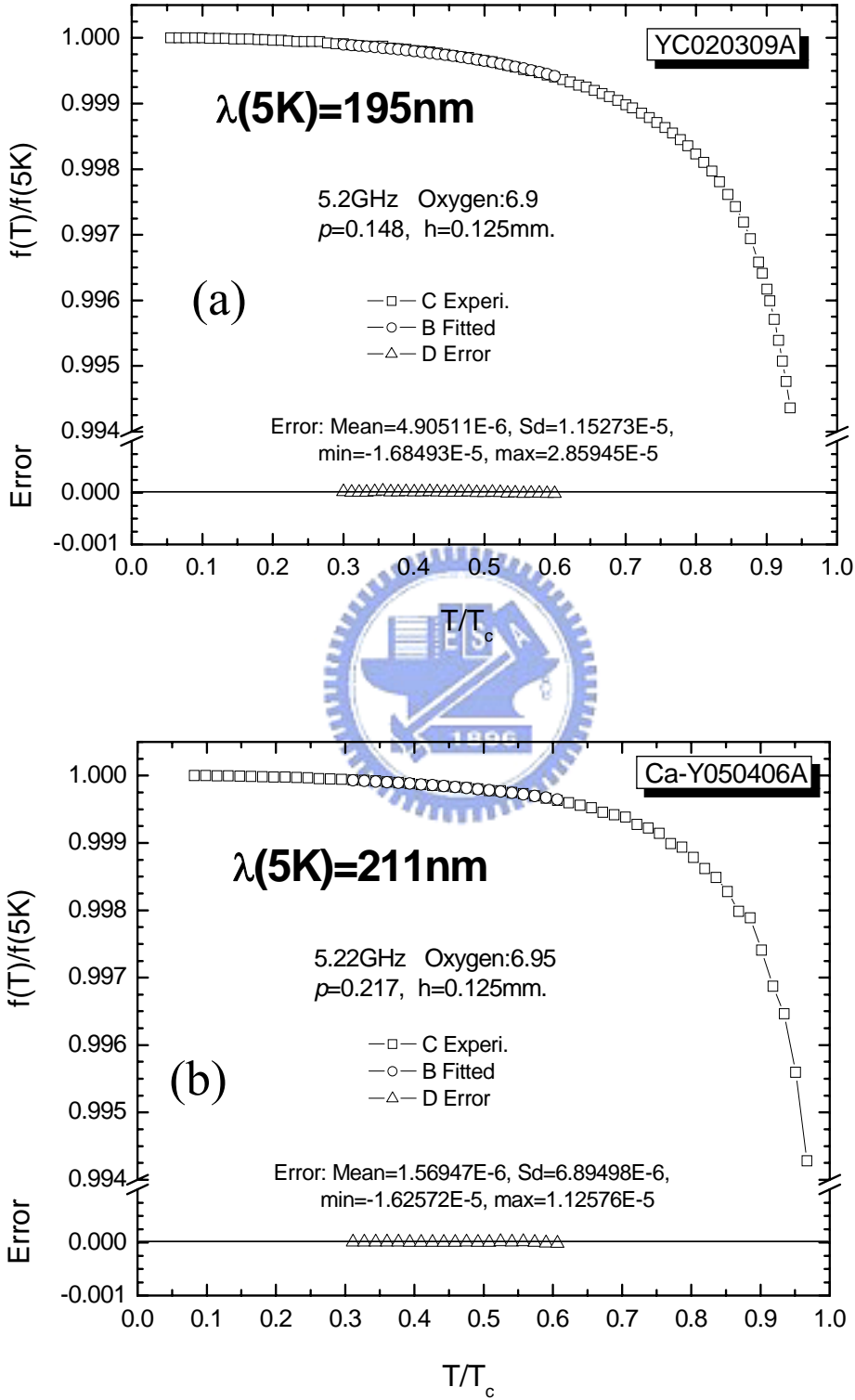
Fig. 4.12. The normalized temperature dependence of the resonance frequency f(T)/f(5K) of the microstrip line resonators for (a) the YBCO thin film with p =0.148 and (b) the Ca-YBCO thin film with p = 0.217, respectively.

137
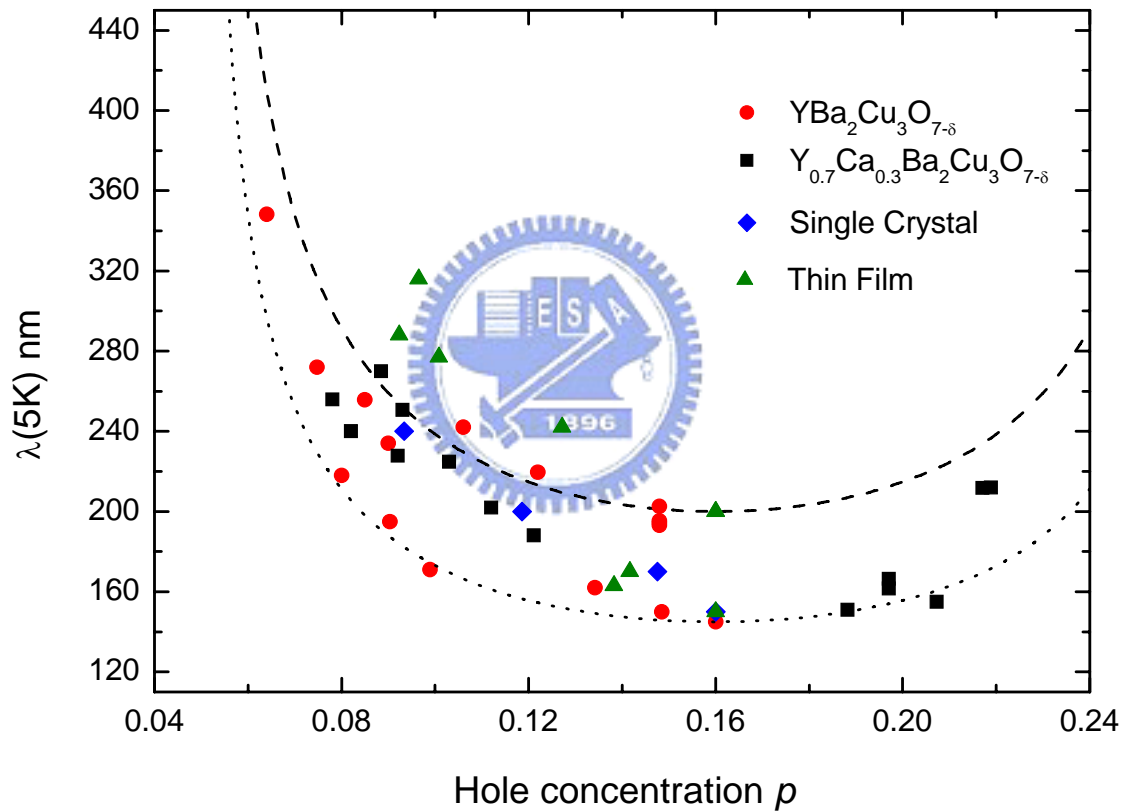
Fig. 4.13. Doping dependence of the a-b plane penetration depth $\lambda(5K)$. By using the Uemura relation, $n_s \propto T_c$, and the empirical formula $T_c/T_{c,max} = 1 - 82.6(p-0.16)^2$, one can obtained the doping dependence of $T_c(p)$. The dashed line is represented as $\lambda(p) = 200 \times (1 - 82.6(p-0.16)^2)^{-0.5}$. The dotted line is represented as $\lambda(p) = 145 \times (1 - 82.6(p-0.16)^2)^{-0.5}$.
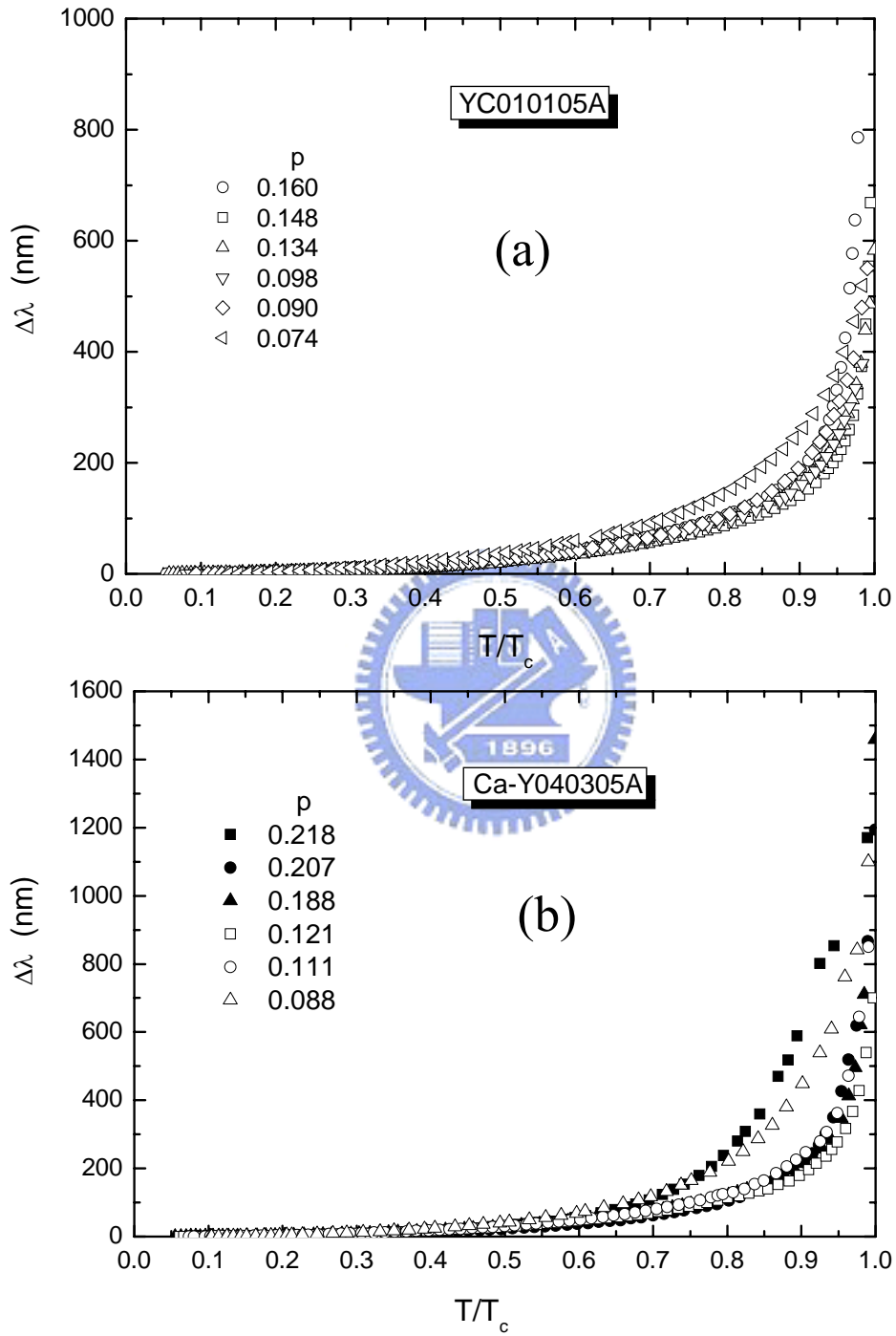
Fig. 4.14 The normalized temperature dependence of the change of the penetration depth $\Delta\lambda$ for the (a) YBCO and (b) Ca-YBCO microstrip ring resonators with various hole concentrations p.
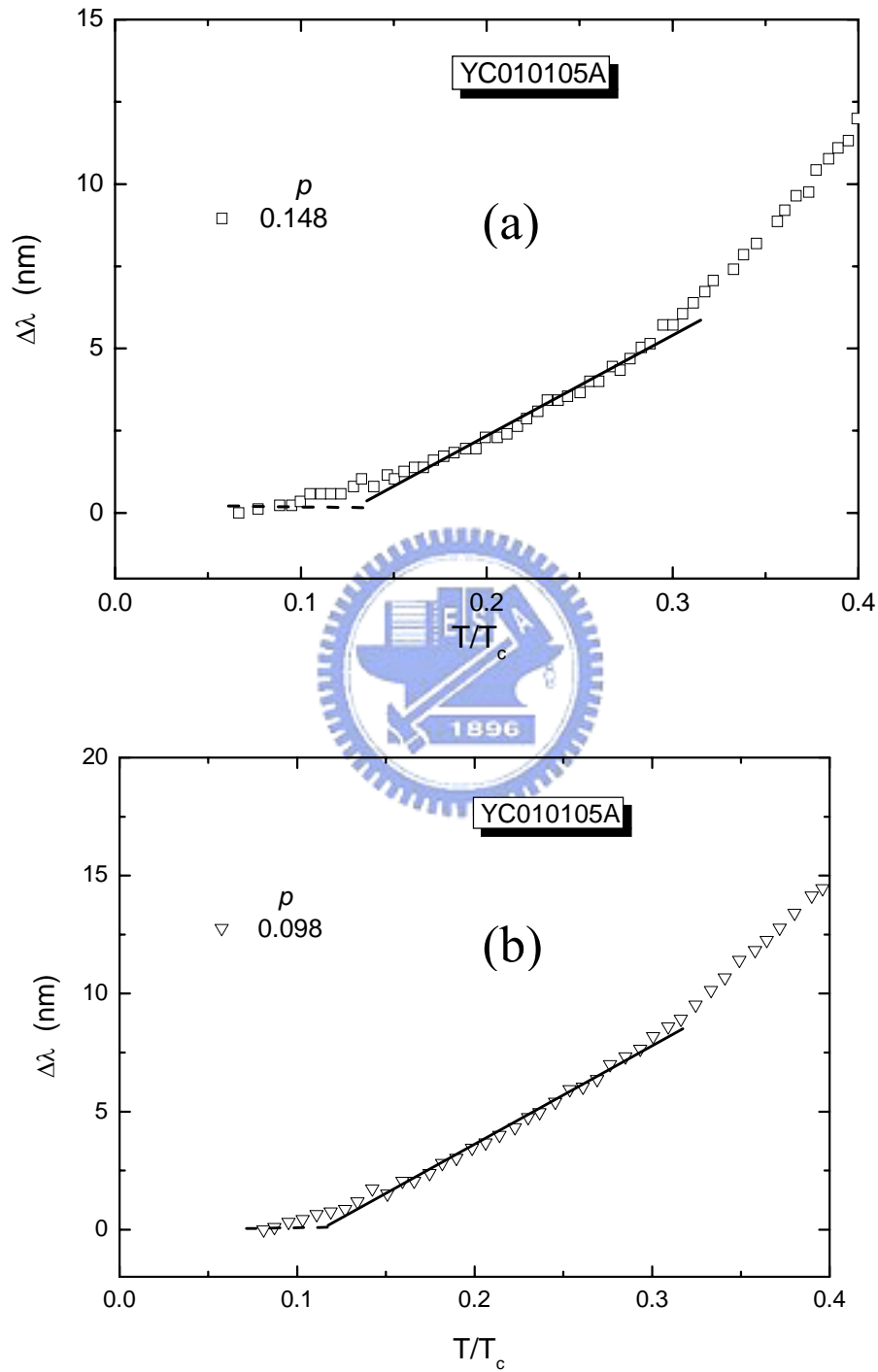
Fig. 4.15 The normalized temperature dependence of the change of the penetration depth $\Delta\lambda$ for the YBCO ring resonator with (a) $p = 0.148$ and (b) $p=0.098$, respectively.
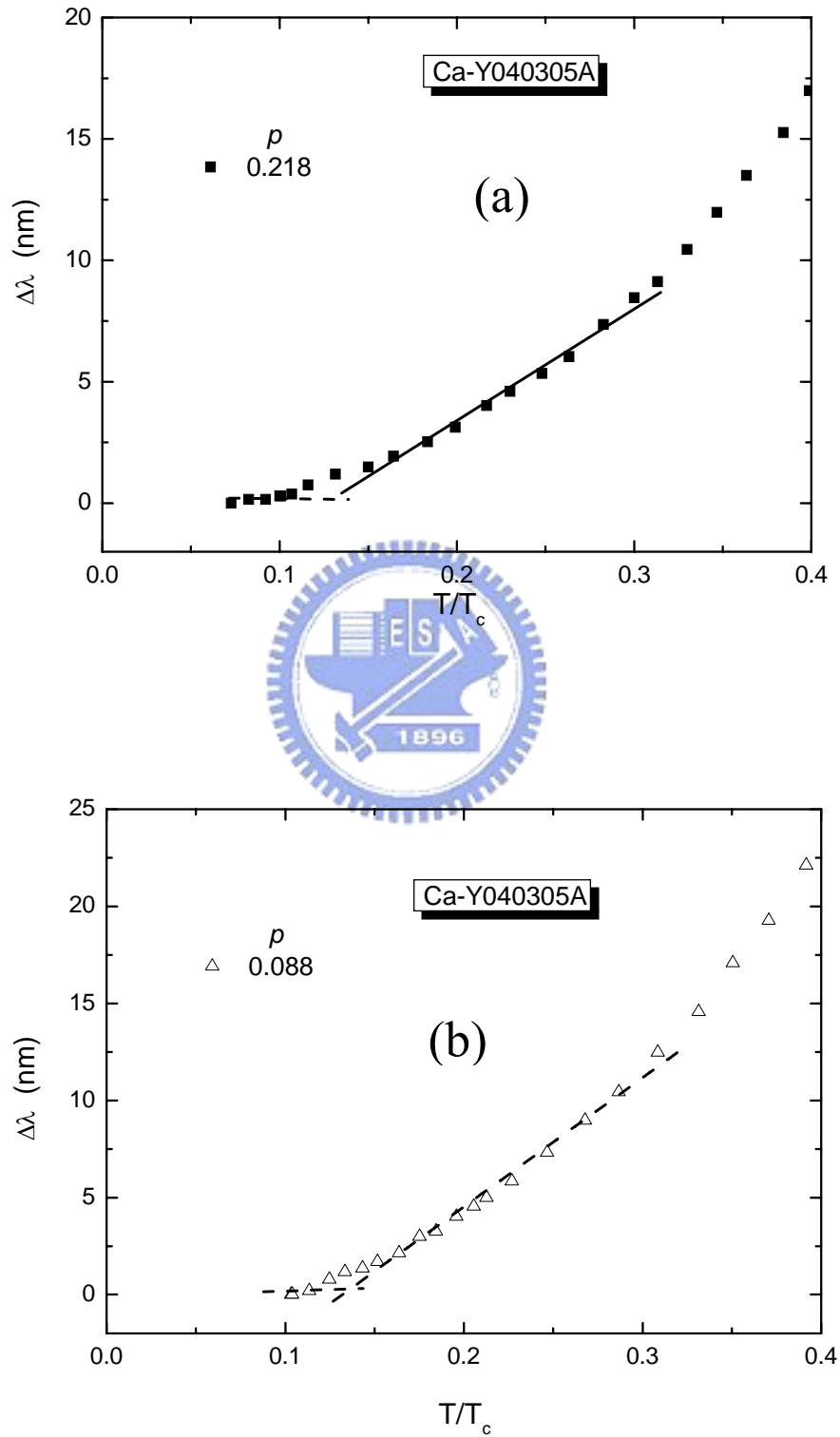
Fig. 4.16 The normalized temperature dependence of the change of the penetration depth $\Delta\lambda$ for the Ca-YBCO ring resonator with (a) p= 0.218 and (b) p=0.088, respectively.
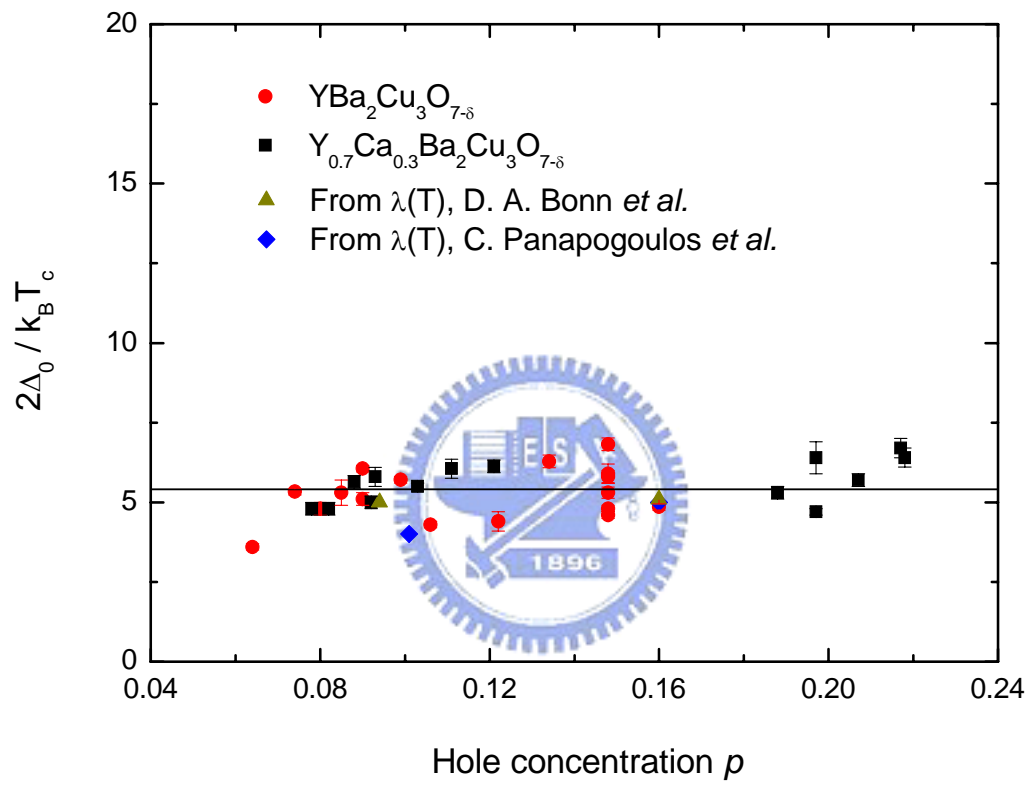
Fig. 4.17. The doping dependence of the $2\Delta_0/k_BT_c$ obtained from the BCS d-wave model for the YBCO and Ca-YBCO films. The average value (solid line) and the error bar of the all experimental data, $2\Delta_0/k_BT_c$ is 5.4 and 0.7, respectively.
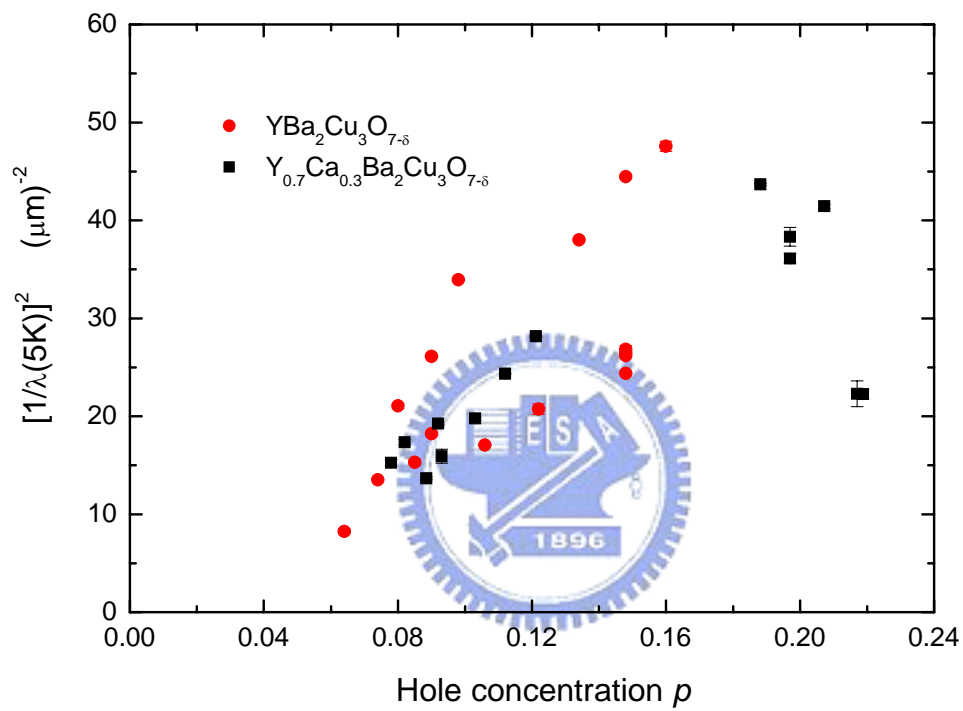
Fig. 4.18. The $1/\lambda^2$(5K) vs p for the $Y_{0.7}Ca_{0.3}Ba_2Cu_3O_{7-\delta}$ and the $YBa_2Cu_3O_{7-\delta}$ thin films. Obviously, in the underdoped regime, it increases as increasing p. However, in the overdoped regime, it decreases as increasing p.
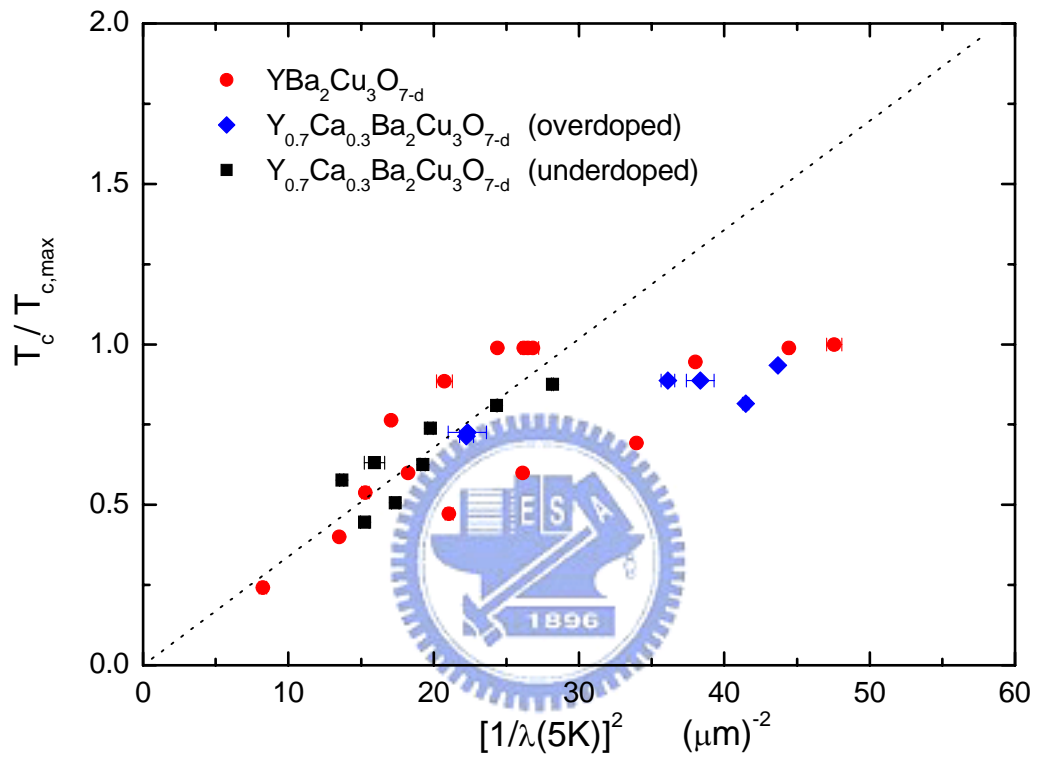
Fig. 4.19. The $T_c/T_{c,max}$ vs $1/\lambda^2(5K)$ for the $Y_{0.7}Ca_{0.3}Ba_2Cu_3O_{7-\delta}$ and the $YBa_2Cu_3O_{7-\delta}$ thin films. The dotted line shows the Uemura relation, $T_c \propto 1/\lambda^2(5K)$.
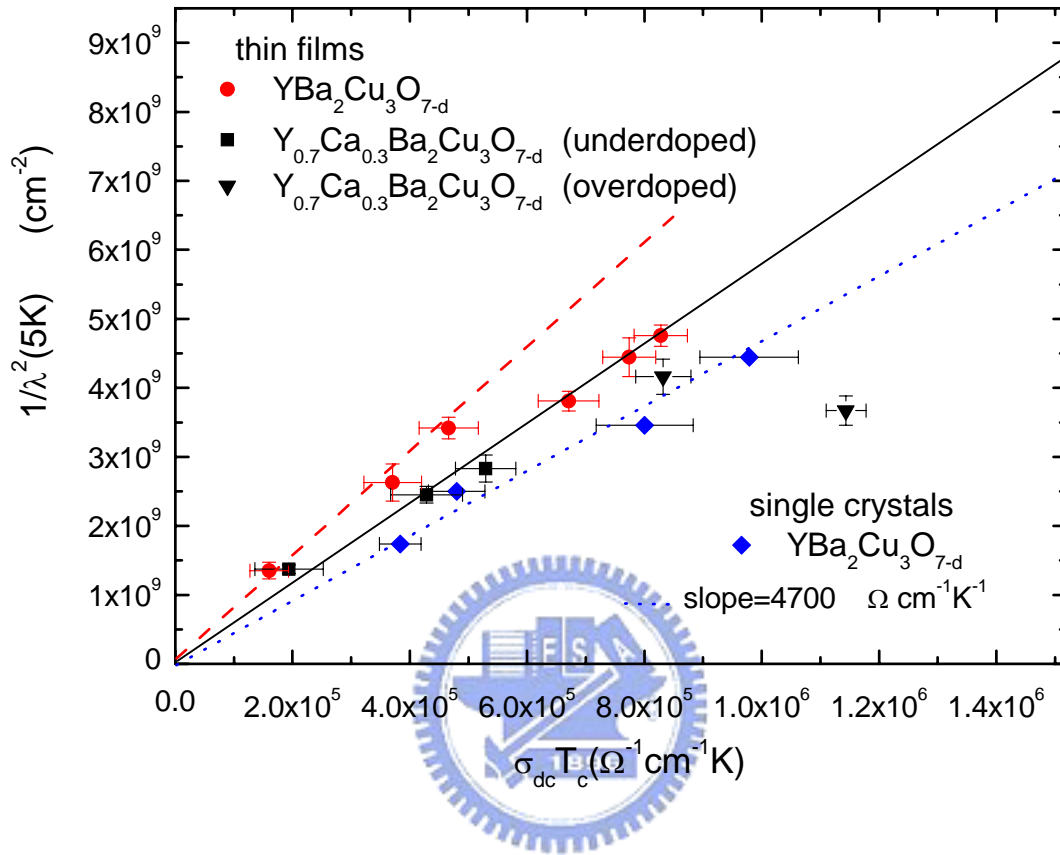
Fig. 4.20. Plot of superfluid density ($1/\lambda^2(5K)$) versus the product of the d.c. conductivity (σ_{dc}) and the superconducting transition temperature (T_c) for the YBCO and Ca-YBCO thin films with various oxygen contents. (σ_{dc} is measured just above the transition, and parallel to the CuO_2 (a-b) plane; data are shown on a linear scale) The values for σ_{dc} and $1/\lambda^2(5K)$ are obtained from standard four probe technique and microwave measurement, respectively. The $1/\lambda^2(5K)$ used in this scaling relation has been derived from the in-plane London penetration depth $\lambda(5K)$ measurement, where $1/\lambda^2(5K)$ is proportional to the number of carriers in the condensate. The dotted, solid and dashed lines are described by $\lambda^{-2} = 4700\sigma_{dc}T_c$, $\lambda^{-2} = 5700\sigma_{dc}T_c$ and $\lambda^{-2} = 7500\sigma_{dc}T_c$ respectively.
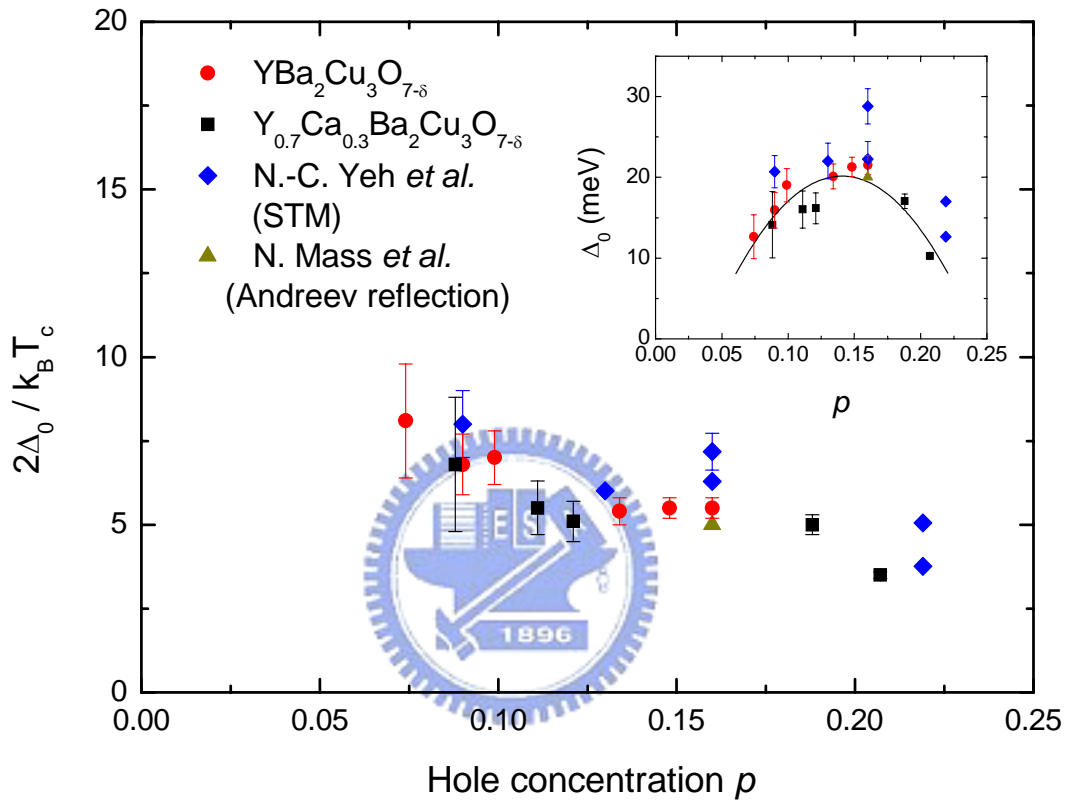
Fig. 4.21. The doping dependence of the normalized energy gap $2\Delta_0 / k_B T_c$ for the YBCO and Ca-YBCO thin films. The ratio $2\Delta_0 / k_B T_c$ appeared to be monotonic with the doping level p and it increased with decreasing doping. Inset: The doping dependence of the magnitude of energy gap Δ_0 for the YBCO and Ca-YBCO thin films.
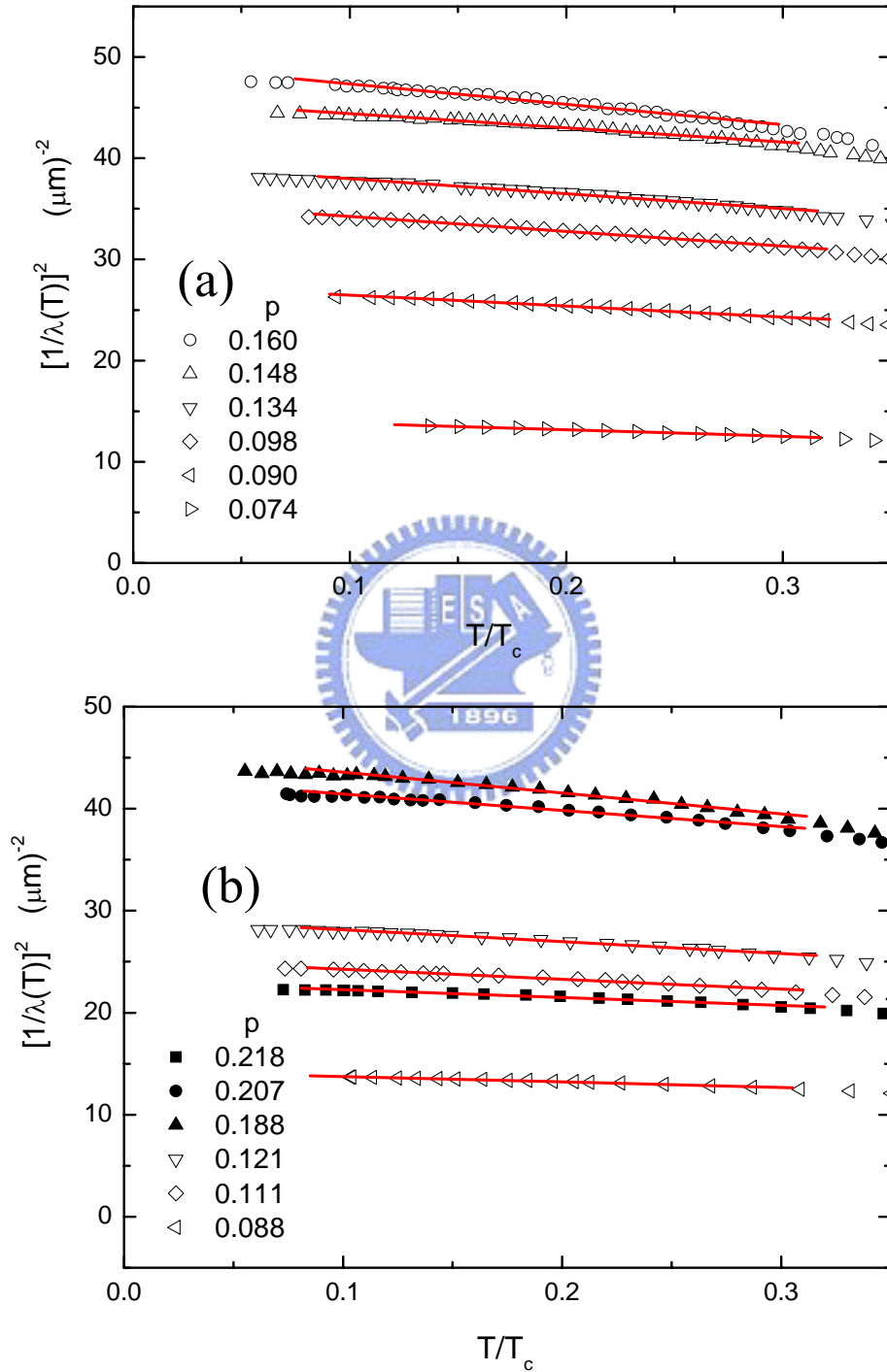
Fig. 4.22. The temperature dependence of $1/\lambda^2(T)$ with various hole concentrations for the (a) YBCO and (b) Ca-YBCO ring resonators at $T<0.35T_c$.

147
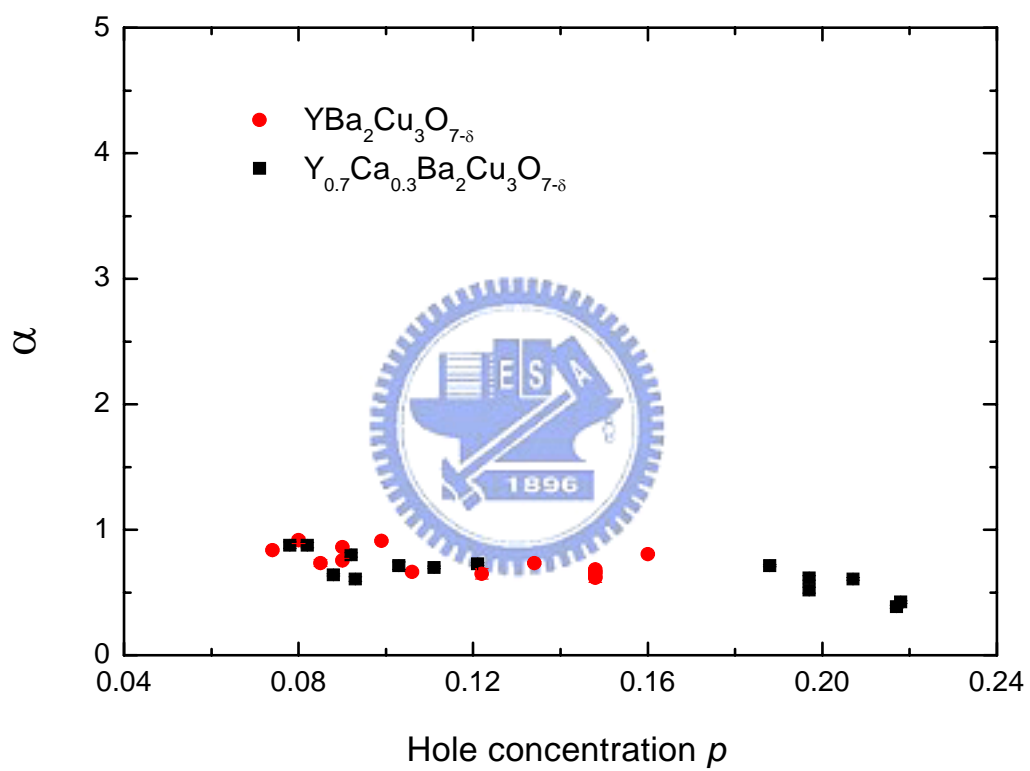
Fig. 4.23. The doping dependence of Fermi liquid correction factor α for the YBCO and Ca-YBCO films.
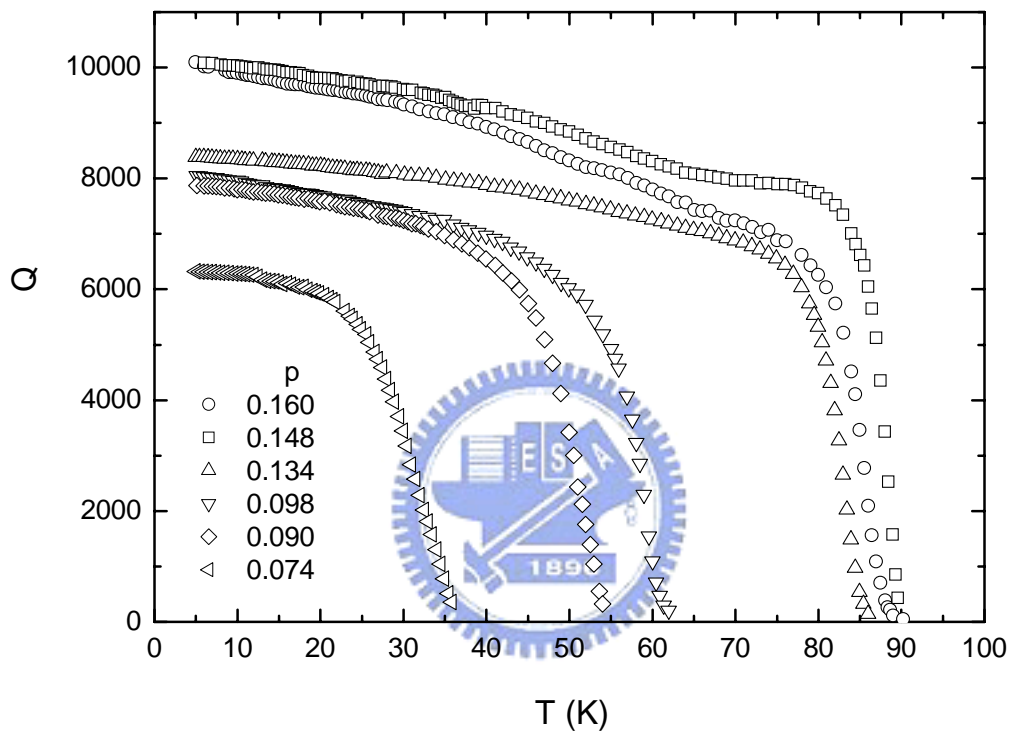
Fig. 4.24. The temperature dependence of the unloaded quality factor, Q, of the same YBCO ring resonator for p = 0.16, 0.148, 0.134, 0.098, 0.09, and 0.074, respectively.
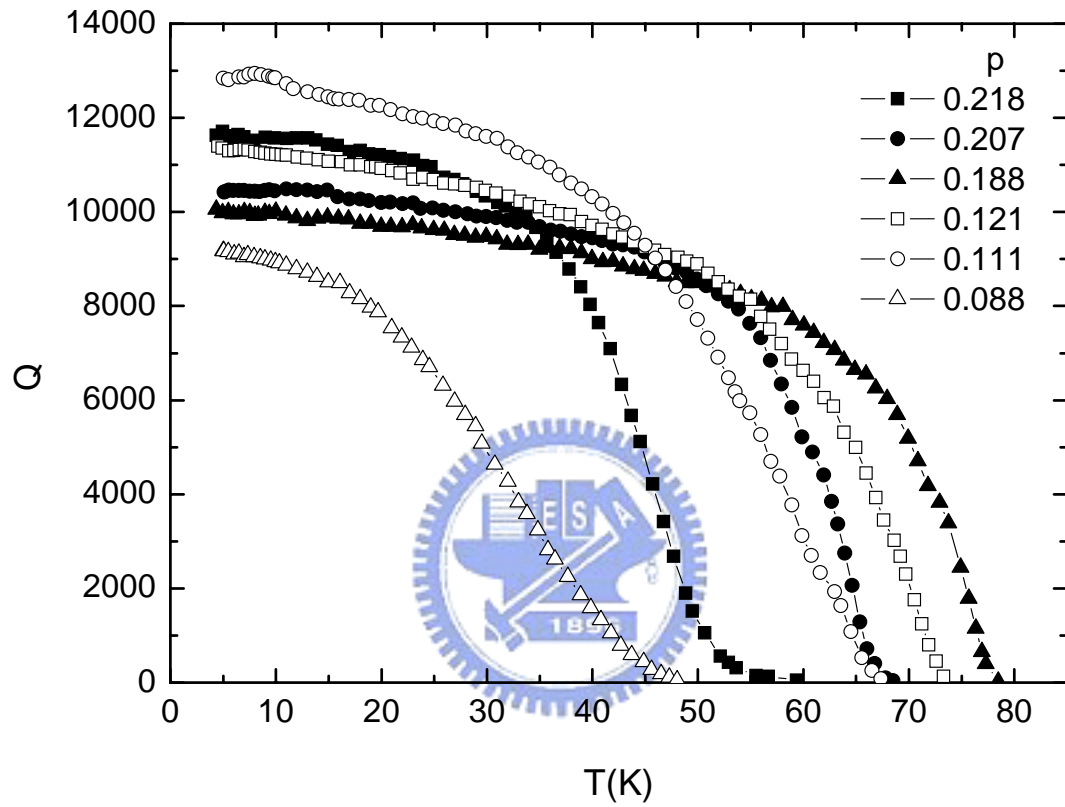
Fig. 4.25. The temperature dependence of the unloaded quality factor, Q, of the same Ca-YBCO ring resonator for p = 0.218, 0.207, 0.188, 0.121, 0.111, and 0.088, respectively.
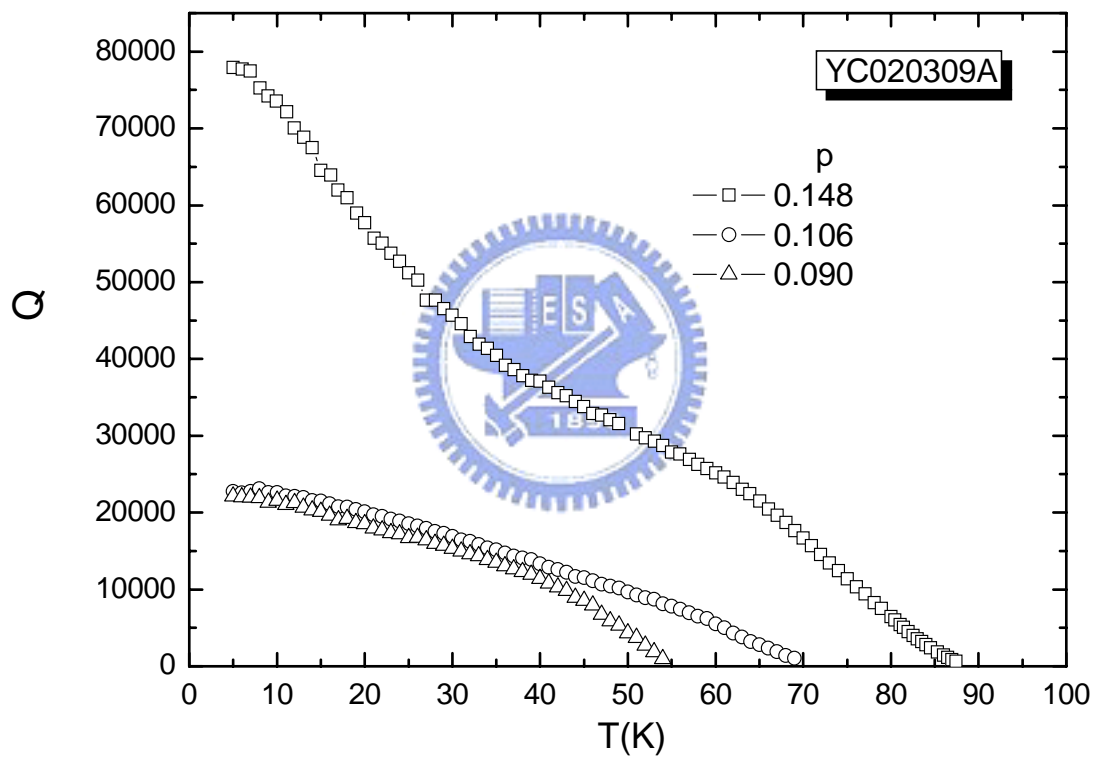
Fig. 4.26. The temperature dependence of the unloaded quality factor, Q, of the same YBCO microstrip line resonator for p = 0.148, 0.106, and 0.09, respectively.
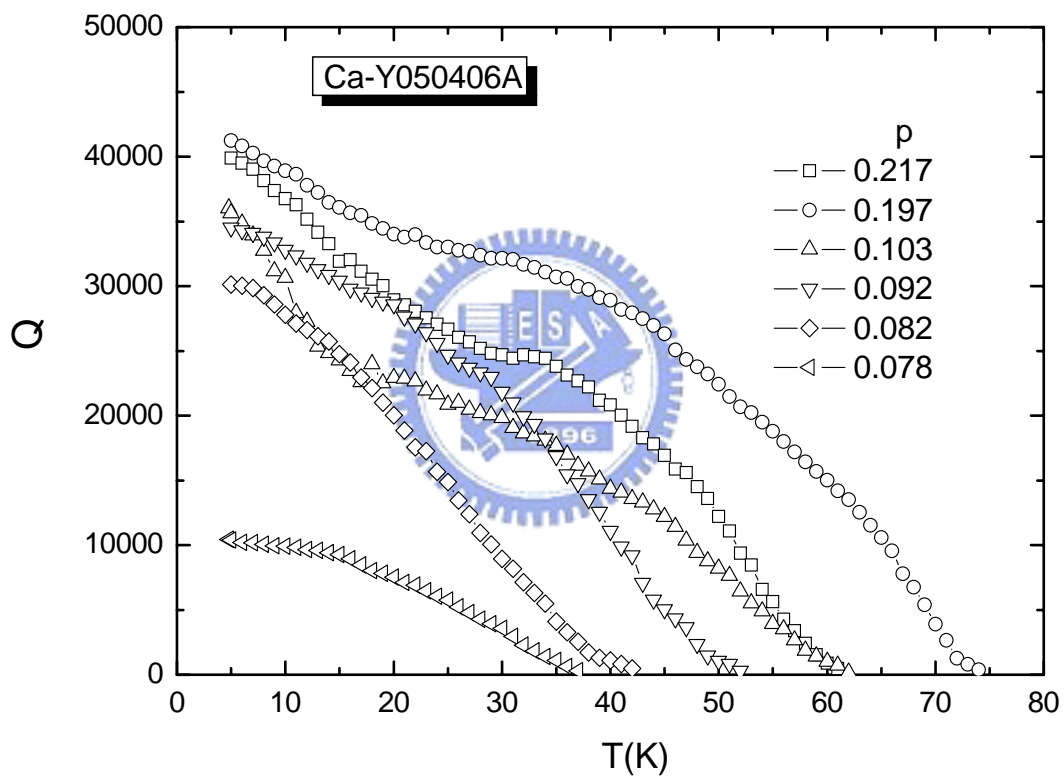
Fig. 4.27. The temperature dependence of the unloaded quality factor, Q, of the same Ca-YBCO microstrip line resonator for p = 0.217, 0.197, 0.103, 0.092, 0.082, and 0.078, respectively.
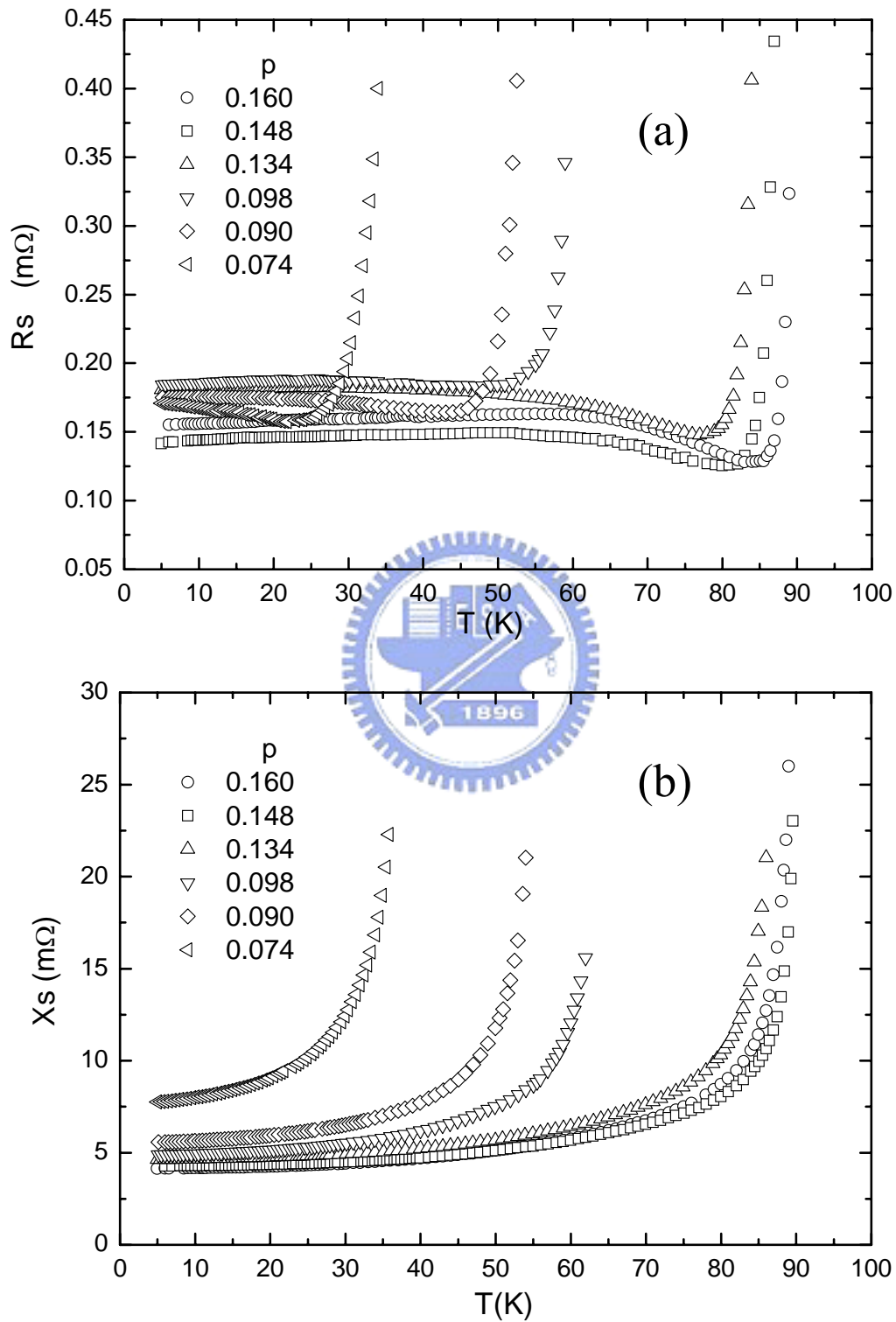
Fig. 4.28. The temperature dependence of (a) the Rs and (b) the Xs of the YBCO ring resonator with p = 0.16, 0.148, 0.134, 0.098, 0.09, and 0.074, respectively.
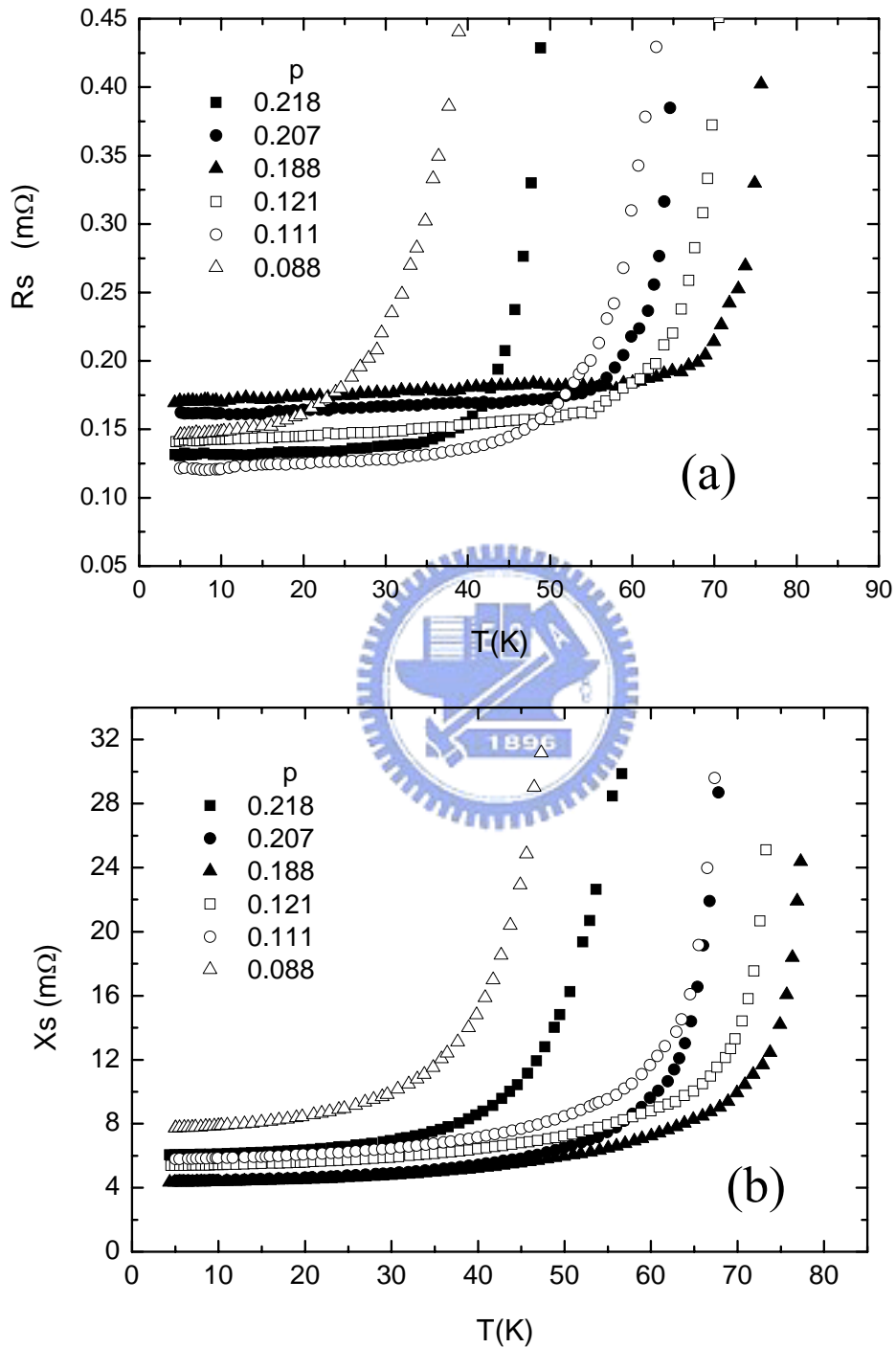
Fig. 4.29. The temperature dependence of (a) the Rs and (b) the Xs of the Ca-YBCO ring resonator with p = 0.218, 0.207, 0.188, 0.121, 0.111, and 0.088, respectively.
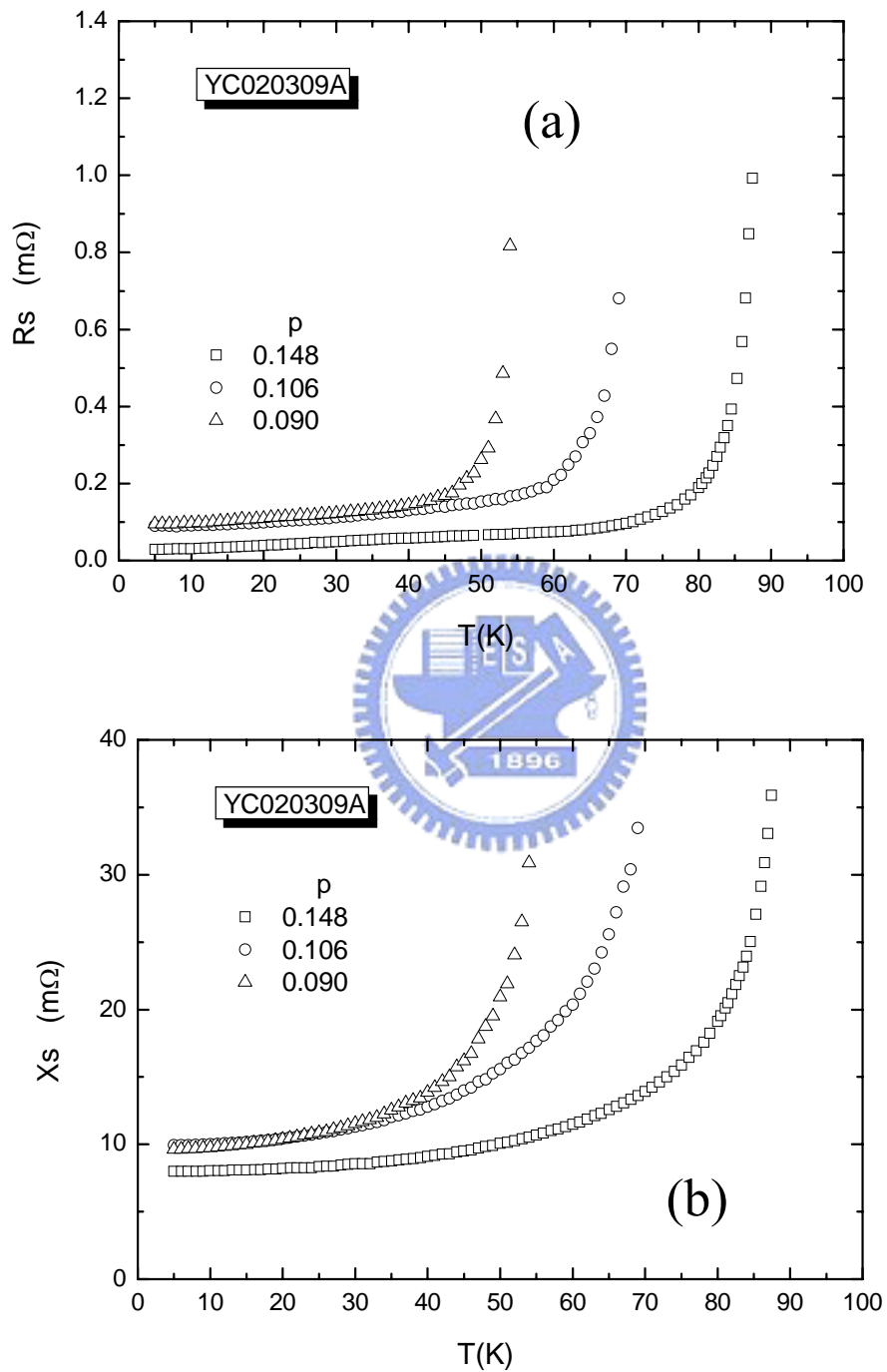
Fig. 4.30. The temperature dependence of (a) the Rs and (b) the Xs of the YBCO microstrip line resonator with p = 0.148, 0.106, and 0.09, respectively.

155
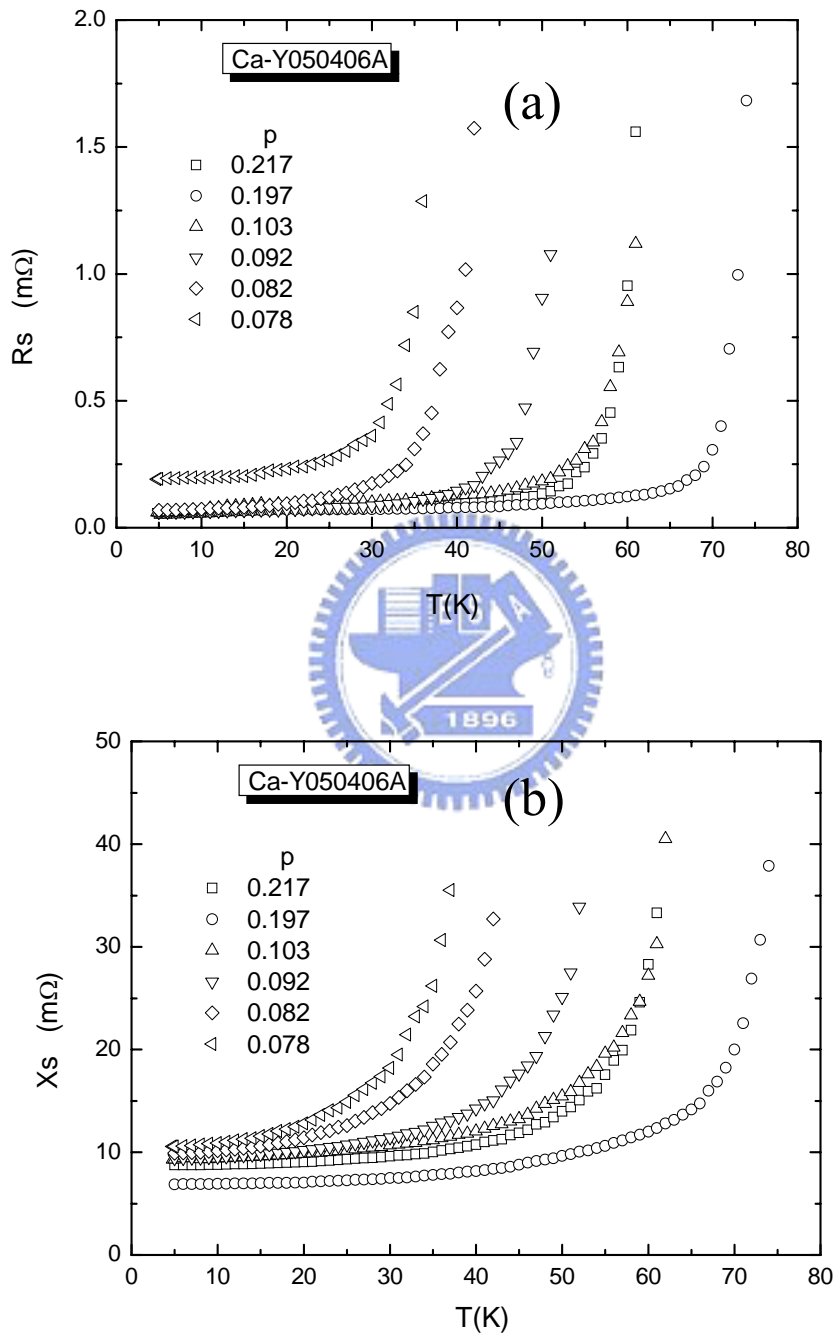
Fig. 4.31. The temperature dependence of (a) the Rs and (b) the Xs of the Ca-YBCO microstrip line resonator with p = 0.217, 0.197, 0.103, 0.092, 0.082, and 0.078, respectively.
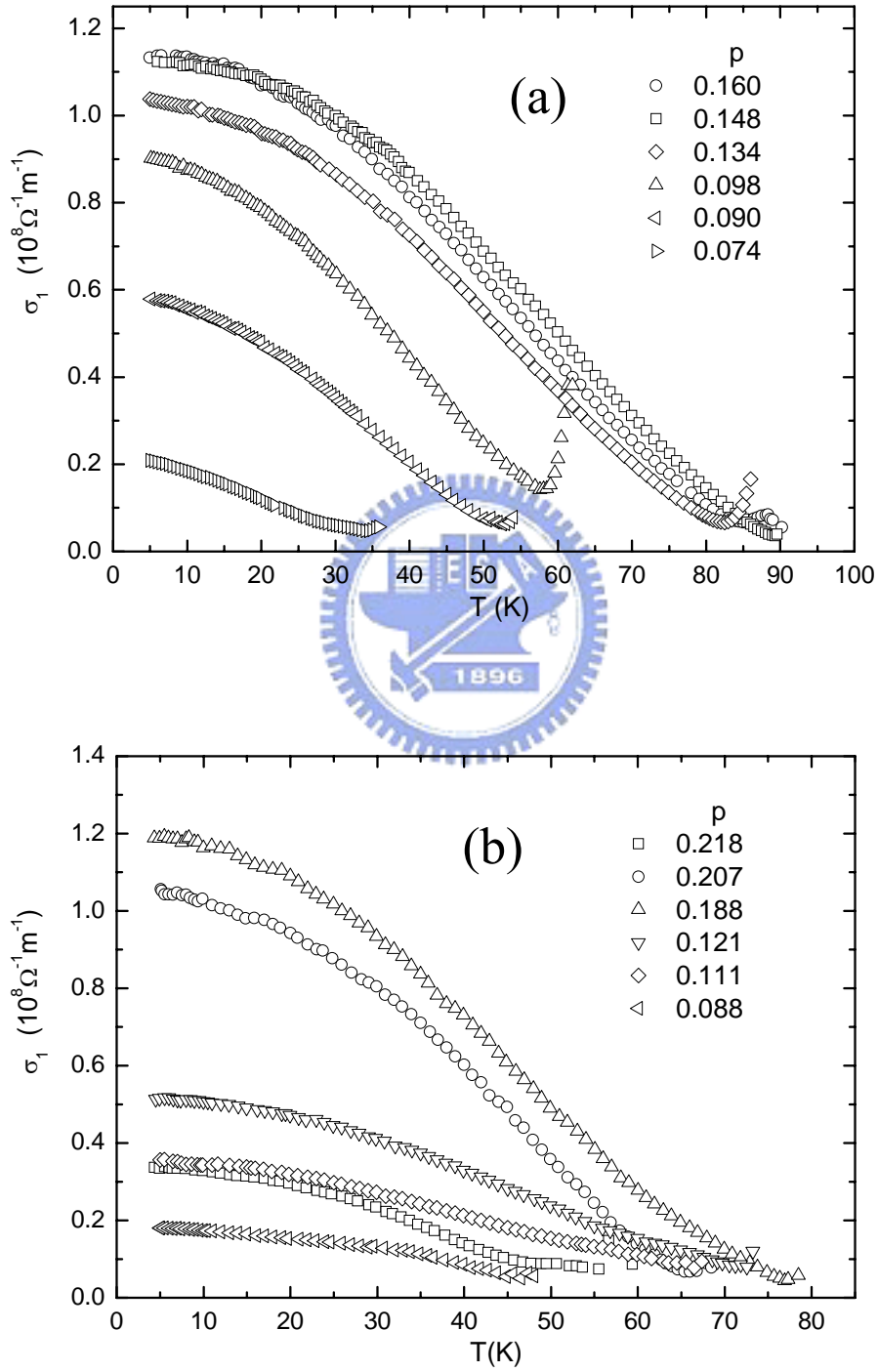
Fig. 4.32. The temperature dependence of the real-part conductivity, σ_1, of the (a) YBCO and (b) Ca-YBCO ring resonators with various hole concentrations.
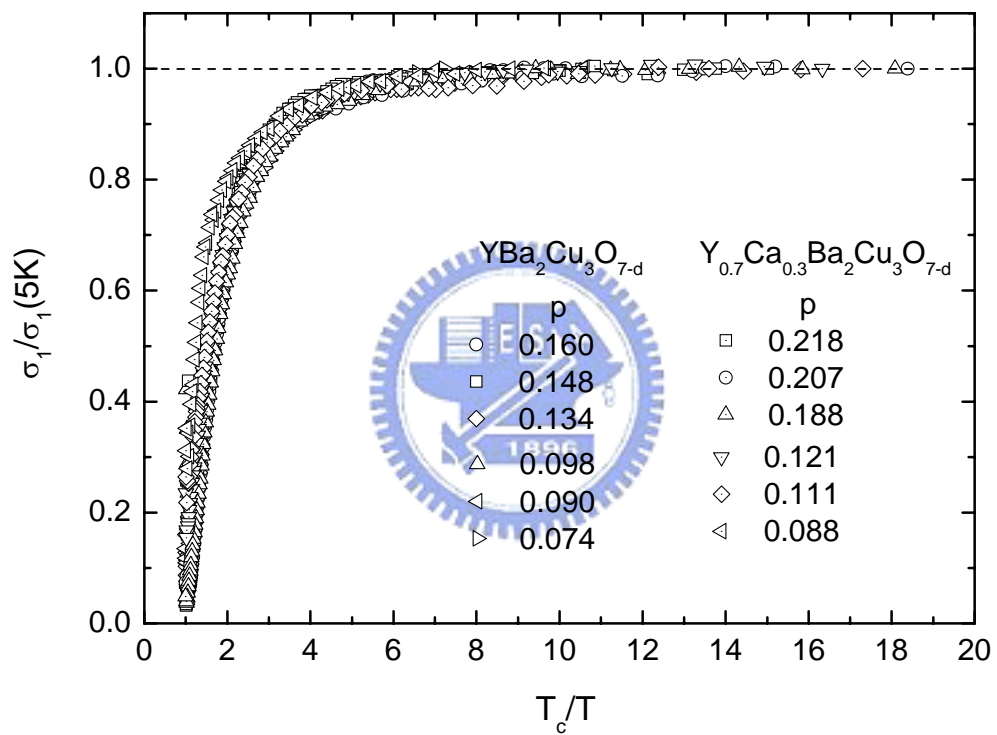
Fig. 4.33. The normalized conductivity $\sigma_1/\sigma_1(5K)$ versus T_c/T for the YBCO and Ca-YBCO ring resonators with various hole concentrations.
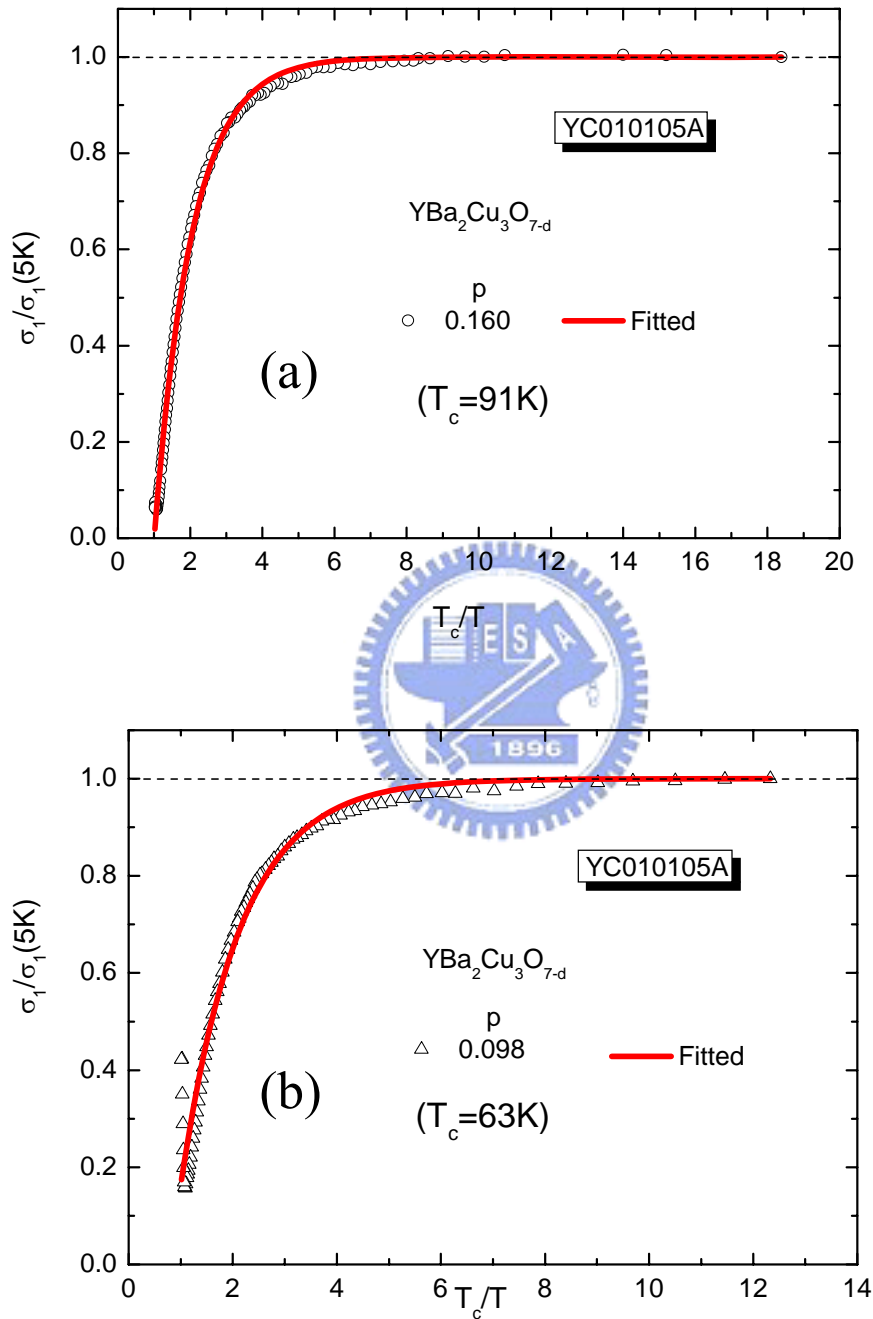
Fig. 4.34. (a) The normalized conductivity $\sigma_1/\sigma_1(5K)$ versus T_c/T for the YBCO ring resonator with p=0.16. The solid line is the formula, $\sigma_1/\sigma_1(5K) = (1 - Ae^{-c_1 \cdot T_c/T})$, fitted to the experimental data. (b) The normalized conductivity $\sigma_1/\sigma_1(5K)$ versus T_c/T for the YBCO ring resonator with p=0.098. The solid line is the formula, $\sigma_1/\sigma_1(5K) = (1 - Ae^{-c_1 \cdot T_c/T})$, fitted to the experimental data.
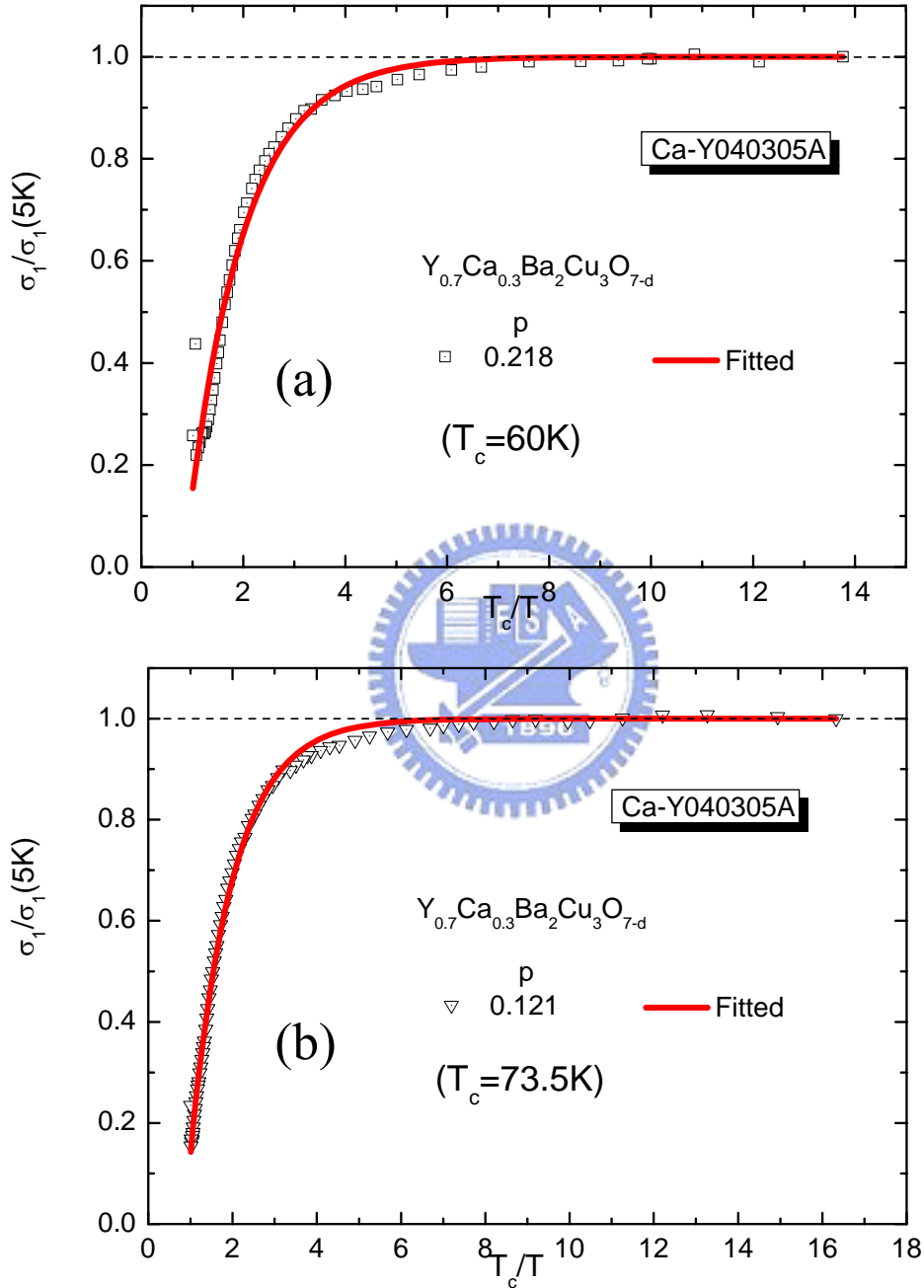
Fig. 4.35. (a) The normalized conductivity $\sigma_1/\sigma_1(5K)$ versus T_c/T for the Ca-YBCO ring resonator with $p=0.218$. The solid line is the formula, $\sigma_1/\sigma_1(5K) = (1 - Ae^{-c_1 \cdot T_c/T})$, fitted to the experimental data. (b) The normalized conductivity $\sigma_1/\sigma_1(5K)$ versus T_c/T for the Ca-YBCO ring resonator with $p=0.121$. The solid line is the formula, $\sigma_1/\sigma_1(5K) = (1 - Ae^{-c_1 \cdot T_c/T})$, fitted to the experimental data.
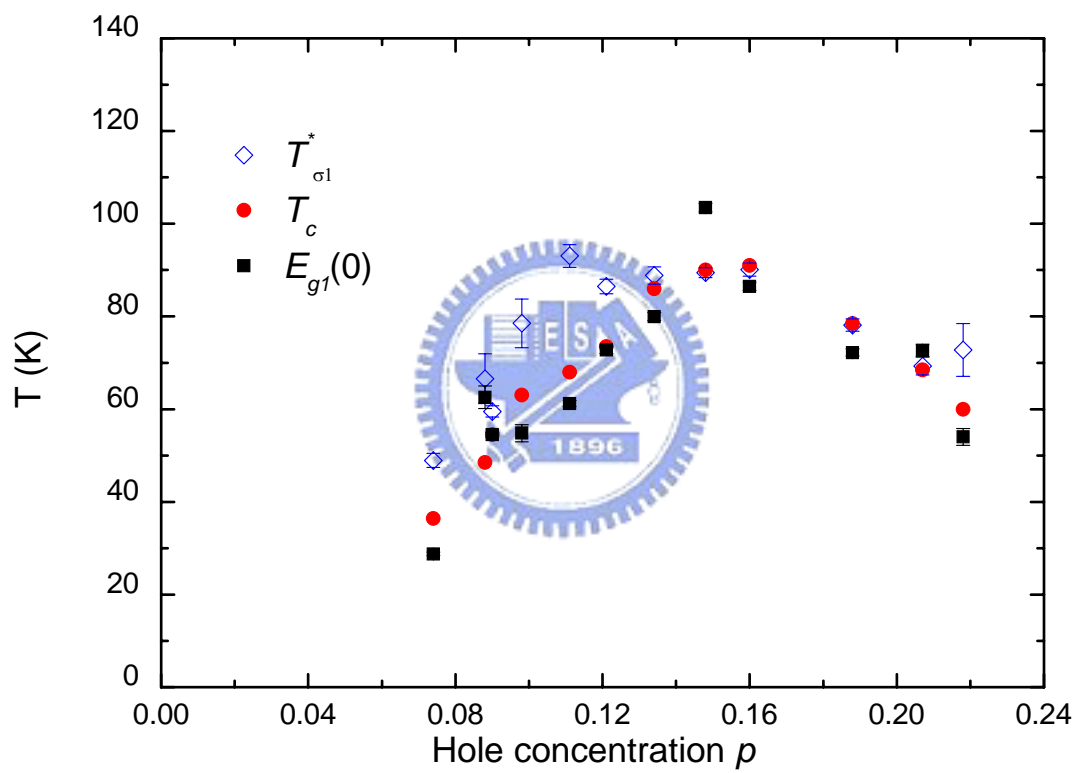
Fig. 4.36. The doping dependence of the characteristic energy scale, $T^*_{\sigma 1}$, $E_{g1}(0)$ and T_c was obtained from the numerical fitting of $\sigma_1/\sigma_1(5K)$ for the YBCO and Ca-YBCO ring resonators.
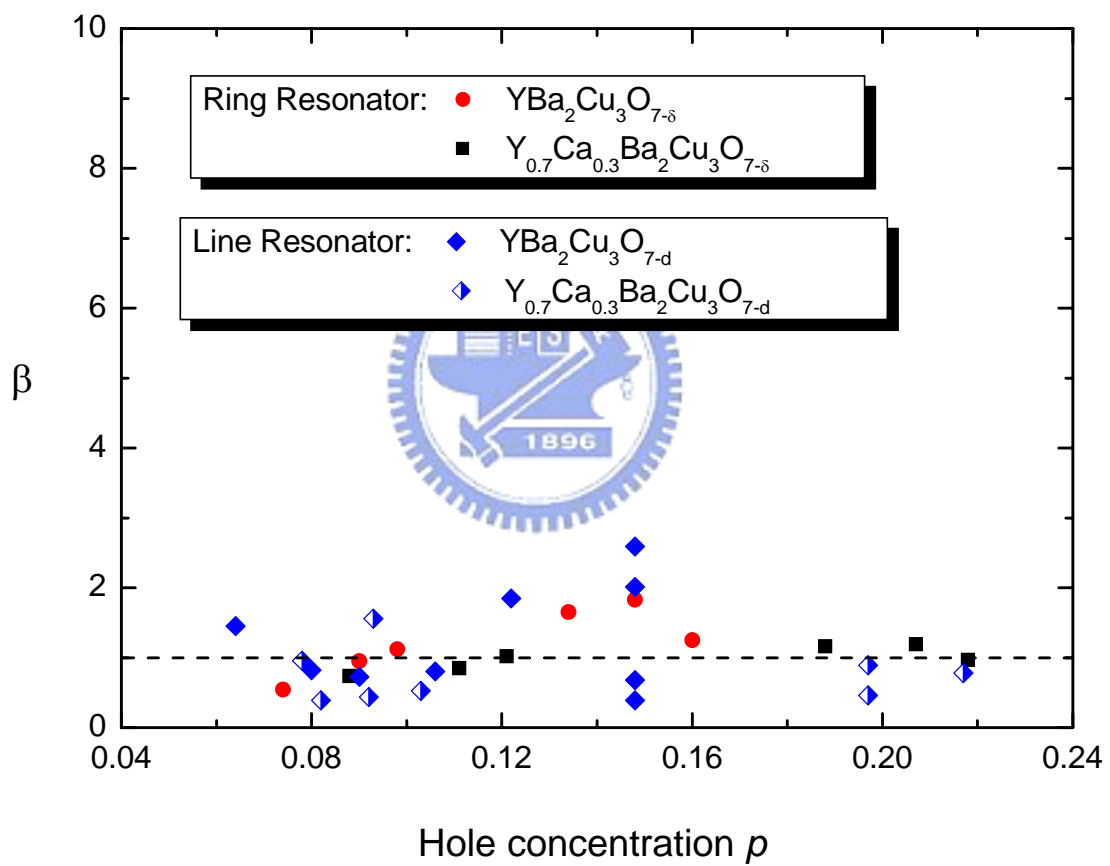
Fig. 4.37. The doping dependence of the vertex correction factor β. The dashed line is the average value of the experimental data and is 1.0 with the error bar of 0.5.
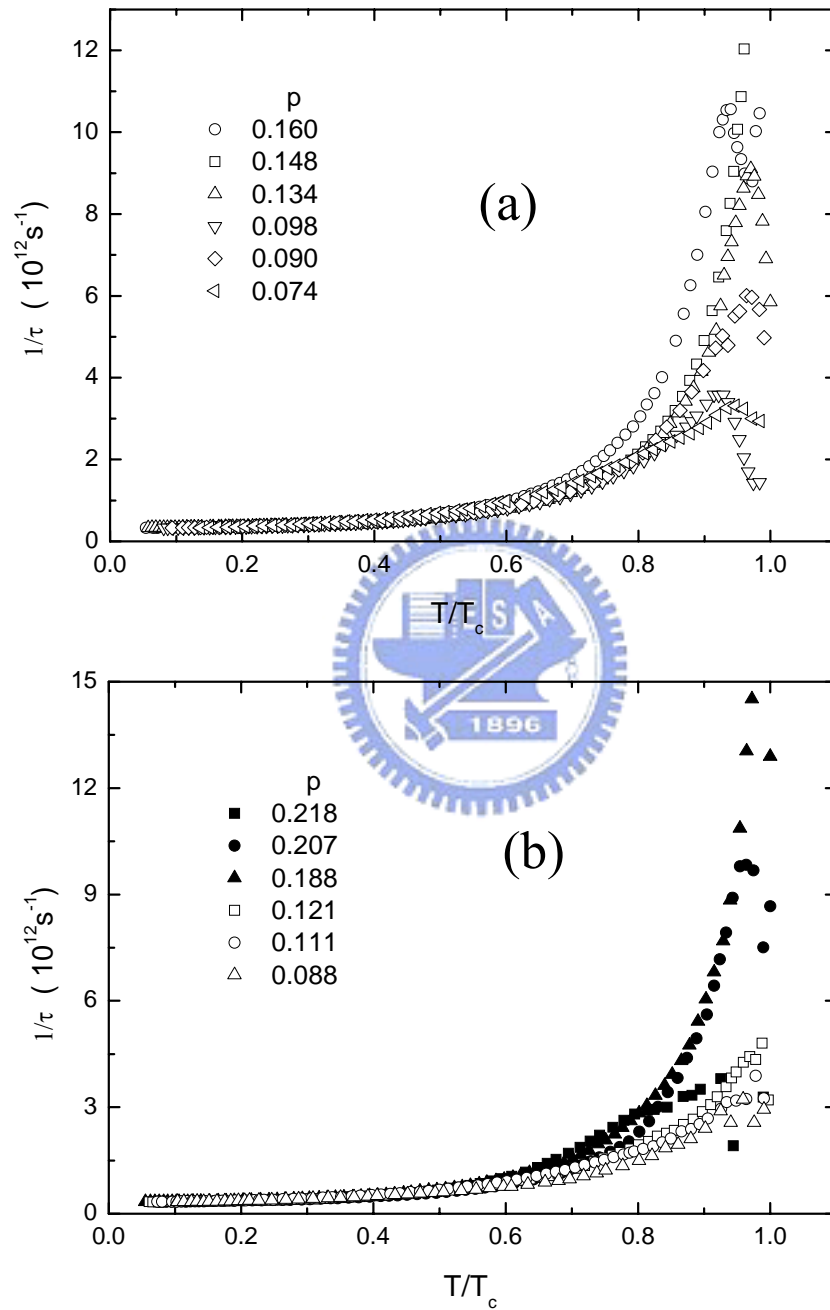
Fig. 4.38. The normalized temperature dependence of the scattering rate, $1/\tau$, of the (a) YBCO and (b) Ca-YBCO ring resonators with various hole concentrations. Obviously, the scattering rate approaches to a constant value at $T<0.4T_c$.
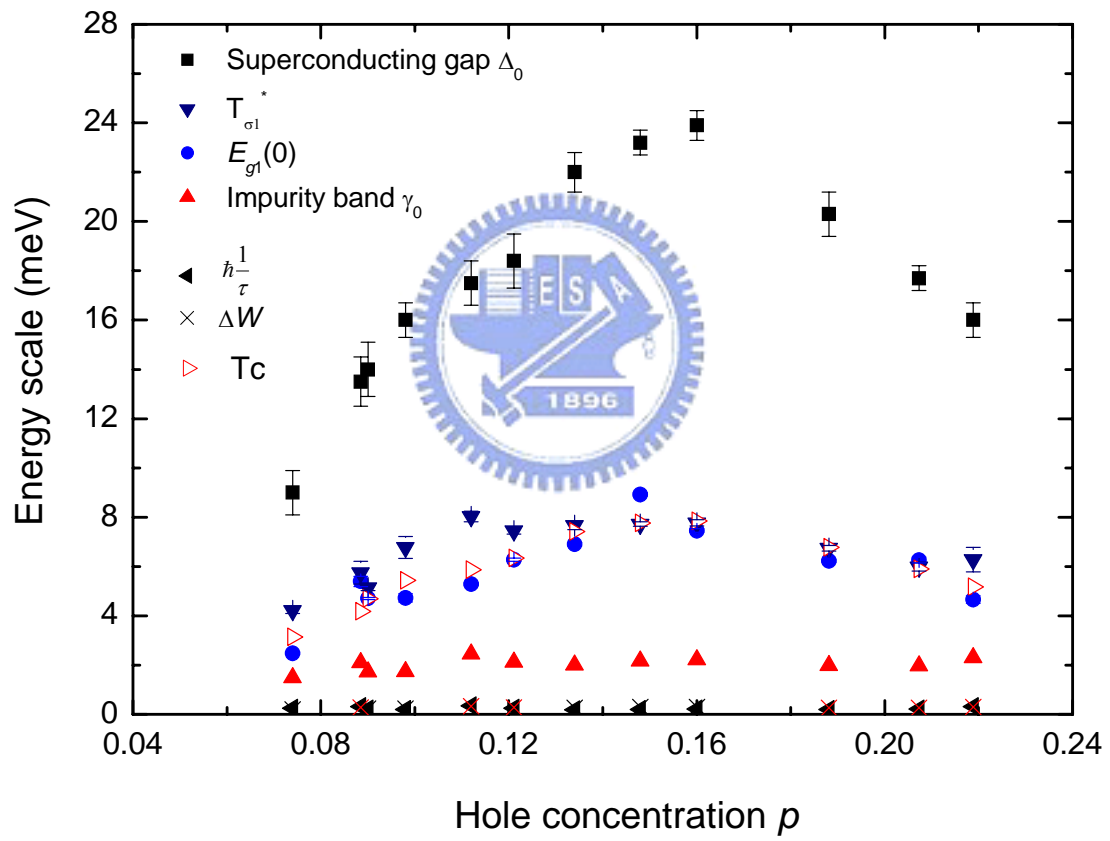
Fig. 4.39. The doping dependence of the energy scale Δ_0, $T_{\sigma 1}^*$, $E_{g1}(0)$, γ_0, $\hbar\dfrac{1}{\tau}$, ΔW, and T_c for the YBCO and Ca-YBCO thin films.
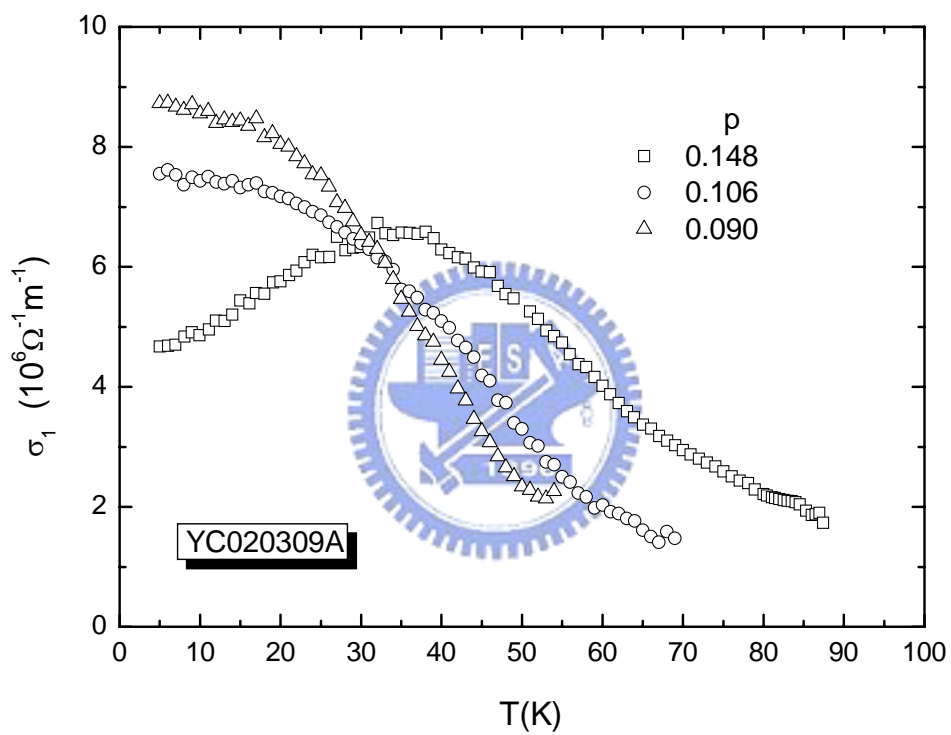
Fig. 4.40. The temperature dependence of the real-part conductivity, σ_1, of the YBCO microstrip line resonator with p = 0.148, 0.106 and 0.09, respectively.
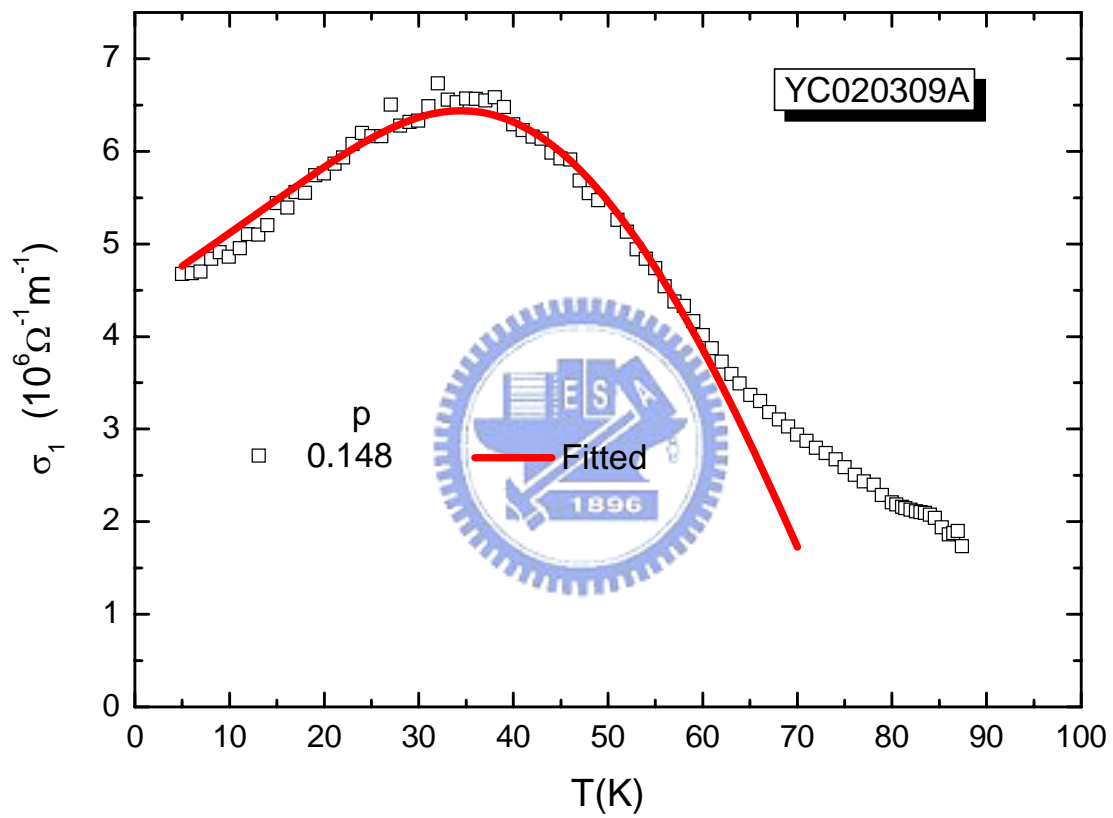
Fig. 4.41. The temperature dependence of the real-part conductivity, σ_1, of the YBCO microstrip line resonator with $p = 0.148$. The broad peak was observed at T≈35K. The solid line is the fitting result of σ_1 at T< 60K with the formula, $\sigma_1 = \sigma_1(5K)[(1 - Ae^{-c_1 \cdot T_c / T}) + a'\frac{T}{T_c}]$.
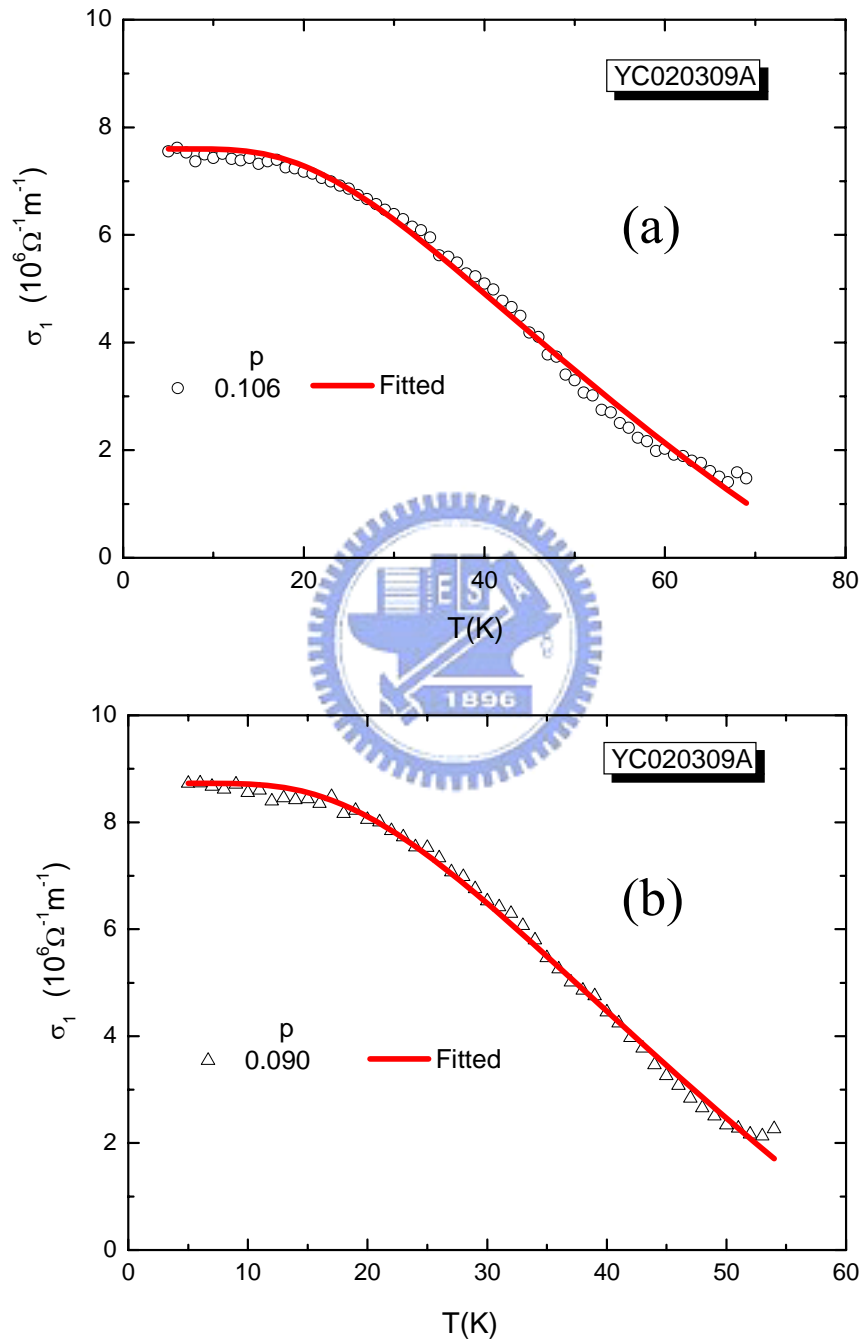
Fig. 4.42. The temperature dependence of the real-part conductivity, σ_1, of the YBCO microstrip line resonator with (a) $p = 0.106$ and (b) $p = 0.09$. The solid line is the fitting result of σ_1 with the formula, $\sigma_1 = \sigma_1(5K)(1 - Ae^{-c_1 \cdot T_c / T})$.
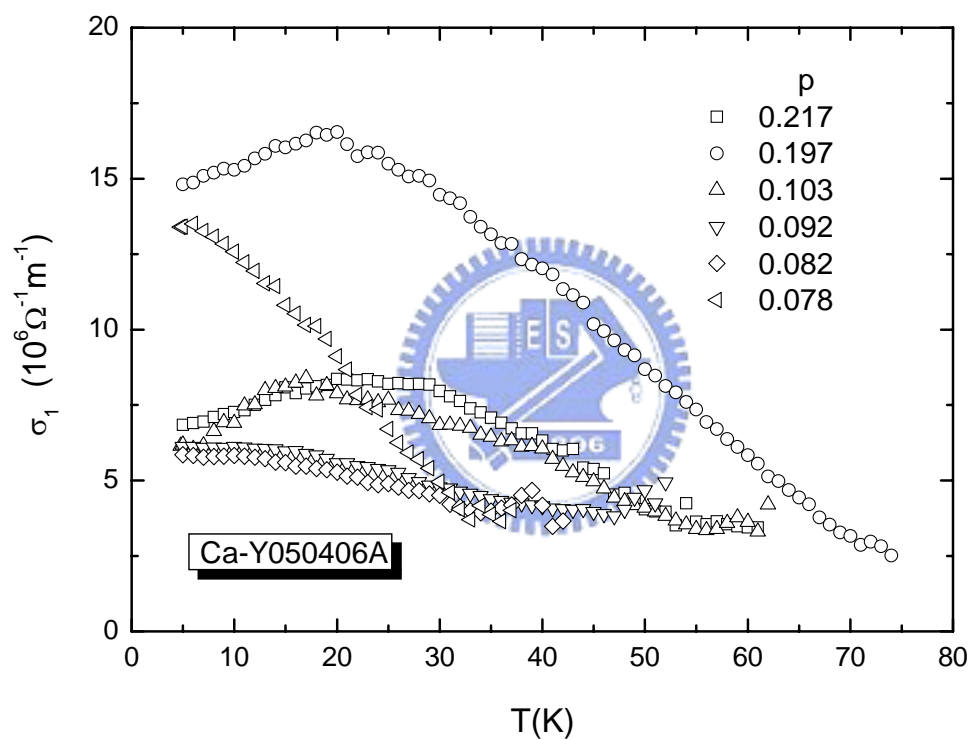
Fig. 4.43. The temperature dependence of the real-part conductivity, σ_1, of the Ca-YBCO microstrip line resonator with p = 0.217, 0.197, 0.103, 0.092, 0.082 and 0.078, respectively.
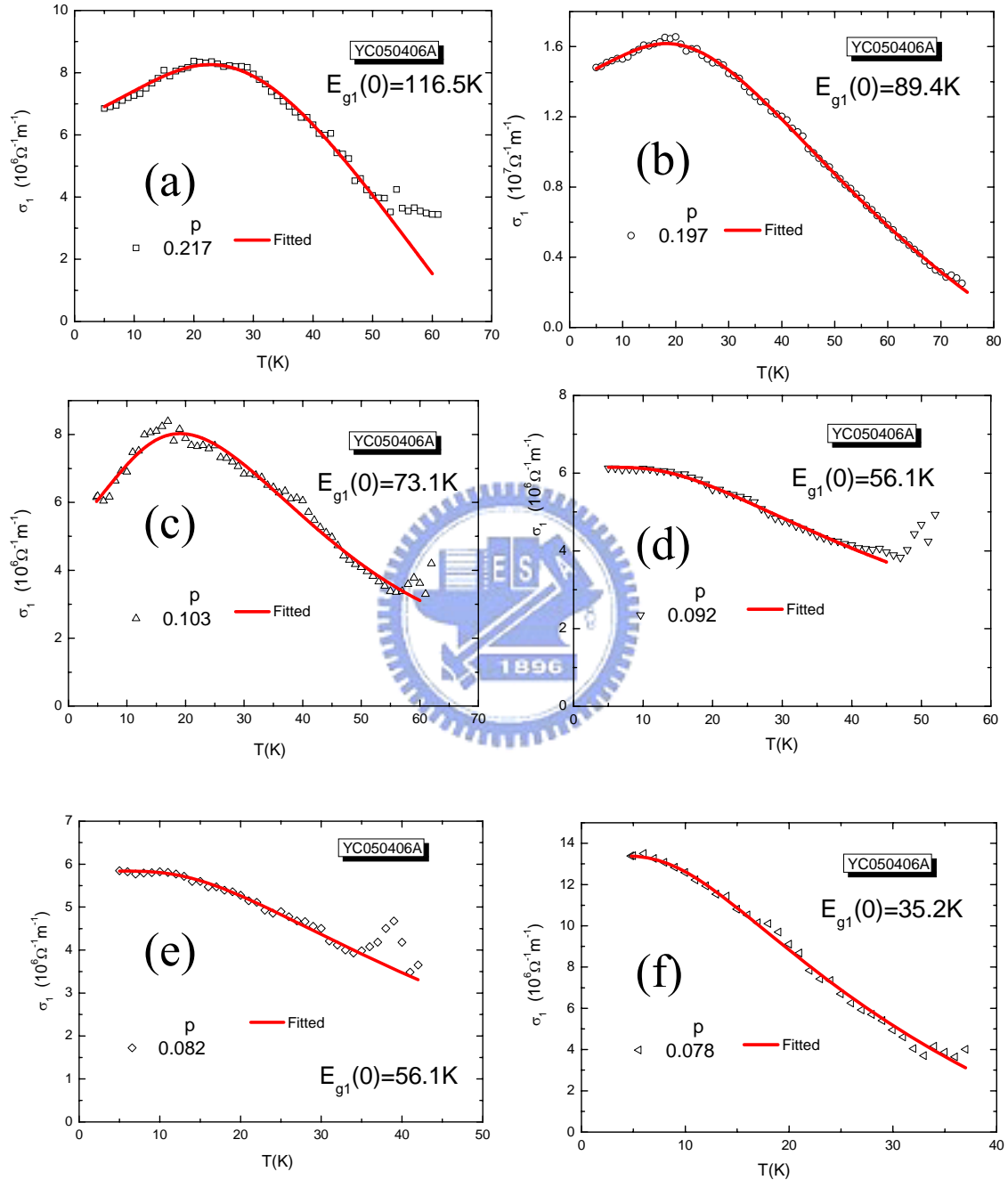
Fig. 4.44. The temperature dependence of the real-part conductivity, σ_1, of the Ca-YBCO microstrip line resonator with p = 0.217, 0.197, 0.103, 0.092, 0.082 and 0.078, respectively. (a)-(c) The solid line is the fitting result of σ_1 with the formula, $\sigma_1 = \sigma_1(5K)[(1 - Ae^{-c_1 \cdot T_c / T}) + a'\dfrac{T}{T_c}]$. (d)-(f) The solid line is the fitting result of σ_1 with the formula, $\sigma_1 = \sigma_1(5K)(1 - Ae^{-c_1 \cdot T_c / T})$.
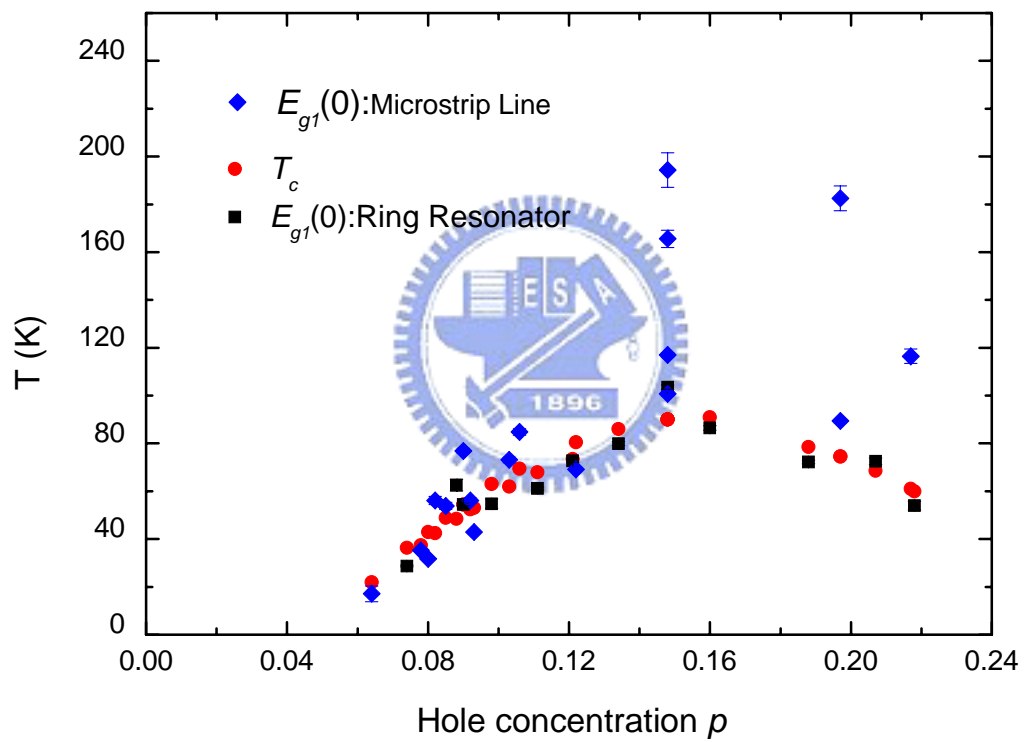
Fig. 4.45. The doping dependence of the thermal activation gap, $E_{g1}(0)$, of the YBCO and Ca-YBCO thin films extracted from the microwave conductivity, $\sigma_1(T)$, measurements.
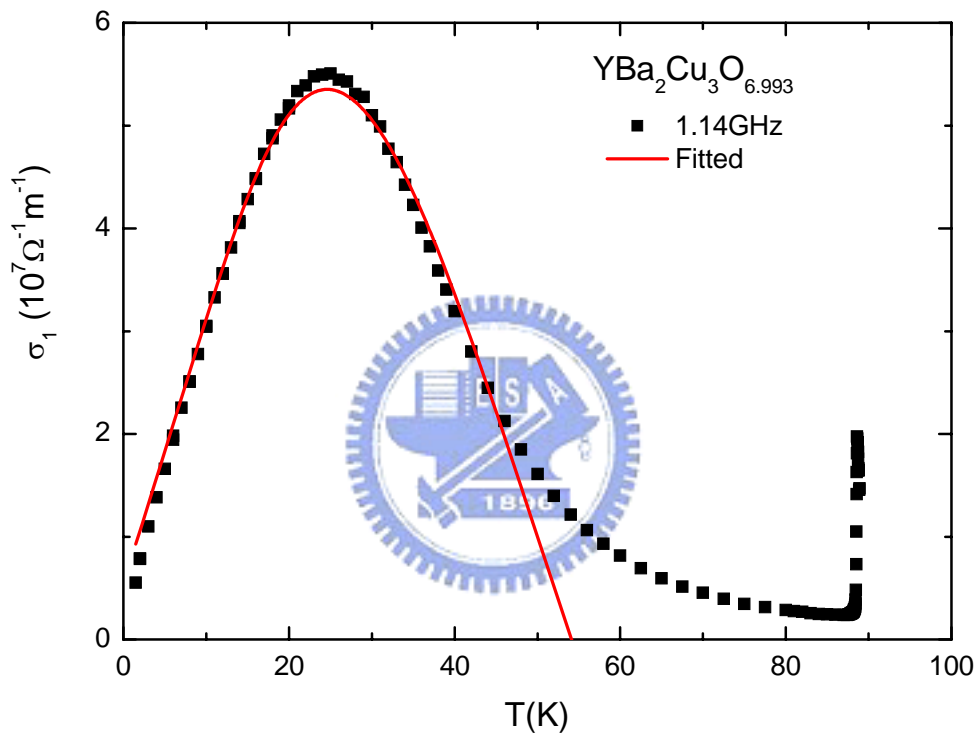
Fig. 4.46. The temperature dependence of the microwave real part conductivity, σ_1, of YBCO single crystal extracted from the $R_s(T)$ and $X_s(T)$ measurements [76]. The solid line is the fitting result of σ_1 with the formula,

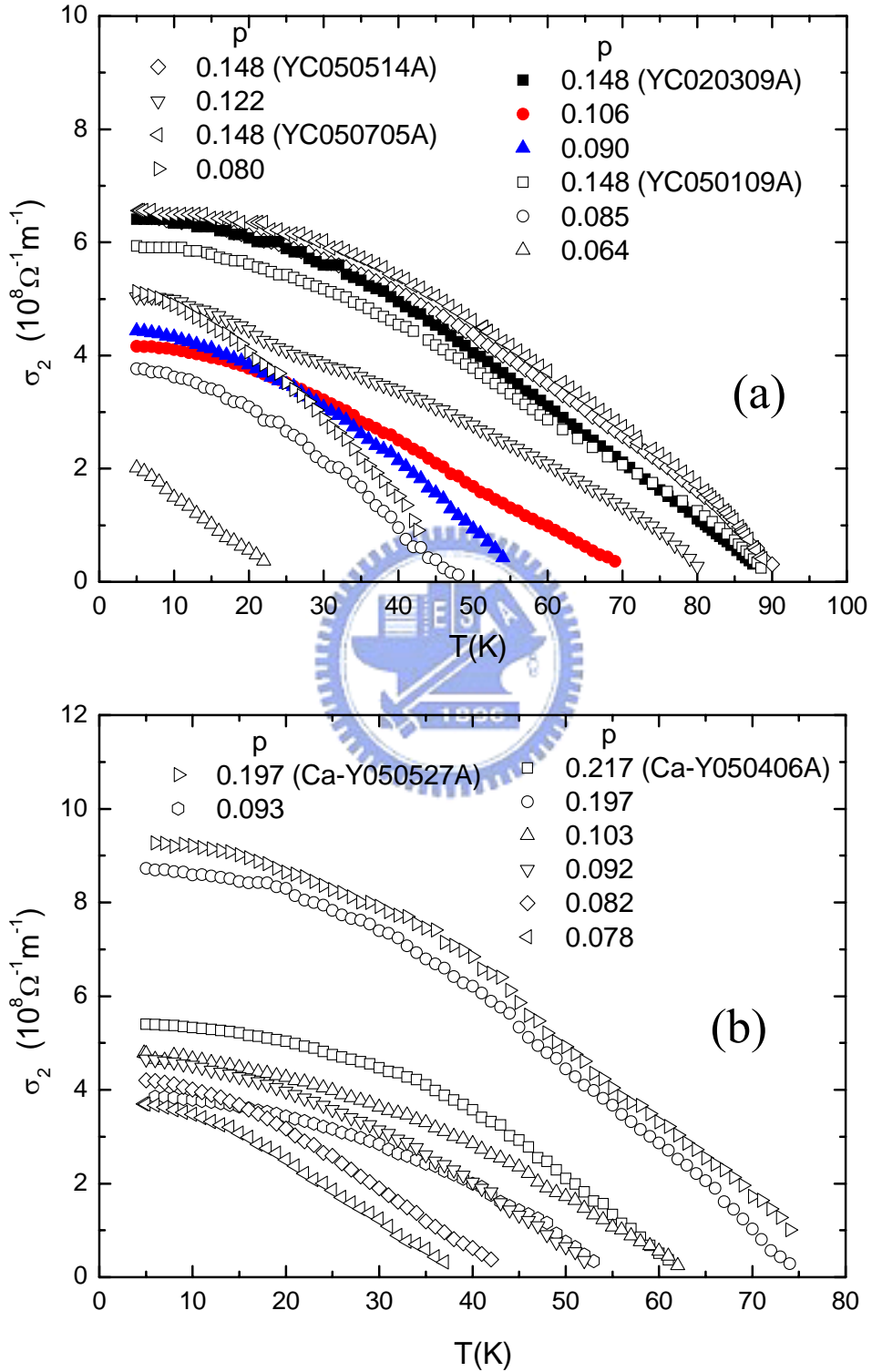$$\sigma_1 = \sigma_1(5K)[(1 - Ae^{-c_1 \cdot T_c / T}) + a'\frac{T}{T_c}] \text{ at T<50 K.}$$
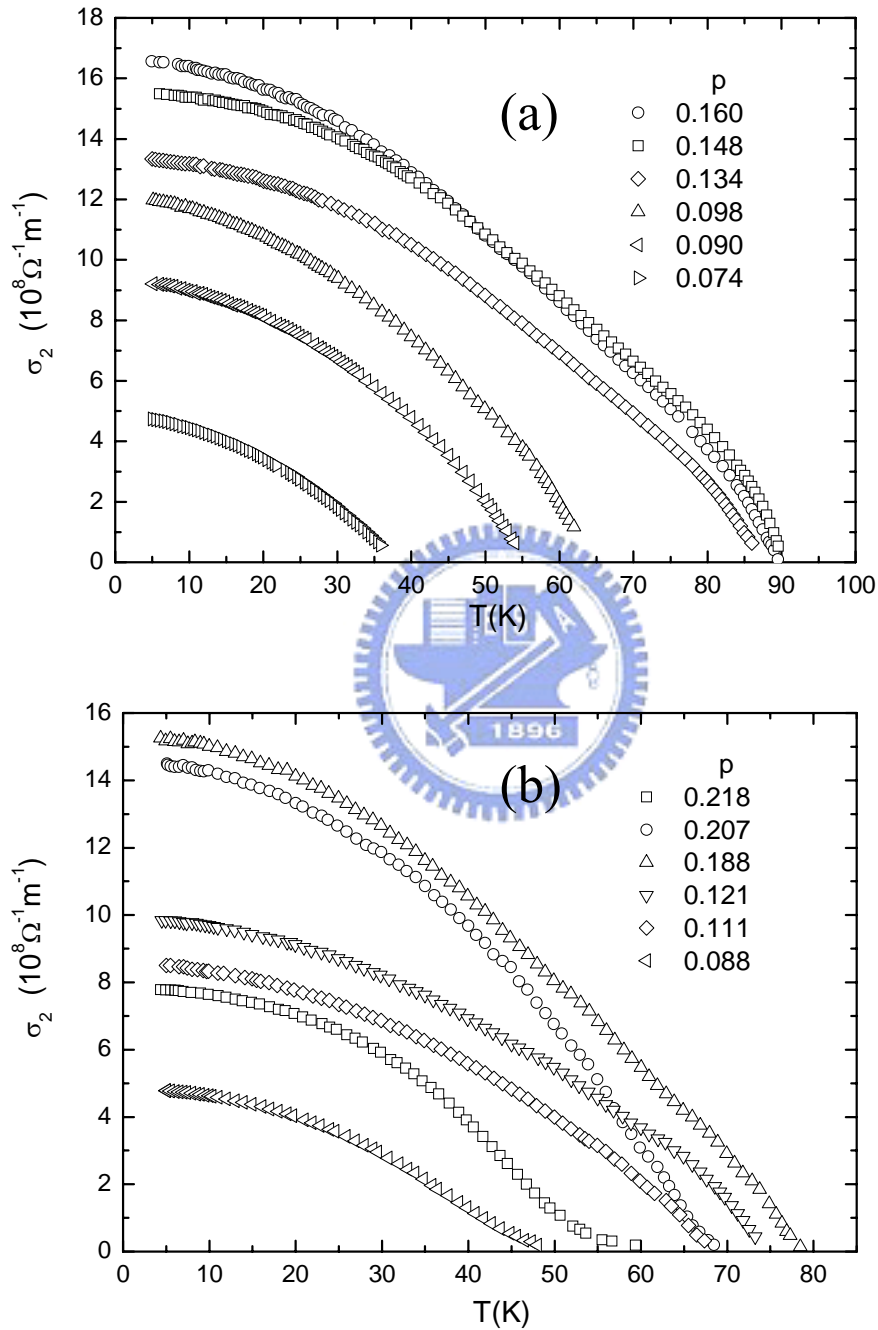
Fig. 4.47. The temperature dependence of the imaginary part of the microwave conductivity, σ_2, for (a) the YBCO and (b) the Ca-YBCO ring resonators with various hole concentrations. The values of σ_2 increases as decreasing T at $T < T_c$ for all doping levels.
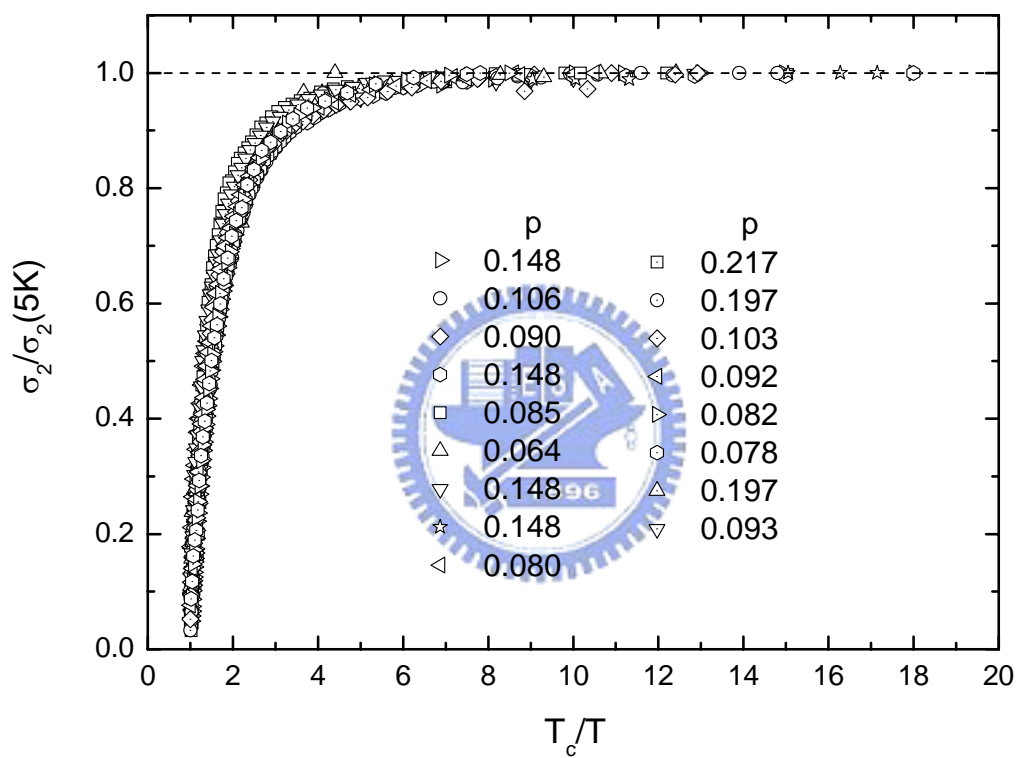
172
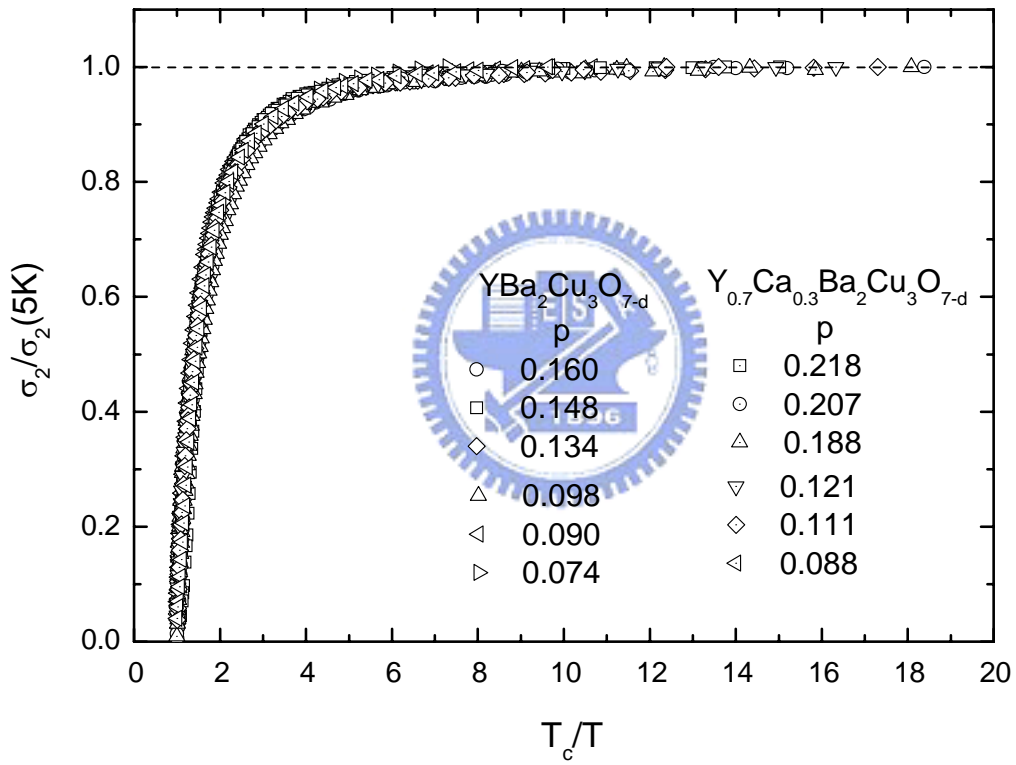
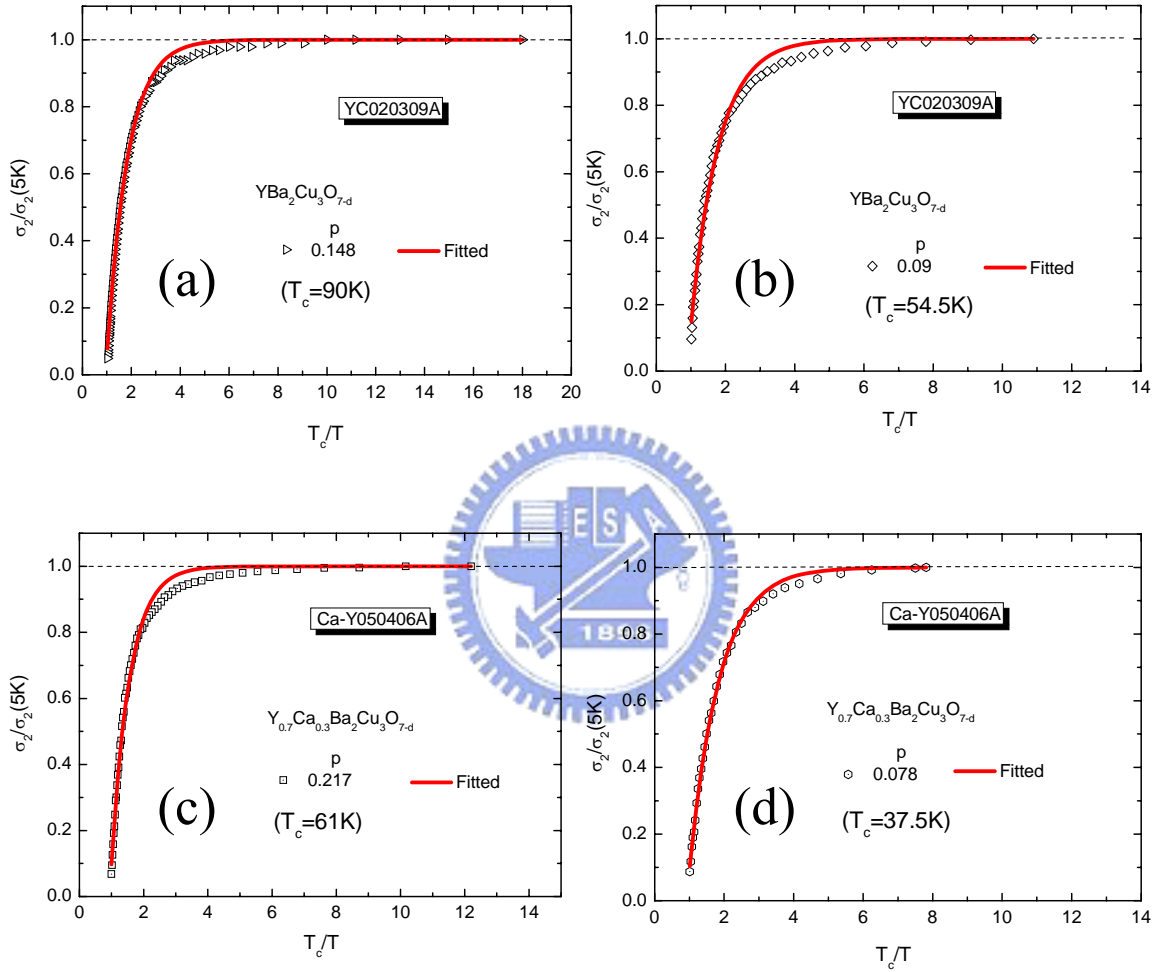Fig. 4.48. Plot of σ_2/σ_2(5K) versus T_c/T for the YBCO and Ca-YBCO ring resonators with various hole concentrations.
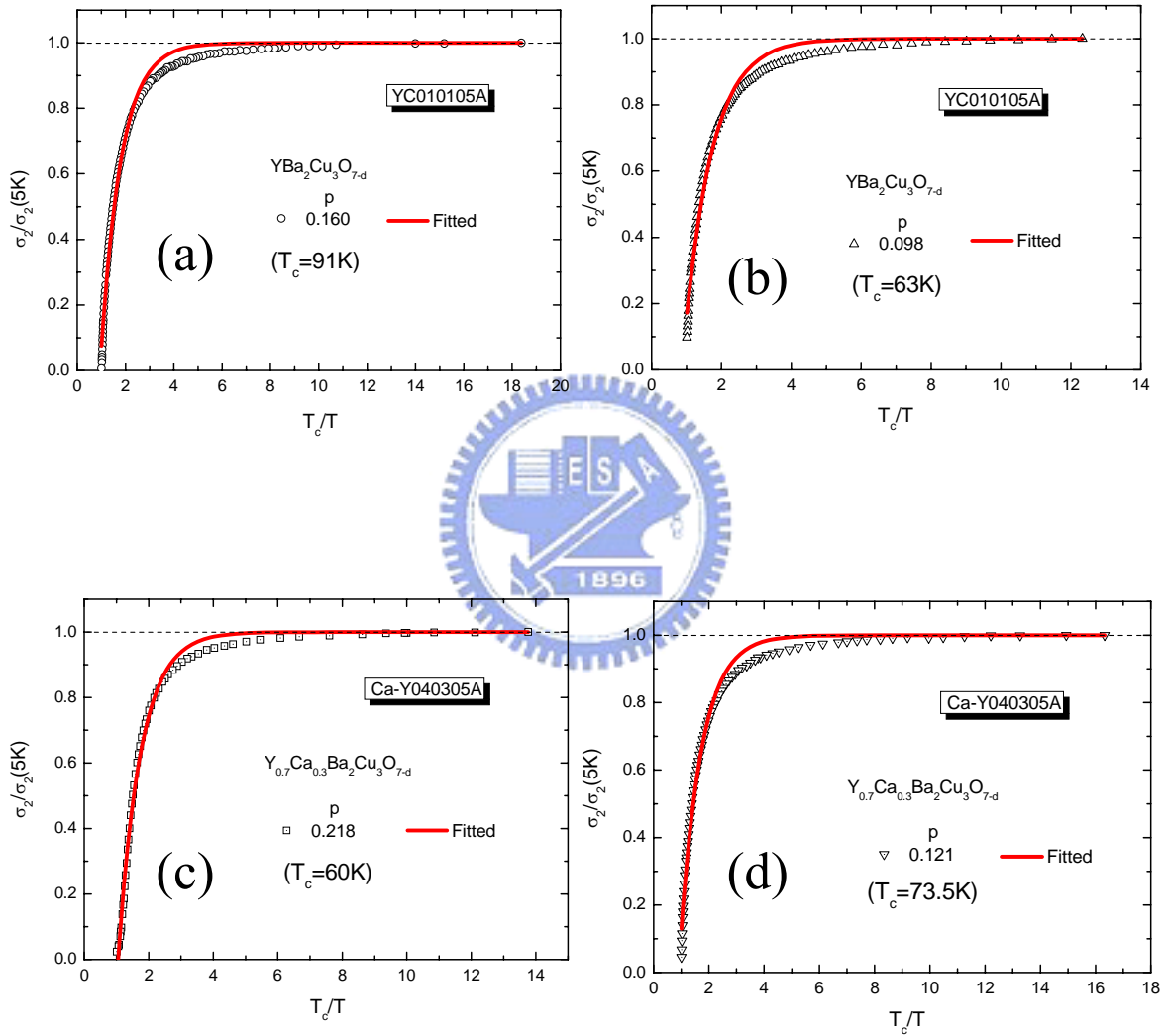
Fig. 4.49. (a)-(b) Plot of $\sigma_2/\sigma_2(5K)$ versus T_c/T for the YBCO ring resonator with (a) $p=0.16$ and (b) $p=0.098$, respectively. The solid line is the fitting result with the formula, $\sigma_2/\sigma_2(5K) = (1 - Be^{-c_2 \cdot T_c/T})$. (c)-(d) Plot of $\sigma_2/\sigma_2(5K)$ versus T_c/T for the Ca-YBCO ring resonator with (c) $p=0.218$ and (d) $p=0.121$, respectively. The solid line is the fitting result with the formula, $\sigma_2/\sigma_2(5K) = (1 - Be^{-c_2 \cdot T_c/T})$.
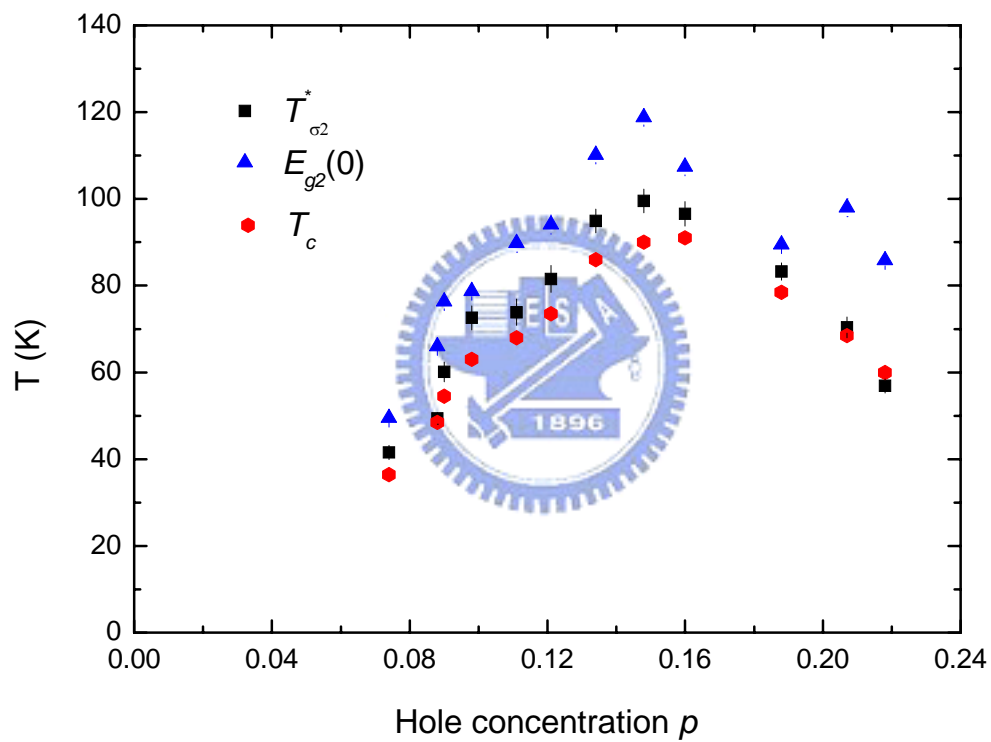
Fig. 4.50. The doping dependence of the characteristic energy scale, $T_{\sigma2}^{*}$, $E_{g2}(0)$ and T_c of the YBCO and Ca-YBCO thin films was obtained from the fitting of $\sigma_2/\sigma_2(5K)$.

Fig. 4.51. The temperature dependence of the imaginary part of the microwave conductivity, σ_2, for (a) the YBCO and (b) the Ca-YBCO microstrip line resonators with various hole concentrations. The values of σ_2 increases as decreasing T at $T < T_c$ for all doping levels.

176

Fig. 4.52. Plot of σ_2 / σ_2(5K) versus T_c/T for the YBCO and Ca-YBCO microstrip line resonators with various hole concentrations.

Fig. 4.53. (a)-(b) Plot of $\sigma_2/\sigma_2(5K)$ versus T_c/T for the YBCO microstrip line resonator with (a) p=0.148 and (b) p=0.09, respectively. The solid line is the fitting result with the for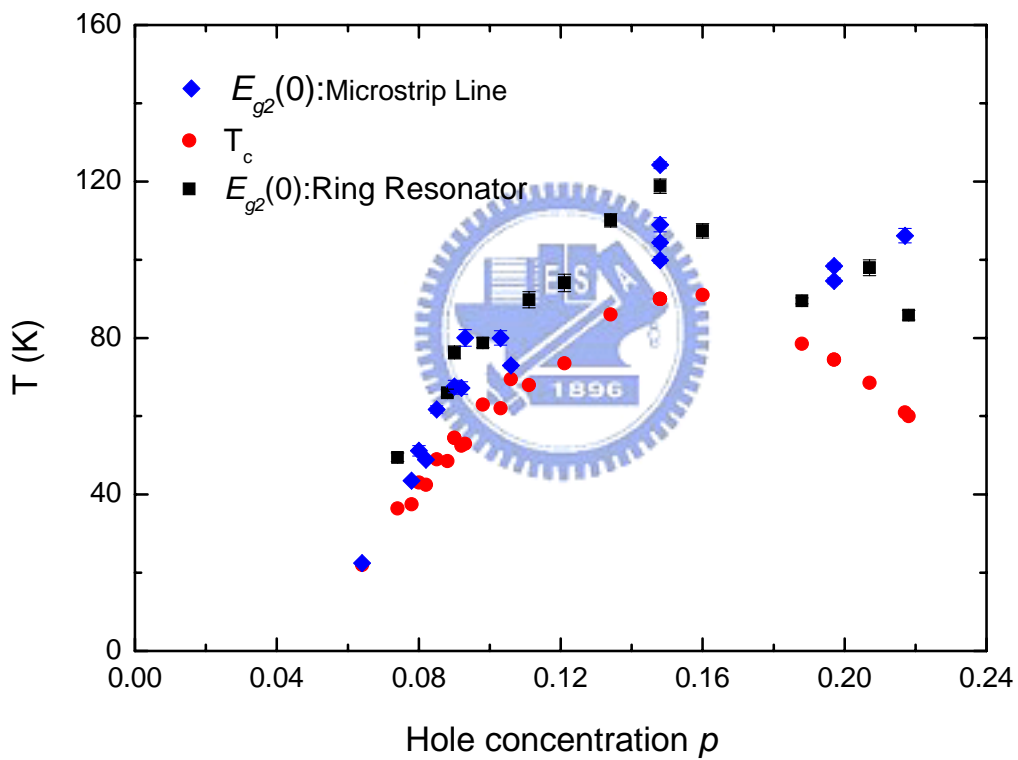mula, $\sigma_2/\sigma_2(5K) = (1 - Be^{-c_2 \cdot T_c/T})$. (c)-(d) Plot of $\sigma_2/\sigma_2(5K)$ versus T_c/T for the Ca-YBCO microstrip line resonator with (c) p=0.217 and (d) p=0.078, respectively. The solid line is the fitting result with the formula, $\sigma_2/\sigma_2(5K) = (1 - Be^{-c_2 \cdot T_c/T})$.

Fig. 4.54. The doping dependence of the characteristic energy scale $E_{g2}(0)$ and T_c of the YBCO and Ca-YBCO thin films was obtained from the fitting of σ_2.
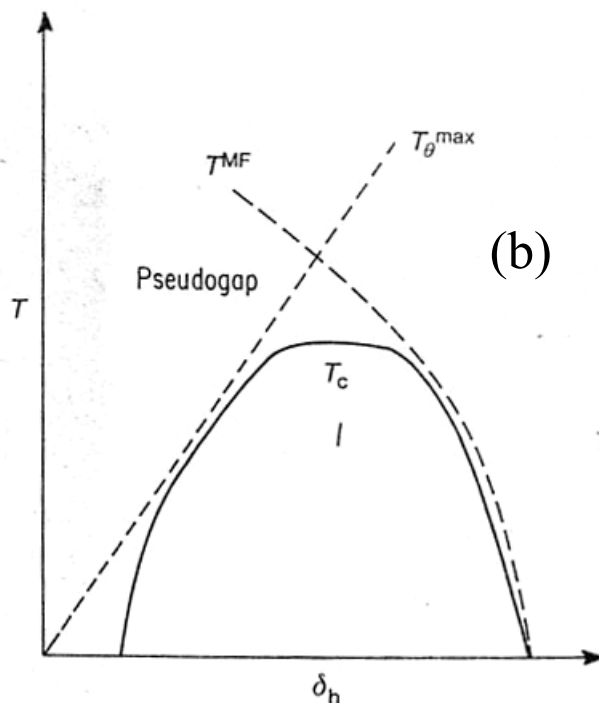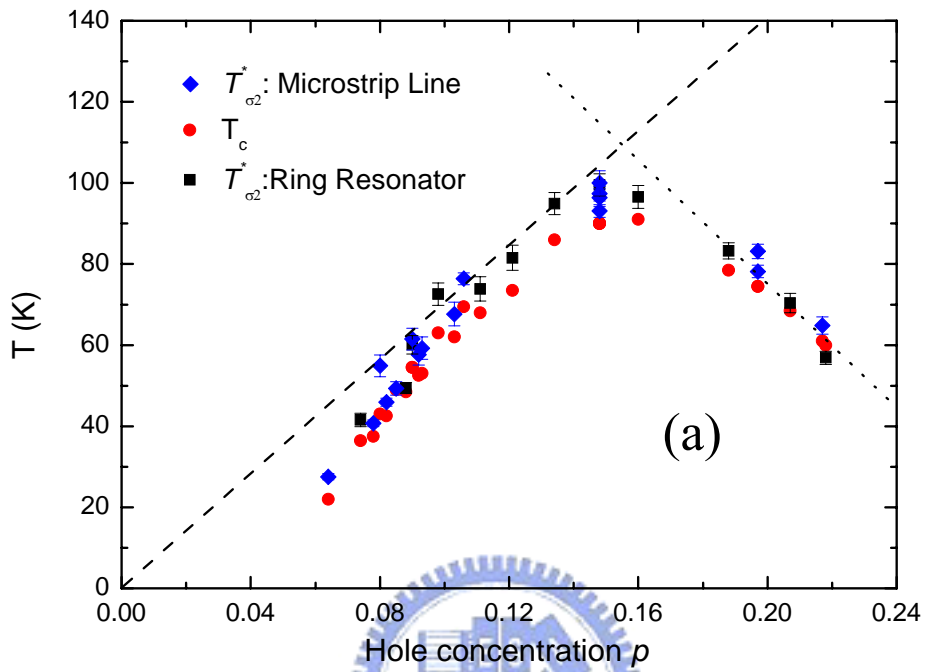
Fig. 4.55. (a)The doping dependence of the characteristic energy scale $T^*_{\sigma 2}$ and T_c of the YBCO and Ca-YBCO thin films extracted from the microwave conductivity, $\sigma_2(T)$, measurements. (b) The doping dependence of the characteristic energy scale T^{max}_θ, T_c, and T^{MF} sketched by Emery and Kivelson [88]. From (a) and (b), the same systematically tendency for $T^*_{\sigma 2}$ and T^{max}_θ in the underdoped regime was shown. However, in the overdoped regime, $T^*_{\sigma 2}$ corresponds to the T^{MF}.
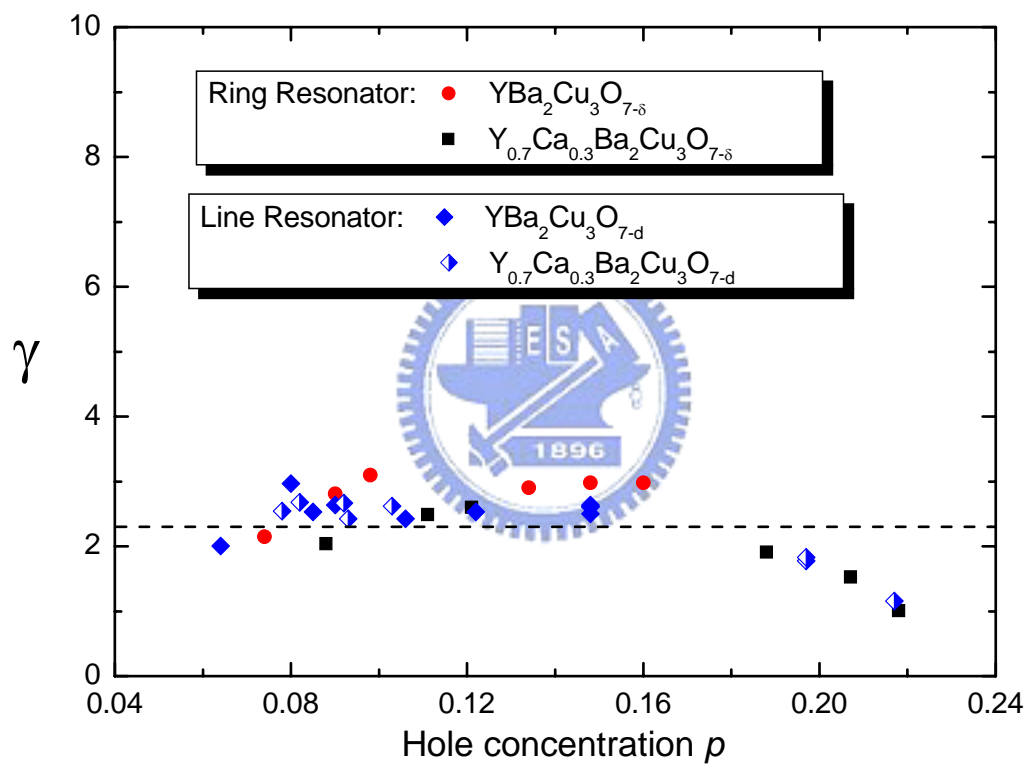
Fig. 4.56. The doping dependence of the factor, γ, extracted from the imaginary part conductivity, $\sigma_2(T)$, measurements for the YBCO and Ca-YBCO thin films.